Development of Segmented Ionization Chamber Technologies for High-Precision Low-Rate Experiments

by

Andrew Redey

B.A.Sc., Simon Fraser University, 2021

Thesis Submitted in Partial Fulfillment of the
Requirements for the Degree of
Master of Applied Science

in the
School of Engineering Science
Faculty of Applied Sciences

© Andrew Redey 2023

SIMON FRASER UNIVERSITY

Fall 2023

Declaration of Committee

Name: **Andrew Redey**

Degree: **Master of Applied Science**

Title: **Development of Segmented Ionization Chamber Technologies for High-Precision Low-Rate Experiments**

Committee: **Chair: Shawn Sederberg**
Assistant Professor, Engineering Science

Andrew Rawicz
Co-Supervisor
Professor, Engineering Science

Krzysztof Starosta
Co-Supervisor
Professor, Chemistry

Ash Parameswaran
Committee Member
Professor, Engineering Science

Greg Hackman
Examiner
Adjunct Faculty, Chemistry

Abstract

The construction of a Frisch grid ionization chamber with positional sensitivity to ionizing particles is presented in this work. The SCI-CASTER project in the Simon Fraser University Nuclear Science Laboratory aims to achieve both high energy resolution and the ability to perform full 3D reconstruction of ionizing particle tracks. SCI-CASTER prototype 1.9 is discussed in this work as the first prototype detector in the SCI-CASTER project that has demonstrated sensitivity to the spherical azimuthal angle of emission of alpha particles emitted from an electroplated triple-alpha source. A dedicated test setup for conducting experiments with ionization chamber detectors has also been established, complete with anti-vibration mounting to limit mechanical vibration, computer controlled gas and high voltage systems, and a waveform digitizing data acquisition system with support for up to 120 signal inputs.

Keywords: Ionization chamber; tracking of ionizing particles; Frisch grid

Dedication

To my grandparents.

Acknowledgements

Table of Contents

List of Tables

List of Figures

x

Chapter 1.   Introduction

A gas ionization chamber is a type of radiation detector that operates based on incident radiation ionizing a gaseous medium. These detectors are a popular choice for radiation dose measurements in industry and medicine when operated in a direct current (DC) mode. In the field of nuclear research however, these same detectors with minor geometry adjustments and alternating current (AC) operation, can prove to be one of the best tools for performing alpha particle spectroscopy [1], [2], [3] and fission fragment analysis [4], [5], [6], [7]. This work will outline the process of building and evaluating the second design in a series of prototype detectors aimed at performing high energy and spatial resolution alpha spectroscopy with low-activity sources. This series of prototypes is known as the Segmented Conductor Ionization Chamber for Advanced Spectroscopy Targeting Emitters of alpha Radiation, or the SCI-CASTER project.

1.1.   Alpha Decay and Ionization Processes

Alpha particles are a type of ionizing radiation, where other common types include beta particles and gamma rays. These can be produced in a variety of ways, however, the detector discussed in this work is being built to detect alpha particles that result from alpha decay.

Alpha decay arises from heavy nuclei (the initial nuclear species X with atomic mass A and atomic number Z) that are energetically unstable and decay to the final nuclear species Y by releasing a ^{4}He nucleus, otherwise known as an alpha particle [4, p. 6]:

$$^A_Z X \rightarrow {}^{A-4}_{Z-2} Y + {}^4_2 \text{He}. \tag{1.1.1}$$

As seen in Eq. 1.1.1, an alpha particle has a charge of $+2e$, where e is the elementary charge. Once emitted, an alpha particle ionizes surrounding atoms by attracting their electrons through the Coulomb force, where this can have one of two effects:

1. *Excitation:* Electrons in the affected atom are pulled to a higher energetic state.

2. *Ionization:* Electrons in the affected atom are ejected, thus producing a free electron and a positive ion (referred to as a charge pair).

With each interaction listed above an alpha particle will lose some energy[1]. As the particle travels through a medium and undergoes multiple interactions, it will eventually lose all its energy and stop. For a medium with a low first ionization potential, that is, with a small energy required to remove a single electron from an atom, the ionization process is of particular interest. Under these conditions, the location and quantity of the generated charge pairs is reflective of the incident alpha particle's energy and path and therefore provides an indirect means of characterizing alpha radiation.

1.2. Applications of Alpha Spectroscopy

While there are practical applications for alpha spectroscopy, the field is also of great interest in fundamental nuclear research. Brief descriptions of some of the use cases are given here, with emphasis on the benefits of ionization chamber technology where applicable.

1.2.1. Alpha-Gamma Angular Correlation and Perturbation Studies

Alpha-gamma angular correlation experiments are used to characterize external factors that perturb the angle of emission between an alpha particle and a gamma ray. In isolation, this angle can be determined based on analysis of alpha-gamma decay properties. In reality however, there is the potential for hyperfine interactions, for example with the surrounding environment, that are not necessarily known and that will change the angles of emission between the alpha particle and the gamma ray.

A typical experimental setup for perturbation studies consists of an array of gamma ray detectors positioned around the source alongside one or multiple silicon surface barrier (SB) alpha particle detectors [8], [9], [10]. The angles between the detectors are either held

---

[1] There is an upper limit to the energy lost per collision, this is discussed in Appendix A

at a known constant for the duration of the experiment, or the alpha detectors are moved relative to the gamma ray detectors to cover multiple angles.

The inherent downside of using discrete SB detectors is that the efficiency, that is, the fraction of total alpha emissions that are detectable, is strictly limited by the angle of acceptance of each SB detector. By contrast, a position-sensitive ionization chamber can in principle detect all alphas emitted from the face of the source, and therefore greatly increase sensitivity and/or reduce experiment runtime.

1.2.2. Uranium Series Disequilibrium Studies

One of the practical applications of alpha spectroscopy is the dating of mineral samples in geological studies using uranium series disequilibrium measurements. This method of dating allows for the time of formation to be determined by calculating the intensity ratios of various isotopes along the uranium decay chain [11], [12]. While not requiring multiple angles to be observed as done in perturbation studies, the efficiency of an ionization chamber is still far superior to an SB detector. This should prove to be a significant upgrade to the process, provided that the necessary energy resolution can be achieved (this topic is discussed further in Section 1.3).

1.2.3. Isotope Lifetime Measurements

While ionization chamber detectors are capable of measuring the lifetimes of alpha emitters in general, they are particularly applicable to measurements of low-activity isotopes. This is because alpha particles are easily stopped in the solid source material from which they originate, and therefore the thickness of the prepared source must be kept to a minimum to avoid energy smearing of the detected particles and outright losses in the material. For an isotope with a long half-life, this means that a thin source material with a large surface area is required to achieve an acceptable activity rate, and therefore a detector system with a large angle of acceptance is required. It is clear then, that an ionization chamber scaled up to contain the source material is an ideal detector for this application [1], [3], [13].

1.2.4. Neutron Induced Reaction Studies

Neutron induced reactions involve a thin target material being bombarded by neutrons, where these neutrons may be a random flux or a beam directed at the target. Particularly due to the recent developments in fusion technology, measuring reaction cross sections of various materials when interacting with 14.2 MeV neutrons[2] has become of interest [14]. In the case of using a random neutron flux, a detector that does not degrade with exposure to radiation is ideal, and this role is easily filled by an ionization chamber in which the gas medium is flowed and constantly replaced as the experiment runs. In the experiment detailed in [14], where a pencil beam was used to reduce background interactions, an ionization chamber would increase the efficiency of the experiment and therefore increase sensitivity and allow for a reduced runtime.

1.3. Consideration in Alpha Detector Design

As seen in Section 1.2, there exist multiple technologies for detecting alpha particles, where each will have its own distinct advantages and drawbacks. A brief overview of different detector classes and designs is presented here.

1.3.1. Gaseous Detectors

Gaseous detectors operate on the principle of alpha particles ionizing a known gaseous medium, and subsequently measure the drift of charges as they traverse an electric field supplied by electrodes in the detector volume. These detectors are usually manufactured using copper plates or printed circuit boards (PCBs) alongside wire wound frames, thus making the physical construction of a gaseous detector more affordable and simple when compared to other detector technologies. Furthermore, since the signals read out from these detectors are reliant on the induced charge from the movement of charge pairs, it is possible to build tracking chambers by utilizing multiple electrodes. Two relevant examples of gaseous detectors are ionization chambers and wire chambers.

---

[2] Deuterium-Tritium (D+T) fusion produces 14.2 MeV neutrons.

A typical ionization chamber measures the drift of charges between two detector regions divided by a wire grid known as a Frisch grid, where the charges at the end of their drift are collected by the positively charges anode electrode. The anode and cathode take the form of two large conductive surfaces, thus giving the chamber an appearance of the simple parallel plate capacitor with large plate spacing. By comparison, a wire chamber uses either a single or multiple wires to collect the charges, thus giving inherent positional sensitivity to multi-wire designs utilizing multiple readout channels. This style of detector is commonplace in high-energy physics [15], [16].

Energy resolution in gaseous detectors is typically between 40 keV and 200 keV [4], [3], [17], with a lower limit imposed by a value known as the Fano factor (this is discussed further in Section 3.2.2).

1.3.2. Semiconductor Detectors

Semiconductor detectors, while generally being more expensive and complex than gaseous detectors, offer superior energy resolution typically around 20 keV. One of the most common choices for semiconductor detectors used for alpha spectroscopy is the SB detector, as seen in Section 1.2. These discrete detectors [18], while convenient, offer no positional sensitivity (outside of the known physical location of the detector) and are limited to a small window of acceptance, which in turn limits the efficiency of the detector. Using multiple SB detectors in an array is an option, however, full coverage of the alpha source would be a costly and complex process. As an alternative, silicon strip or pixel detectors are used to achieve a much higher detector density by segmenting the silicon-based electrodes [4, p. 493], greatly mitigating the issue of positional sensitivity. Again, this comes with a large cost and complexity associated with the readout and amplification of many individual silicon detectors.

1.3.3. Scintillation Detectors

Scintillation detectors operate by using a light-sensitive component such as a photomultiplier tube (PMT) or PIN diode coupled to a scintillating material. A scintillator emits light in a given wavelength range when struck by ionizing radiation, thus creating an

5

optical signal proportional to the energy of the interacting particle. While PMTs are costly, PIN diodes or other types of photodiodes are relatively inexpensive, and therefore creating entire detector arrays to achieve positional resolution and angular coverage is feasible. This has been done using Thallium-doped Cesium Iodide scintillation detectors [19], and has been used in in-beam experiments multiple times.

The major caveat with these detector systems is that each scintillator and its light sensor must be optically isolated from all others, or light will escape resulting in signal loss and crosstalk on other detectors. To alleviate this, each detector is wrapped in a light-tight foil, however, this results in some energy loss as alpha particles enter the scintillator face, and for this reason there is an inherent degradation to energy resolution. Because of this, the energy resolution of such a system is typically between 280 keV and 550 keV for alpha particles [20], [21].

1.4. Ionization Chamber Applications at the SFU Nuclear Science Laboratory

The SCI-CASTER project was started due to the advancements in spectroscopic capabilities it could provide in the Simon Fraser University Nuclear Science Lab (SFU NSL). In particular, the design's potential to track alpha particles while being highly adaptable to geometric constraints and able to survive in neutron radiation fields puts it in a unique position to fulfill multiple roles in the lab.

1.4.1. Operation with the 8Pi Gamma Ray Spectrometer

The SFU NSL houses a full 4π coverage gamma ray spectrometer called the 8Pi [22], which uses two layers of gamma ray detectors for simultaneous high-efficiency and high-resolution gamma ray measurements. The spectrometer is presently being refurbished to operate with modernized electronic hardware and computer systems, where it was previously in service at the TRIUMF ISAC-1 facility and Chalk River Laboratories before this. When complete, usage of the 8Pi alongside a miniaturized SCI-CASTER detector will allow for alpha-gamma correlation studies as detailed in Section 1.2.1. Further, a twin-sided chamber can be used to perform fission fragment analysis on a radioactive source or

on samples activated in a neutron field. Construction of this detector will be challenging due to the physical constraints of the 8Pi core (Figure 1.4.1), particularly with regard of to the proximity of amplifier circuits to the detector and holding gas pressure in a complex containment vessel.
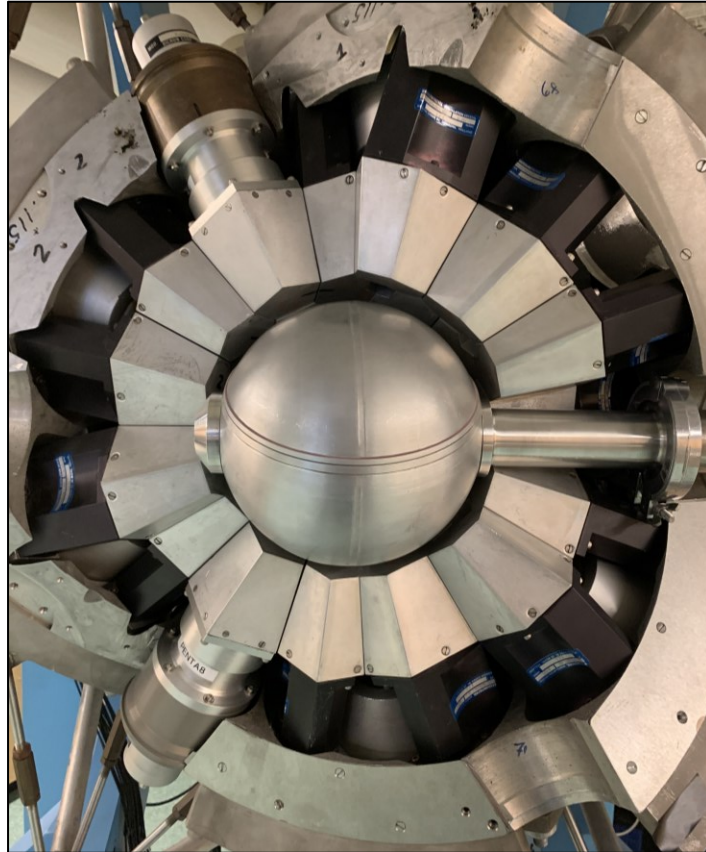
Figure 1.4.1: One half of the 8Pi spectrometer core with vacuum chamber installed. The vacuum chamber is 8" in diameter and is flanked by an inner layer of Bismuth Germanium Oxide (BGO) gamma ray detectors.

1.4.2. Neutron Induced Reactions in the Neutron Generator Facility

The basement of the SFU NSL is known as the neutron generator facility (NGF). The facility houses a Thermo-Fisher P385 neutron generator in a concrete vault [23], [24], which can be used for the irradiation of either target materials for in-vault experiments, or irradiation of samples that can be transported to other detection systems (the 8Pi for example). This facility, when coupled with appropriate neutron shielding and targets of interest, can be used in conjunction with a future SCI-CASTER detector to perform neutron

induced reactions, much like the setup described in [14]. Should any experiments require that the full detector be exposed to the neutron field, ionization chambers have the advantage that unlike semiconductors, their gaseous medium can be flowed continuously to replace any gas damaged by radiation. Reactions are also not limited to alpha particles, as both protons and fission fragments can be studied with minor detector modifications.

1.4.3. The Long-Lived Emitters of Alpha Particles Program

The Long-Lived Emitters of Alpha Particles Program (LLEAP Program) is aimed at the measurement of alpha emitters with long half-lives as discussed in Section 1.2.3. An oversized ionization chamber is intended to be built within the current test vessel and be used specifically for the measurement and verification of such isotope lifetimes. The tracking capabilities of SCI-CASTER detectors will allow for the rejection of events that come from outside of the detector, and its size will enable a high efficiency such that measurement times are feasible. Work in this area has already been explored in references [1], [3], [13], where it has been demonstrated that ionization chambers are ideal detectors for these types of experiments.

Chapter 2. Conventional Ionization Chamber Theory of Operation

Before discussing the practical implementation of an ionization chamber, it is first important to characterize the detector's behavior from the ground-up under ideal circumstances. We begin with the ionization of the detector gas environment, followed by the addition of detector electrodes and their respective electric fields. Finally, a discussion on induced charge and the expected signal outputs is presented.

2.1. Ionization of a Gas

To begin, consider an alpha particle point source immersed in a known gas at a known pressure. The specific energy of the alpha particles emitted from the source is unimportant for now, however for reference, energies between 4 MeV and 6 MeV are common. As alluded to in Chapter 1, alpha particles can be easily stopped in a few centimeters by a gas alone, and their range in most solids is sub-0.1 mm. Therefore, alpha sources need to be a thin layer of material with no protective casing. This is because the alphas would not only be stopped by a casing, but experience energy losses by interacting with the source material from which they originate. This is of particular concern when measuring the energy resolution of a detector, since the source material itself can cause a low-energy smear that overshadows the detector response. For this reason, alpha particle spectroscopy sources are typically electroplated on a metallic surface with a sub-micron thickness, and even so come with a quoted full width at half max (FWHM) denoting the best observable resolution possible. An illustration of how source material thickness can affect the energy of an alpha particle is shown in Figure 2.1.1:

(a) 0.1 μm samarium thickness. *(b) 1.0 μm samarium thickness.* *(c) 5.0 μm samarium thickness.*
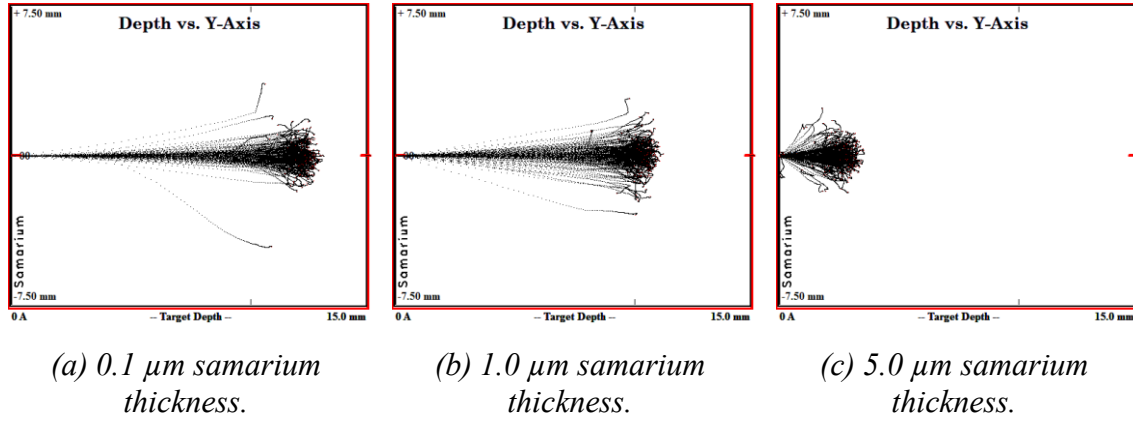
Figure 2.1.1: Ziegler TRIM [25] simulations of ^{147}Sm alpha particles traversing varying thicknesses of source material and exiting into argon gas. Particles are emitted left-to-right at the same energy of 2248 keV, the reduction in path length comes from energy being absorbed by the source material itself.

Once an alpha particle has escaped from the source material, it will repeatedly interact with the gas atmosphere, losing energy with each interaction and ionizing the gas thus producing positively charged ions and free electrons. The path of charges left behind by the alpha is known as a *charge track*. The average energy per ionization is given by a measure known as the W-value which is discussed briefly in Section 3.2.1. This means that once the alpha particle has given up all energy to ionizing the gas, the number of charges now drifting freely in the gas is proportional to the energy of the alpha particle. If a method of determining the total charge in the gas is then implemented, an indirect measurement of the energy of the alpha particle can be performed. Further, if the location of the charges can be determined, the trajectory of the alpha particle can be characterized.

It is the measurement of these charges that is the basis of ionization chamber operation, which will now be expanded upon by considering a common ionization chamber geometry.

2.2. Detection of Ionizing Particles Using an Ionization Chamber

For this section, a design known as the Gridded Ionization Chamber will be considered (Figure 2.2.1). This design is distinct in that it utilizes a parallel wire grid known as a Frisch grid, named after its inventor Otto Frisch. These detectors are also known as

Frisch Grid Ionization Chambers (FGICs), are a very common if not the most common design in existence, and are the basis of the SCI-CASTER project. Notice that the FGIC is divided into two regions by the Frisch grid. These regions are known as the ionization region (where the gas atmosphere is ionized by alpha particles) and the collection region (where the generated charges are collected).
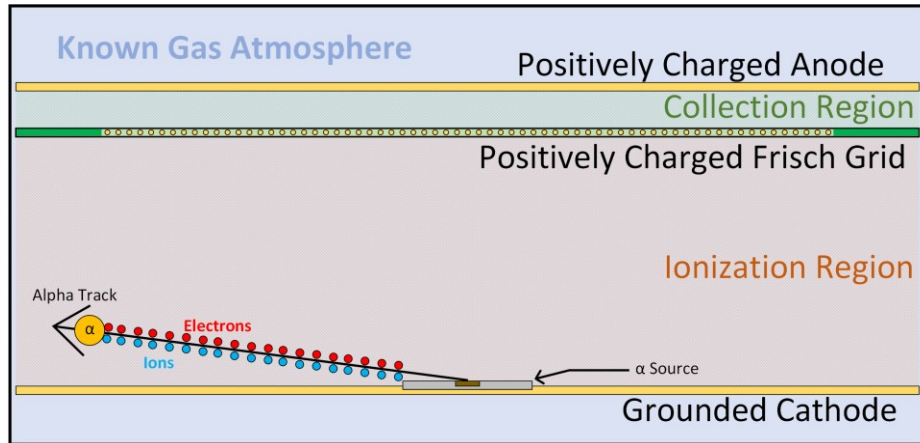
Figure 2.2.1: Basic structure of an FGIC.

In order to determine the total charge produced by the alpha particle ionizing a gas, a static electric field is applied to the detector shown in Figure 2.2.1. Under the influence of this electric field, the free charges will drift through the detector volume until impacting the detector electrodes. A common misconception is that it is solely the *collection* of these charges that result in a charge deposit on the electrodes. In actuality this is not the case, and it is in fact the *drift* of charges through the electric field supplied by the electrodes that results in opposite induced charge buildup, eventually followed by charge collection. This effect is explained by the Shockley-Ramo theorem [26].

2.3. The Shockley-Ramo Theorem

The Shockley-Ramo theorem states that the movement of charges under the influence of an electric field supplied by an arbitrary conductor will induce opposing charges in that same conductor. This means that as the charge pairs drift through the detector shown in Figure 2.2.1, a charge buildup is observed on the electrodes from the

instant the charges start to move, and long before they come into contact with the electrodes.

The full derivation of the theorem can be completed using References [26] and [27], and is given in Appendix B. The results of the derivation are the time-dependent induced charge $Q(t)$ and current $i(t)$ on an arbitrary electrode by a particle point charge:

$$Q(t) = -q\varphi_{2R}(\vec{s}(t)), \tag{2.3.1}$$

$$i(t) = q\vec{E}_{2R}(\vec{s}(t)) \cdot \vec{v}(t), \tag{2.3.2}$$

where q is the particle's charge, $\vec{s}$ is the position of the point charge, $\vec{v}$ is the velocity of the point charge, and φ_{2R} and $\vec{E}_{2R}$ are the Ramo weighting potential and Ramo weighting field, respectively. Of important note here (and shown in Appendix B) is that the Ramo weighting potential is equivalent to the electrostatic potential divided by the units of Volts, and that the Ramo weighting field is equivalent to the electric field divided by the units of Volts.

Equations 2.3.1 and 2.3.2 are general statements which may be applied to any geometry. For the simplest case, which applies to a parallel plate detector design of sufficient radius and voltage such that electric field fringing effects are negligible, the Ramo weighting field for the detector anode becomes $-1/D$, where D is the distance between the parallel plates (Figure 2.3.1).
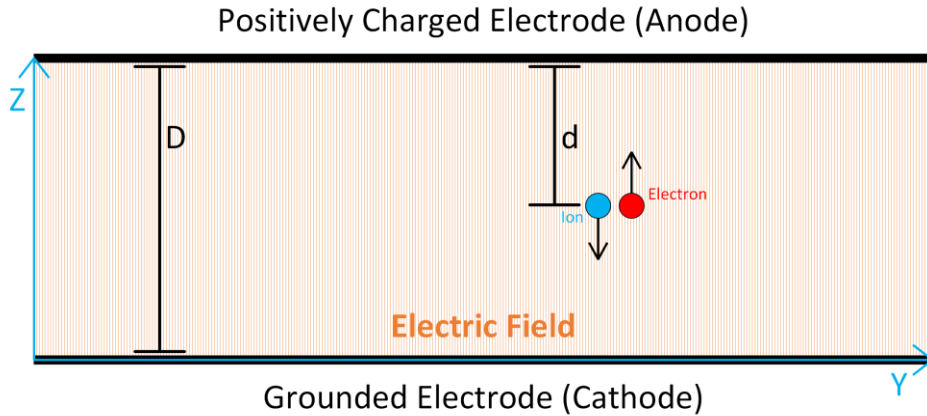
Figure 2.3.1: Parallel plate ionization chamber geometry.

Knowing that the line integral of the electric field is equal to the electrostatic potential,

$$\varphi_{2R}(\vec{s}(t)) = -\int_C \vec{E}_{2R}(\vec{s}(t)) \cdot d\vec{s}(t). \tag{2.3.3}$$

The weighting field of $-1/D$ assumes that the electric field is uniform and perpendicular to the plate planes. Further, it is assumed that the drift of charges in the detector is also perpendicular to the plate planes. Under these assumptions,

$$\vec{E}_{2R}(\vec{s}(t)) = E_{2R}\hat{e}_z, \tag{2.3.4}$$

$$\vec{s}(t) = s(t)\hat{e}_z, \tag{2.3.5}$$

and therefore:

$$
\begin{aligned}
\varphi_{2R}(\vec{s}(t)) &= -\int_C E_{2R}\hat{e}_z \cdot ds(t)\hat{e}_z \\
&= -\int_C E_{2R}\,ds(t) \\
&= -\int_C -\frac{1}{D}\,ds(t) \\
&= \frac{1}{D}\int_C ds(t) \\
&= \frac{s(t)}{D}.
\end{aligned}
\tag{2.3.6}
$$

Under the assumption that the velocity of the charged particle is constant,

$$s(t) = vt, \tag{2.3.7}$$

$$vt \leq d,$$

we may simply state

$$Q(t) = -\frac{qvt}{D}. \tag{2.3.8}$$

13

2.4. Induced Signals in an FGIC

An intuitive understanding of the signals expected from an FGIC can be attained by considering the FGIC structure shown in Figure 2.2.1 alongside Equation 2.3.8. The purpose of the Frisch grid is to decouple the electric fields in the two regions of the detector while simultaneously allowing charges to drift through it and reach the anode. While in practice there are several caveats and phenomena that arise from the design of the grid, it is for now assumed that the Frisch grid perfectly decouples the detector fields and is completely transparent to charge drift. Further, it is also assumed that the drift of ions is ~1000x slower than the drift of electrons through the detector (This assumption is explored further in Section 2.5). This means that for a single charge track, the effects of ion drift can be safely ignored when plotting the induced signal from electron drift.

Under these assumptions, consider two time intervals for charge drift resulting from a single alpha particle track:

Time Interval 1: Electrons are drifting through the ionization region towards the Frisch grid, ions are drifting towards the cathode.

Time Interval 2: Electrons are drifting through the collection region away from the Frisch grid, ions are still drifting towards the cathode.

The addition of a charge track to the FGIC geometry with the mean of the charge distribution along the track denoted by $\bar{x}$ is shown in Figure 2.4.1.
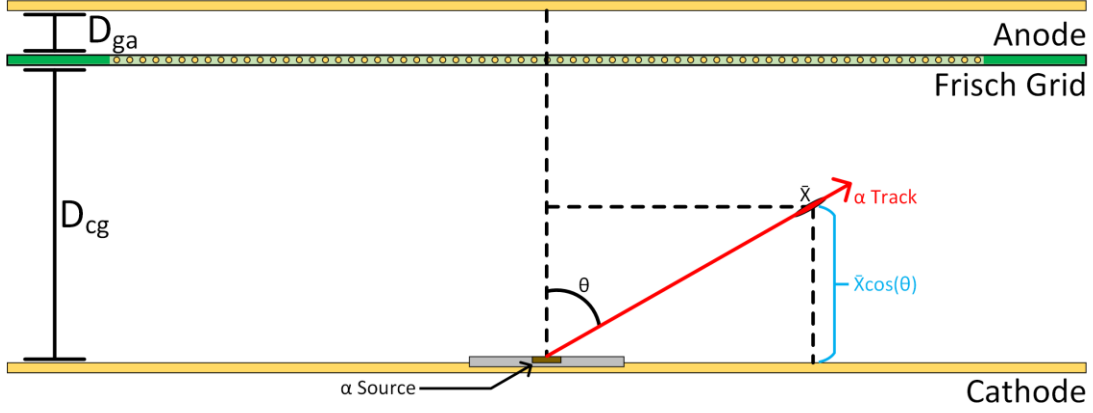
Figure 2.4.1: A single alpha particle track and its mean charge distribution.

For the purposes of this work, the anode and Frisch grid induced charges are of interest and can be found by substituting parameters from Figure 2.4.1 into Equation 2.3.8 to yield the time-dependent induced charge for each time interval. Note that the induced charge due to ion drift is consistent across both time intervals, and it is therefore given only once under time interval 1.

Time Interval 1:

$$Q_{grid,ion}(t) = -\frac{Ne}{D_{cg}}(v_{ion}t), \tag{2.4.1}$$

$$v_{ion}t \leq \bar{x}cos(\theta),$$

$$Q_{grid,electron}(t) = \frac{Ne}{D_{cg}}(v_{electron}t), \tag{2.4.2}$$

$$v_{electron}t \leq D_{cg} - \bar{x}cos(\theta),$$

$$Q_{anode,ion}(t) = Q_{anode,electron}(t) = 0. \tag{2.4.3}$$

Time Interval 2:

$$Q_{grid,electron}(t) = -\frac{Ne}{D_{ga}}(v_{electron}t), \tag{2.4.4}$$

15

$$Q_{anode,electron}(t) = \frac{Ne}{D_{ga}}(v_{electron}t), \qquad (2.4.5)$$

$$v_{electron}t \leq D_{ga},$$

where N is the number of charge pairs, e is the elementary charge, v_y is the drift velocity of the particle y, and t is the drift time.

The above equations result in piecewise waveforms for the grid and anode electrodes. Under the assumption that the induced charge due to ion drift is negligible on the time scale of electron drift, the induced charge waveforms expected in an FGIC can easily be plotted and are shown in Figure 2.4.2. These waveforms will have a positive polarity as derived above, since the induced charge on the electrodes opposes the polarity of the drifting charge. Note that due to charge being distributed along the length of the alpha track, the sharp boundaries between regions are in practice expected to have smoothed transitions.
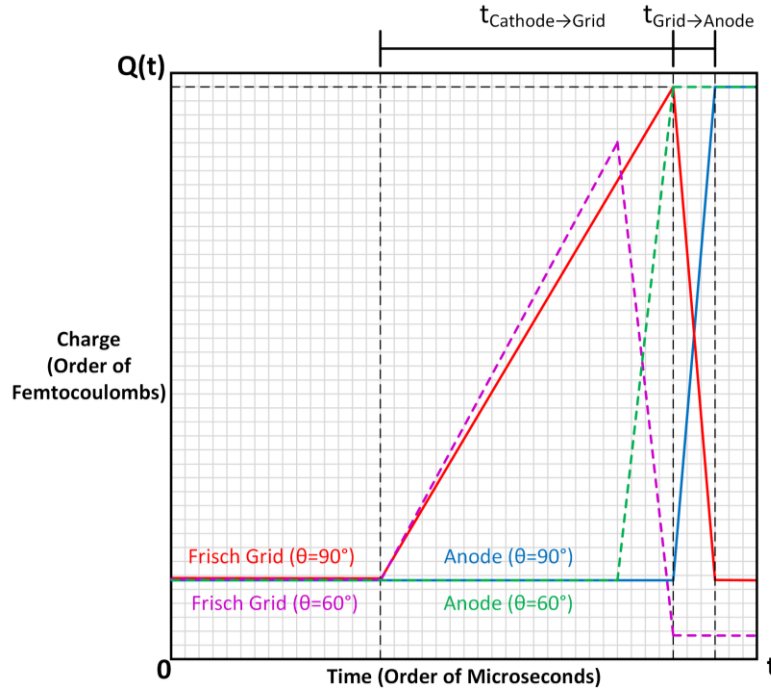
Figure 2.4.2: Ideal, expected signals from an FGIC. Note the difference in signal behavior based on the angle of emission, where the blue and red lines indicate a grazing polar angle, and the dashed green and yellow lines indicate a polar angle of appproximately 60°.

16

The Frisch grid waveform shown in Figure 2.4.2 has a maximum amplitude governed by Equation 2.4.2 and its upper limit imposed on $v_{electron}t$ which yields

$$Q_{grid,maximum} = Ne\left(1 - \frac{\bar{x}cos(\theta)}{D_{cg}}\right). \qquad (2.4.6)$$

Similarly, the anode waveform has a maximum amplitude governed by Equation 2.4.5 and its upper limit, yielding

$$Q_{anode,maximum} = Ne. \qquad (2.4.7)$$

From Equation 2.4.6, it is evident that the pulse amplitude of the Frisch grid signal not only has a dependence on the number of charge pairs produced, but additionally the polar angle of emission of the alpha particle. By comparison, the maximum amplitude of the anode signal is purely dependent on the number of charge pairs and is therefore reflective of the energy of the alpha particle. Herein lies the purpose of the Frisch grid, as without it the anode would take on the polar angle dependence of the Frisch grid and the ability to recover the alpha particle energy would be lost.

2.5. Drift of Charged Particles in a Gas

The assumption presented in Section 2.4 regarding the drift velocity of ions vs. that of electrons is generally valid for charge drift through a gas in the presence of an electric field. The drift velocities of the charges can be approximated by

$$v_{ion} \approx \frac{\mu E}{p}, \qquad (2.5.1)$$

$$v_{electron} \approx 1000v_{ion}, \qquad (2.5.2)$$

where μ is the ion mobility of the gas, E is the electric field in the region of drift in V/m, and p is the gas pressure in atmospheres (atm). The range of ion mobilities for a gas is typically between 1 and 2×10^{-4} m^2·atm/V·s [4, p. 133].

Given the resulting drift velocities of the charged particles and the typical size of an ionization chamber (on the order of centimeters to 10's of centimeters), drift times on the order of microseconds for electrons and milliseconds for ions are expected. For this reason, the impact of ion drift on the induced signal for a single charge track is negligible and can be safely ignored when considering the waveforms that will be observed by an ionization chamber detector.

2.6. Expected Magnitude of the Induced Charge

To give a sense of the magnitude of the signals generated by an ionization chamber, the average energy per ionization (the W-value) can be used alongside the energy of the alpha particle to compute the total charge of the electrons in the track. Supposing a W-value of 26.3 eV per charge pair (the W-value for argon gas) [4, p. 130], and an alpha particle energy of 5.8 MeV, the total charge in femtocoulombs is

$$Q_{electron,total} = (1.6 \times 10^{-19}\text{C}) \frac{5.8 \times 10^6 \text{eV}}{26.3 \text{eV/pair}} \qquad (2.6.1)$$
$$= 35.3\text{fC/track.}$$

Knowing this, it is apparent that a low-noise, high-gain amplifier that is capable of converting the induced charge into a voltage signal will be required to read out the induced charges in the detector. This type of amplifier is commonly known as a charge-to-voltage converter, or equivalently, as a high-gain transimpedance amplifier with a decay time on the order of 100's of microseconds. The design and operation of the amplification circuitry used in the SCI-CASTER project is further detailed in Chapter 5.

Chapter 3.   SCI-CASTER Prototype 1.9 Geometry and Operating Conditions

The second prototype detector in the SCI-CASTER project, prototype 1.9, has been built to test fundamental detector and circuitry design while simultaneously verifying expected tracking capabilities. An explanation of the detector geometry, how this geometry relates to ionizing particle tracking, and considerations in selecting the detector operating conditions are discussed below.

3.1.   Segmented Detector Design

The long-term goal of the SCI-CASTER project is to develop detectors capable of tracking ionizing particles in 3D space. In the short-term, the focus lies specifically on fully characterizing low-activity alpha particle sources. As seen in Chapter 2, particles originating from a thin alpha source (Figure 3.1.1) held in a conventional FGIC detector produce induced charge waveforms that contain both energy information in the form of signal amplitude and polar angle information derivable either from drift times or the shift in the Frisch grid baseline pre- and post-event.
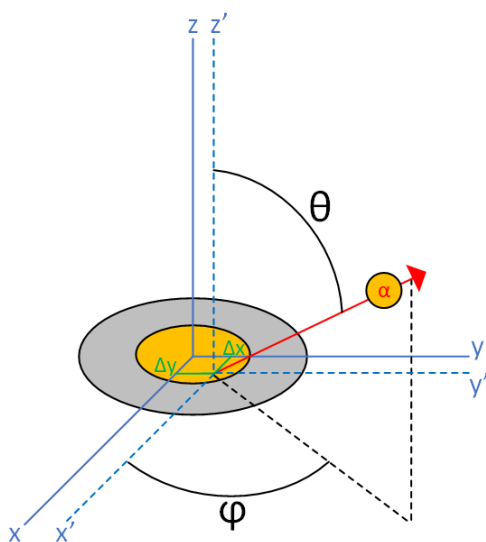
Figure 3.1.1: Alpha particles from a distributed source have an energy, two spherical angles of emission, and a positional offset relative to the chamber origin.

Figure 3.1.1 shows that information about the origin of the alpha particle track relative to the chamber origin as well as the azimuthal angle φ are missing from the waveforms produced by the typical FGIC design shown in Figure 2.4.2, which only contains information on the particle energy and polar angle. For the purposes of this work, the alpha particle source is assumed to be a point source, and under this assumption, what remains to be determined is only the azimuthal angle.

A conventional FGIC detector is completely insensitive to charge track rotations as the sensitive electrodes are all symmetric about the vertical axis of the chamber. Therefore, to gain azimuthal angle sensitivity, it is necessary to either add electrodes to the detector, or more simply, to segment one or multiple of the existing detector electrodes into multiple sensitive elements. In doing this, each segment of the electrode will have its own Ramo weighting field, and therefore effectively experience an induced charge dependent on the proximity of moving charges to the individual segment.

The goal of SCI-CASTER prototype 1.9 is to test the theory and simulation results behind the segmented design by splitting the detector anode into two conductive semicircles, thereby creating the simplest detector possible that has azimuthal angle sensitivity. Furthermore, the prototype serves as a test to evaluate the mechanical and electrical complexity of building such a detector before significant investments are made into a fully-featured model.

3.1.1. SCI-CASTER Prototype 1.9 Physical Construction

The SCI-CASTER prototype 1.9 geometry is built upon that of SCI-CASTER prototype 1.0 [28], which itself was reused from the prior TIFFIN project [29]. The primary reason for reuse of the detector geometry is the cost and complexity associated with making a new Frisch grid. This was unjustifiable given that the existing detector, with modifications to the anode, would serve as an acceptable test apparatus for both confirmation of the theory of operation as well as the electronic design and anode production methodology. The dimensions of SCI-CASTER prototype 1.9 are given in Figure 3.1.2.
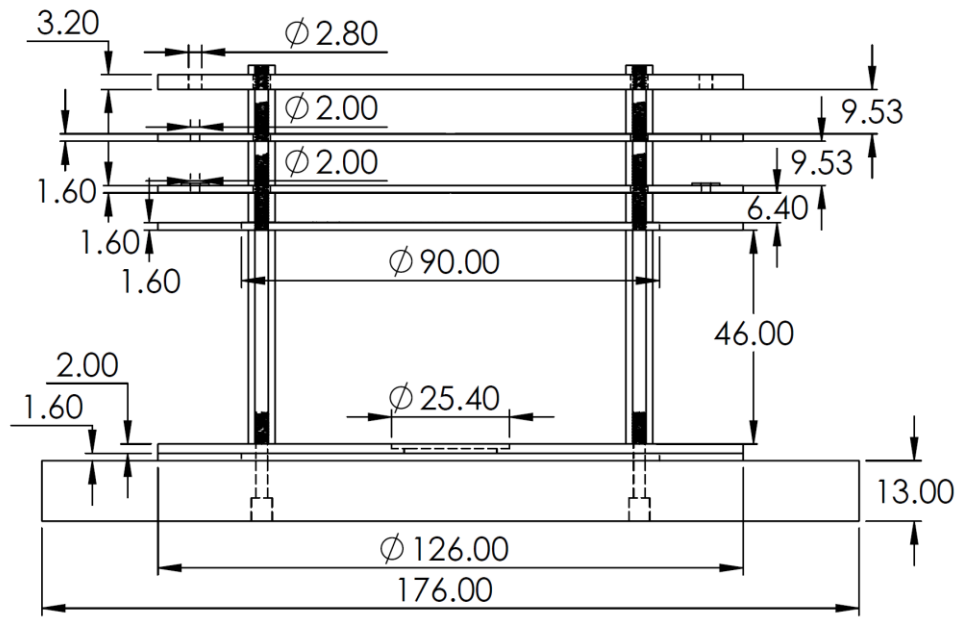
(a) SolidWorks drawing of SCI-CASTER prototype 1.9 with relevant dimensions (mm).
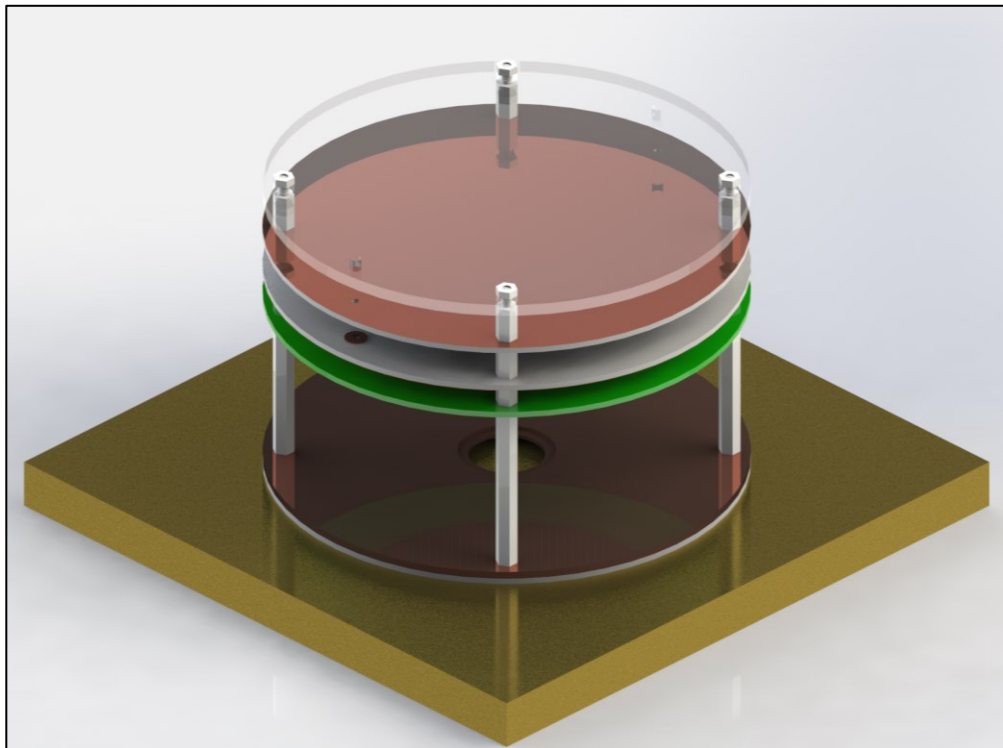
(b) SolidWorks 3D render of SCI-CASTER prototype 1.9.

Figure 3.1.2: Drawing and 3D model of SCI-CASTER prototype 1.9 detector.

Prototype 1.9 has a usable detector radius of 45 mm as limited by the Frisch grid, which was originally produced at TRIUMF for the TIFFIN project. The grid is wound using 0.07 mm diameter wires at a pitch of 1.0 mm. The cathode electrode consists of a solid copper plate with a 25 mm diameter recess to allow for source disk mounting that lies flush with the cathode face. The electrodes are mounted to a solid brass baseplate using stacked nylon standoffs. An important note is that nylon tends to expand as it is exposed to moisture, so this is not an ideal material and will be replaced with a more suitable insulator in subsequent detector designs.

The detector anode, which was originally a solid copper plate, has been replaced by a set of three disks (Figure 3.1.3): a PCB-based anode split into two conductive segments (see Appendix C for production method), a grounding PCB to connect the coaxial anode cable shields, and an acrylic plate to act as a wire guide for the anode cables.
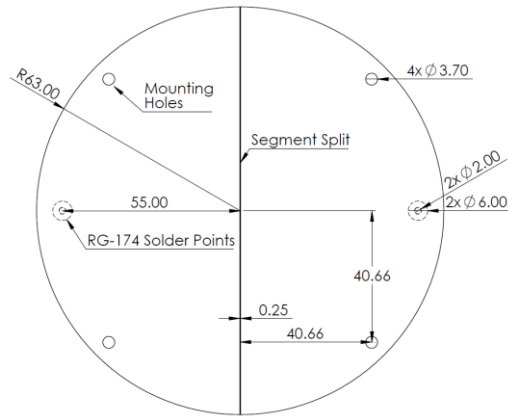
(a) Segmented anode (1/16" PCB).
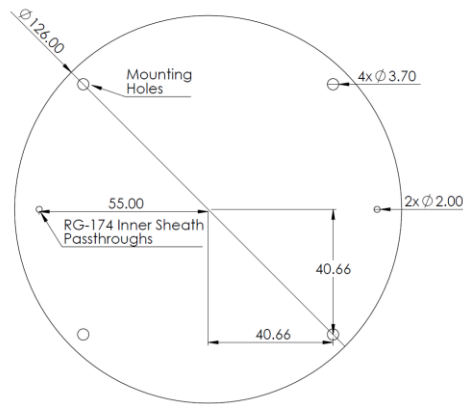
(b) RG-174 coaxial shield grounding plate (1/16" PCB).
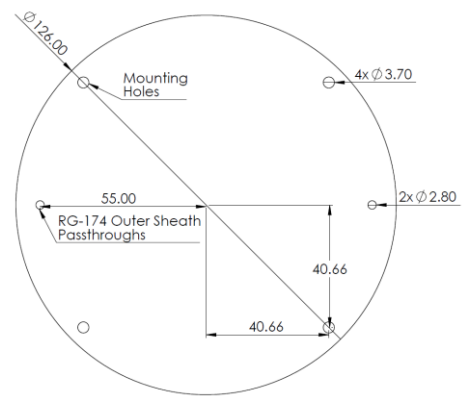
(c) RG-174 coaxial cable wire guide (1/8" acrylic).

Figure 3.1.3: SolidWorks drawings of the three disks that comprise the SCI-CASTER prototype 1.9 anode assembly (mm).

3.1.2. Frisch Grid Inefficiency

An important consideration in detector design is a phenomenon known as *grid inefficiency* [30]. This quantity describes the extent to which the Frisch grid fails to decouple the electric fields of the ionization and collection regions. This in turn results in some fraction of the induced charge on the Frisch grid to be transferred to the anode, therefore yielding a potentially significant positional dependency on the anode charge readout. Grid inefficiency is dependent on the electrode-to-electrode gap of the anode and Frisch grid and the dimensions of the Frisch grid wires, where the inefficiency σ is defined as

$$\sigma = \frac{l}{l + D_{G-A}}, \tag{3.1.1}$$

$$l = \frac{d}{2\pi} \left(\frac{1}{4} \rho^2 - \ln \rho \right), \tag{3.1.2}$$

$$\rho = 2\pi \frac{r}{d}, \tag{3.1.3}$$

where r is the grid wire radius, d is the grid wire pitch, and D_{G-A} is the distance between the Frisch grid and anode. From Equation 3.1.1, grid inefficiency can be reduced either by reducing the grid wire pitch (Figure 3.1.4) or by increasing the grid to anode electrode gap. Either one of these actions has the consequence of necessitating an increase in the detector operating voltage to avoid charge collection on the Frisch grid (Section 3.3.1) and electric field fringing effects (Section 3.3.2). Therefore, care must be taken to ensure that the detector geometry does not make proper HV biasing impossible by either reaching the limits of the HV supply in use or causing arcing in the detector. This is further discussed in Section 3.3.1.
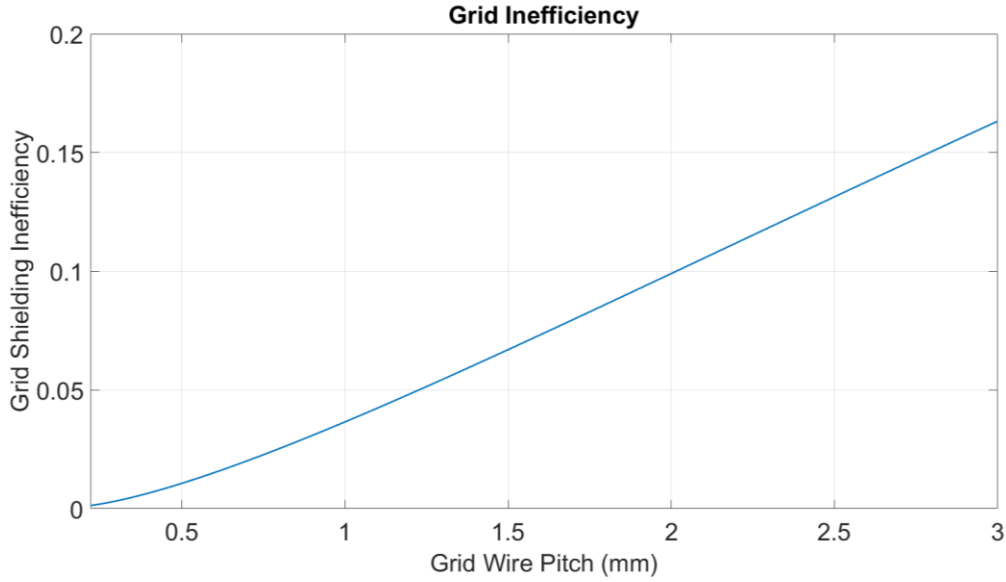
Figure 3.1.4: SCI-CASTER prototype 1.9 grid inefficiency as a function of grid wire pitch. The grid to anode distance is 6.4 mm and the grid wire is 0.07 mm in diameter.

The dimensions of the original TIFFIN detector and now SCI-CASTER prototype 1.9 yield a grid inefficiency of 0.036, meaning that charge drift in the ionization region will likely be visible on the anode signal of the detector. This is not however nearly the detrimental effect it was when the phenomenon was originally published in 1949. At this point in time, measurement of the charge signal from the anode would have been an integral over the duration of an event done by an analog instrument, and therefore the position dependent rise of the anode signal would impact the energy resolution of the readout. By contrast, SCI-CASTER uses modern waveform digitizers which means that the start of charge drift in the collection region is readily identifiable by a significant change in signal slope.

While this dramatically lessens the importance of grid inefficiency on detector resolution, it is still not negligible. Any charge drift occurring in the ionization region, be it from slow drifting ions or a new alpha particle track, will impact the anode signal in a way which may not be easily discerned using waveform digitization.

3.2. Gas Atmosphere Selection

As discussed in Section 2.1, the basis upon which an ionization chamber operates is the ionization of a gaseous medium. The choice of this gas in turn determines how the detector operates and what types of conditions it is optimized for. The goals of the SCI-CASTER project in the NSL require the detector to be optimized for low-rate, high-precision operation. Therefore, argon gas, which has a large W-value, low Fano factor, and small drift velocity is the ideal choice.

3.2.1. The W-Value

The W-value of a gas, which has been mentioned several times thus far, is defined as the average energy required by an ionizing particle to produce a single charge pair in the gas. A low W-value is critical for high-precision measurements as it maximizes the number of charges produced for a given alpha particle energy, and therefore the signal-to-noise ratio of the detector improves. For alpha particles, argon gas has one of the lowest W-values of commonly used gases at 26.3 eV per charge pair, however even under these circumstances, the induced charge remains on the order of femtocoulombs as shown in Section 2.6.

3.2.2. The Fano Factor

The Fano factor provides information on the statistical minimum in achievable detector resolution, meaning that depending on the choice of gas there will be an energy resolution limit irrespective of the design of the detector or electronics. The Fano factor F measured for pure argon gas for 5.3 MeV alpha particles is 0.20 (+0.01, -0.02) [31]. This in turn imposes a maximum energy resolution R_{Fano} in pure argon of

$$
\begin{aligned}
R_{Fano} &= 2\sqrt{2\ln 2}\,\sqrt{\frac{FW}{E}} \times 100\% \\
&= 2\sqrt{2\ln 2}\,\sqrt{\frac{0.20 \times 26.3 eV/pair}{5.3 MeV}} \times 100\% \\
&= 0.23\%.
\end{aligned} \tag{3.2.1}
$$

This limitation on resolution is rarely achievable due to other sources of amplitude fluctuations in the detector system, for example variations in gas purity or pressure and possibly electrical noise.

3.2.3. Charge Drift Velocity and Gas Contamination

The drift velocity of charges in a gas determines the duration of the charge drift throughout the detector. When using a waveform digitizing data acquisition system (DAQ), the number of samples taken of the induced charge signal for a given sampling frequency will increase with the signal length, which from a data acquisition standpoint is considered advantageous. However, the disadvantage of this is that the maximum source activity that the detector can support is reduced. This is because as the drift times increase, the probability of having more than one charge track in the detector volume also increases. The charges from multiple tracks will then drift simultaneously, inducing a signal that is representative of more than one alpha particle and resulting in an effect known as *pileup*. For the current goals of the SCI-CASTER project however, the trade-off in event rate for sampling quality is considered worthwhile as the tracking abilities of the detector are highly reliant on sampling the induced signals from charge drift.

The drift velocity of charges in a pure gas at known pressure in a homogeneous electric field can be found by using Equation 2.5.1 and Equation 2.5.2, where the ion mobility for argon is $\mu = 1.92 \times 10^{-4}$ m²·atm/V·s [32]. The drift velocity is commonly plotted as a function of a value known as the *reduced field*, which is the electric field divided by the gas pressure. Of important note is that for certain gas mixtures, the drift velocity will not monotonically increase as Equation 2.5.1 suggests and will instead have a peak near small values of the reduced field [33]. Effects like this and large increases in drift velocity can be used as a probe for potential gas contamination in the detector.

While an unexpectedly short drift time is an undesirable but manageable effect of mild gas contamination, there are multiple effects that are not. To begin, the W-value of the gas will change and lead to fluctuations in the number of charge pairs created for a given alpha particle energy. Additionally, the stopping distance of an alpha particle is

dictated by the gas type and its pressure, thereby requiring a known gas to set the chamber pressure accordingly. Should the gas be an unknown mixture, the stopping distances may change and have an effect on positional resolution, or in an extreme case, allow alpha particles to escape the detector volume.

Lastly, the most impactful effect of contamination will be that it is likely a time-varying parameter if the contaminant is not present in the gas cylinder itself. This is to say that either the contaminant will be present and slowly purged from the chamber as the fill gas is circulated, or the contaminant will leech into the fill gas over time. Either one of these situations leads to a time-dependent drift time, energy, and track length for a given alpha particle energy, and therefore a worsening of both positional and energy resolution.

3.2.4. Practical Considerations

Among the benefits discussed above, there are two practical benefits to using argon gas that are not strictly related to optimal detector behavior. To begin, argon is non-toxic and non-combustible, meaning that for prototype testing it is considered a very safe option. By contrast, pure methane (used for its high drift velocity) or P-10 (a mixture of 90% argon, 10% methane) are both combustible in air and pose a notable safety concern. Argon is also an affordable and highly available gas, meaning that the purity required to operate a detector that is highly sensitive to gas atmosphere contamination can be easily attained and replenished without significant financial and logistical investment.

3.3. High Voltage Conditions

The HV supplied to the detector is critical for optimal performance, and either unstable or incorrect bias voltages can lead to significant noise injection to the amplification system, charge loss, and damage to the detector electronics.

3.3.1. The Minimum Electric Field Ratio

Alongside grid inefficiency, Reference [30] introduced a minimum condition on the electric field ratio between the collection and ionization regions of the detector. In

principle, the fulfilment of this condition ensures that all electrons that travel towards the Frisch grid will pass the grid wires and enter the collection region. Should the condition be violated, some of the electrons will instead be collected by the Frisch grid, thereby resulting in signal amplitude variations for a given alpha particle energy. Intuitively, fulfilment of this condition can be thought of as ensuring that all electric field lines in the detector are directed from the cathode to the anode, with none terminating on the Frisch grid. The minimum condition is

$$\frac{V_A - V_G}{V_G - V_C} \times \frac{D_{C-G}}{D_{G-A}} \geq \frac{1 + \rho \left[1 + \frac{d}{4\pi D_{G-A}}(\rho^2 - 4\ln\rho)\right]}{1 + \rho \left[1 + \frac{d}{4\pi D_{C-G}}(\rho^2 - 4\ln\rho)\right]}, \tag{3.3.1}$$

where V_A, V_G, and V_C are the anode, Frisch grid, and cathode potentials, D_{G-A} is the distance between the Frisch grid and anode (collection region), D_{C-G} is the distance between the cathode and Frisch grid (ionization region), and ρ is defined in Equation 3.1.3. A visualization of the effect of the field ratio on electric field lines passing through a Frisch grid is shown in Figure 3.3.1.

(a) Field lines passing grid wires.   (b) Field lines ending on grid wires.
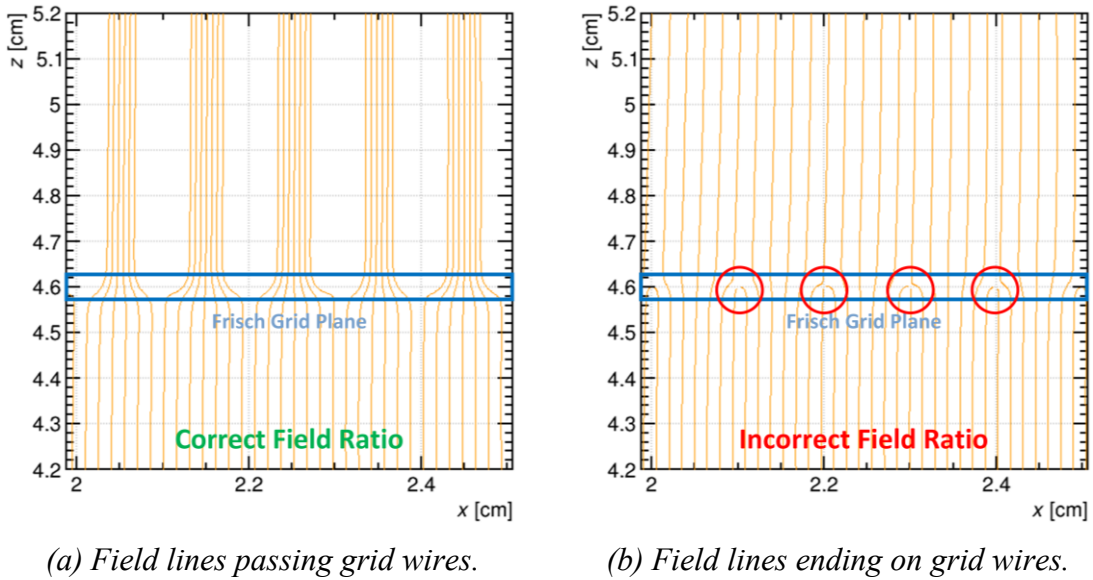
Figure 3.3.1: Garfield++ [34] simulation of field lines passing and terminating on the Frisch grid depending on voltage settings.

The dimensions for the prototype 1.9 detector given in Figure 3.1.3 yield a minimum field ratio of 1.6. While in principle this ratio is sufficient, it has been documented that exceeding of the minimum is required to achieve maximum anode pulse height, and therefore maximum energy resolution [17]. For this reason, the minimum condition was exceeded in all experiments conducted using prototype 1.9, which are discussed in Chapter 7.

The minimum field ratio and associated bias voltage ratio as a function of grid wire pitch for SCI-CASTER prototype 1.9 is shown in Figure 3.3.2. Notice that there is a clear elbow in the plot below which biasing the detector without arcing or experiencing significant fringing effects in the ionization region due to a low electric field (Section 3.3.2) becomes very challenging.

A consequence of charges being collected on the Frisch grid is that there is more charge approaching the grid than leaving it, meaning that the number of charges N changes between time interval 1 (electrons drifting towards the grid) and time interval 2 (electrons drifting away from the grid) presented in Section 2.4. This effect is clearly observable when examining waveforms with polar angles of emission close to 90°, as these will yield positive differences in the Frisch grid baseline, where the difference is taken as the pre-event charge reading subtracted from the post-event charge reading. This is demonstrated by summing Equations 2.4.2 and 2.4.4 for a differing number of electrons N_1 and N_2:

$$
\begin{aligned}
Q_{grid(T2-T1)} &= \frac{N_1 e}{D_{cg}}(v_{electron}t) + \frac{-N_2 e}{D_{ga}}(v_{electron}t) \\
&= \frac{N_1 e}{D_{cg}}\left(D_{cg} - \bar{x}cos(90°)\right) + \frac{-N_2 e}{D_{ga}}\left(D_{ga}\right) \\
&= e(N_1 - N_2),
\end{aligned}
\tag{3.3.2}
$$

where a greater number of charges in the ionization region will yield a positive Frisch grid baseline shift. The significance of charge collection on the Frisch grid can therefore be evaluated by viewing a histogram of the difference between the grid baseline values. An example of this plot is shown in Figure 3.3.3 and was obtained during prototype 1.0 testing.
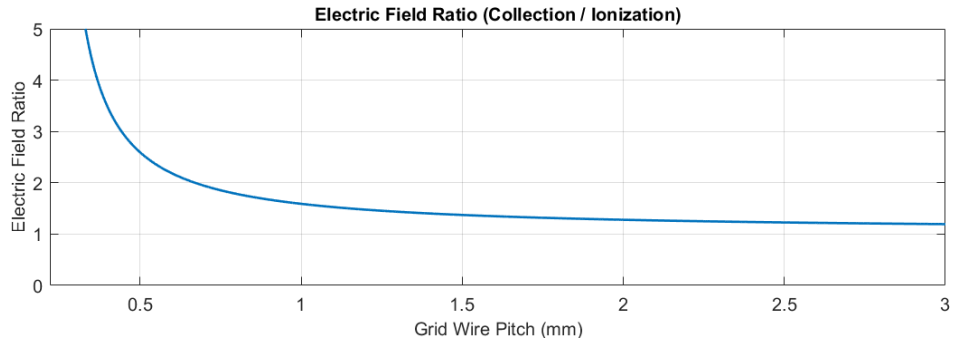
(a) Minimum electric field ratio as a function of grid wire pitch.
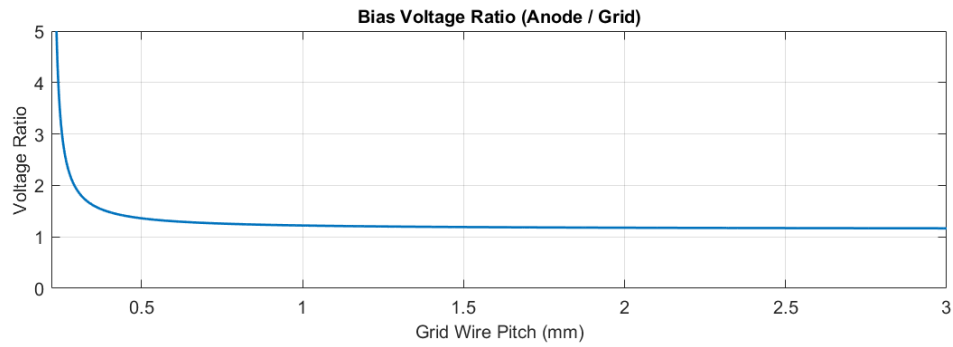
(b) Corresponding bias voltage ratio.
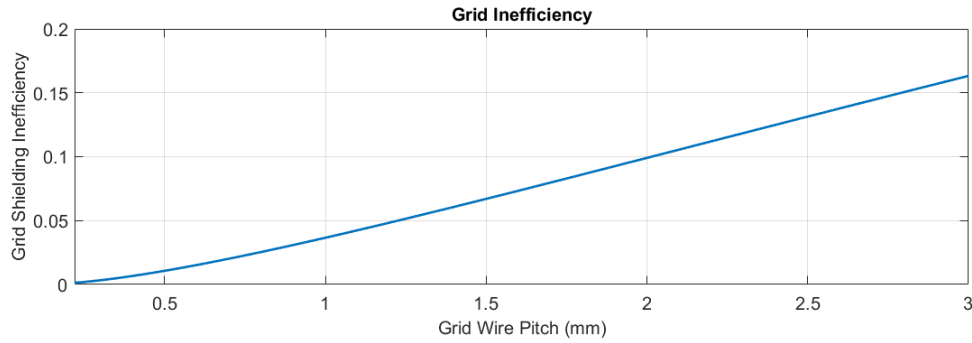
(c) Corresponding shielding efficiency, the same plot is shown in Figure 3.1.4.

Figure 3.3.2: Electric field and bias voltage ratios as a function of grid wire pitch for SCI-CASTER prototype 1.9. The grid to anode distance is 6.4 mm, grid wire is 0.07 mm in diameter, and the grid wire pitch used for prototype 1.9 is 1.0 mm.

31
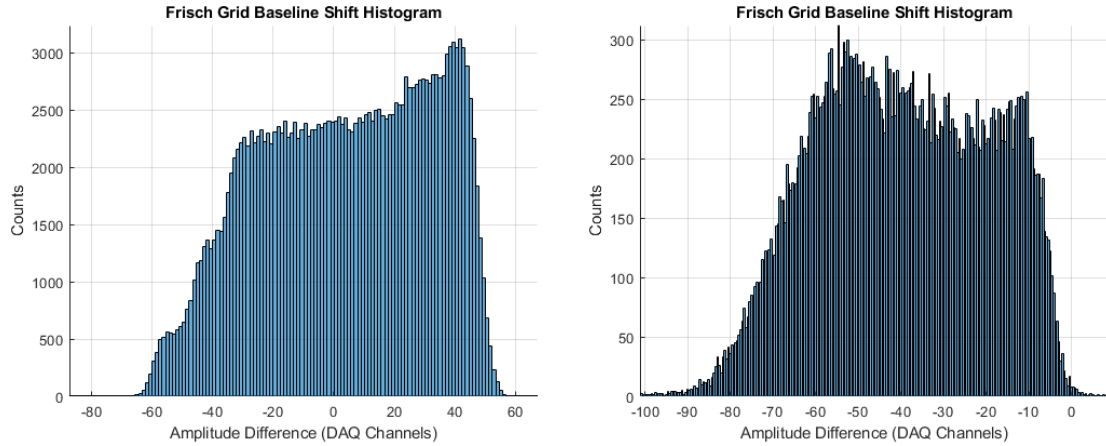
(a) Violation of the electric field condition resulting in charge collection on the Frisch grid.

(b) Exceeding the electric field condition yielded the expected behavior of the detector with no positive shifts.

Figure 3.3.3: Frisch grid baseline shift data from SCI-CASTER prototype 1.0 demonstrating the effects of incorrect bias voltage.

3.3.2. Electric Field Fringe Effects

A concern particularly with the large gap between electrodes in the ionization region is the effect of fringe fields at the outer edge of the detector. The principle of operation of a SCI-CASTER detector is predicated on the fact that the electric fields throughout the detector regions are homogeneous. Violating this will cause issues when conducting drift time studies and possibly create errors under constraints imposed and assumptions made in the waveform analysis algorithms written for the SCI-CASTER project (Chapter 6). A visualization of the fringing effect for the prototype 1.9 detector operating at an anode voltage of 1000 V and a Frisch grid voltage of 700 V is shown in Figure 3.3.4.
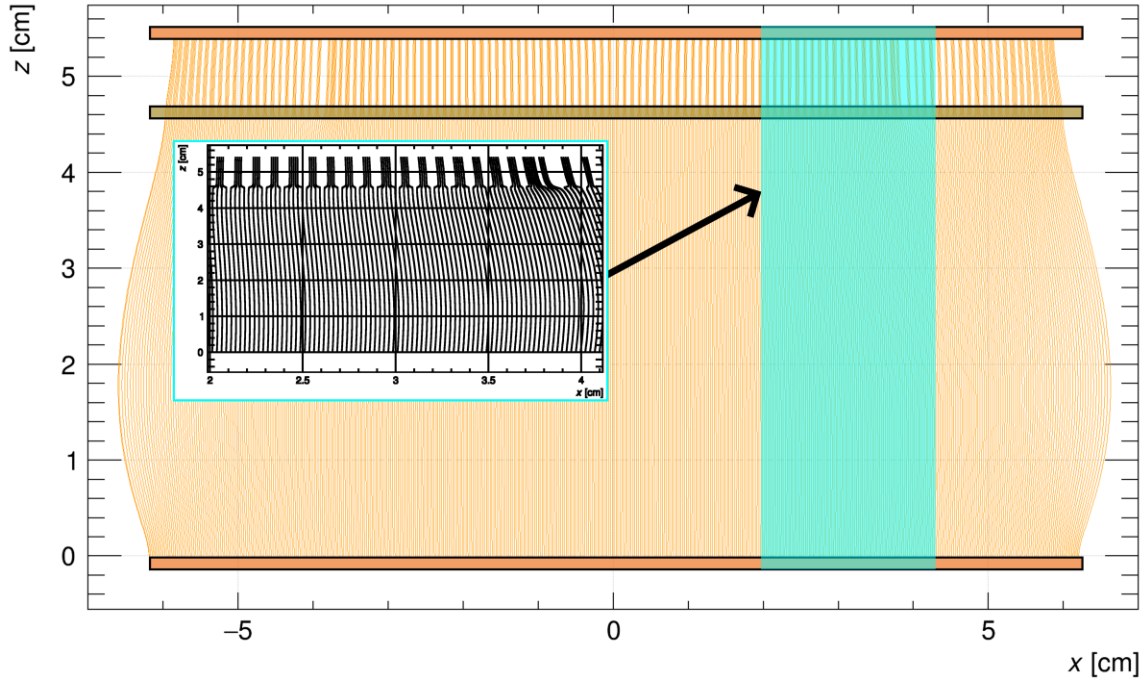
Figure 3.3.4: Fringe fields for SCI-CASTER prototype 1.9 present at the detector edges. Inset shows that the field lines become significantly warped beyond ~3.0 cm from the detector origin.

FGIC detector designs commonly implement conductive strips known as *field degrader rings*. These encircle the ionization region of the detector and are held at intermediate bias voltages such that the electric field is made more uniform, and the fringe fields are minimized. Degrader rings are planned to be added to future SCI-CASTER prototypes, however as a stop-gap measure until this time, the calculated range of the alpha particle tracks have been kept within the uniform field computed by Garfield++ by increasing gas pressure.

Chapter 4.   SCI-CASTER Test Chamber Setup

To facilitate the testing of FGIC prototypes in the SFU NSL, a dedicated test apparatus has been built and permanently occupies a space in the laboratory. Gas system componentry has been reused from the TIFFIN project [29], however, all components have been densified where possible to save space. Computer control and logging systems have been added to ease and better document experiments.

4.1.   Physical Chamber

The SCI-CASTER chamber is mounted on a laboratory bench in the SFU NSL (Figure 4.1.1) and is constructed from heavy gauge stainless steel. This allows it to withstand high operating pressures while being an effective EMI shield and offering some acoustic deadening.

To conserve laboratory space the chamber has been rebuilt to take up less bench length. The chamber was also cleaned while taken apart and every seal was retightened to ensure atmospheric ingress would be kept to a minimum when evacuating the chamber. The chamber is mounted on a spring-loaded anti-vibration table with a layer of Sorbothane dampers between the chamber itself and the table. The main chamber area of 275 mm × 275 mm × 175 mm (L × W × H) is used for the mounting of the detector and electronics. The main chamber is flanked by piping to facilitate electrical connections via a passthrough plate and gas connections for vacuum and argon flow.
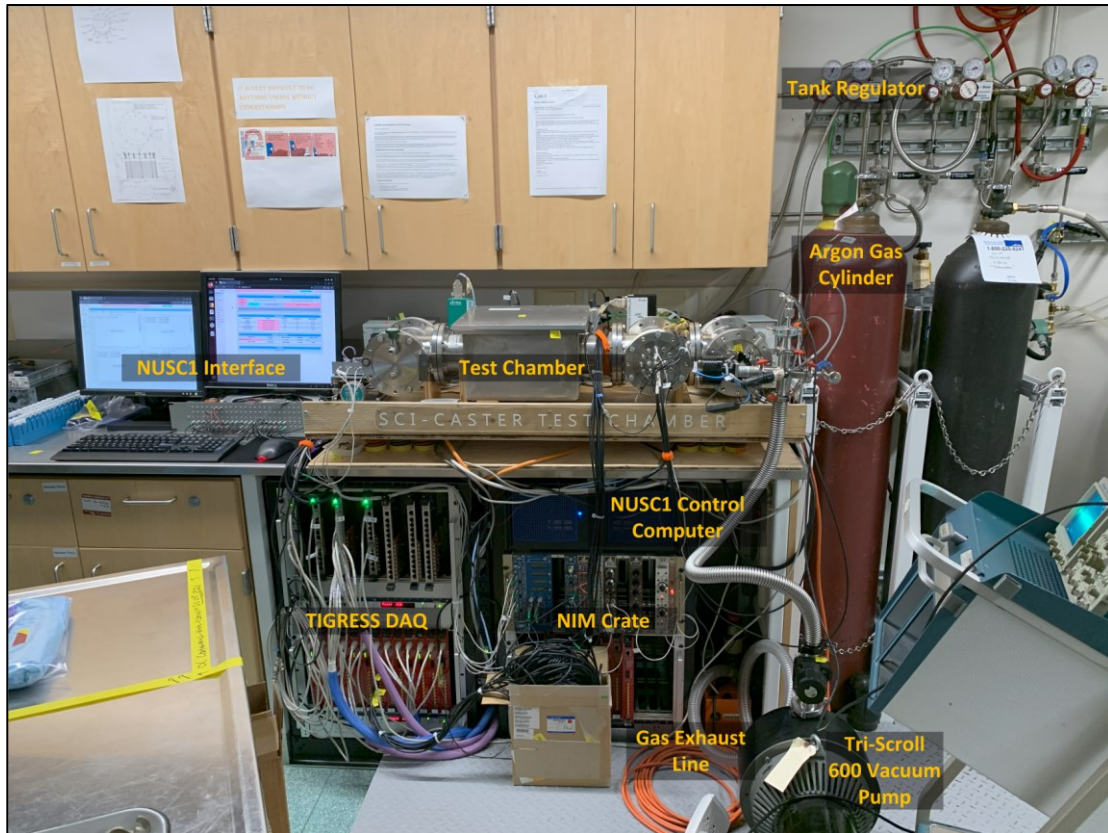
(a) SCI-CASTER test chamber lab area.
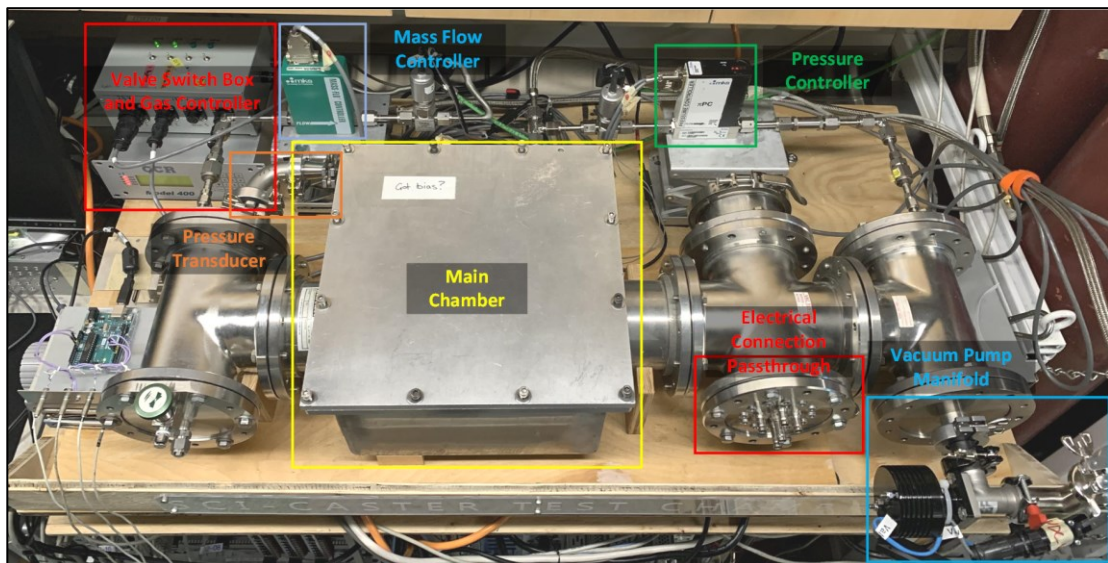
(b) SCI-CASTER test chamber.

Figure 4.1.1: Images of the SCI-CASTER test chamber setup in the SFU NSL.

4.2. Gas Flow System

The gas control system is used to supply argon gas to the detector as well as purge atmosphere from the chamber prior to pressurization. A block diagram of the gas system is shown in Figure 4.2.1.
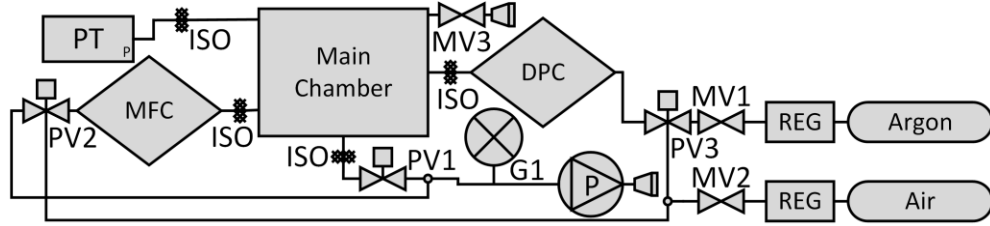
Figure 4.2.1: SCI-CASTER gas system. PT = pressure transducer, MFC = mass flow controller, DPC = downstream pressure controller, P = vacuum pump, G = vacuum gauge, ISO = electrical isolators, PV = powered valves, MV = manual valves, REG = manual-set pressure regulators.

An MKS πPC99 downstream pressure controller [35] and an MKS Type M100B flow controller [36] are used to maintain gas pressure and a consistent flow. An MKS Baratron Type 722B [37] pressure transducer and CCR Model 400 [38] power supply and gas controller are used to provide pressure feedback and control over the gas system. Before pressurizing the chamber, it is necessary to first purge all atmospheric contaminants. This is done via a vacuum manifold that bypasses all gas control systems through an electrically controlled KF25 valve and opens the chamber to the inlet of a Varian TriScroll 600 vacuum pump. The pump is vented from the lab using a radiation-specific exhaust stack to ensure that any possible radioactive contamination of the chamber gas does not enter the laboratory atmosphere. The gas system has demonstrated a maximum operating pressure of ~1750 Torr after rebuilding, which is attributed to the limitations of the chamber O-ring seals.

4.3. High Voltage Supply

The bias voltage necessary for FGICs to operate is supplied by an ISEG NHQ 204M dual-channel bias supply [39], which was selected for its low-ripple characteristics and computer-controlled operation. The supply itself is in a NIM format and is connected to

two SHV passthroughs on the chamber via coaxial cables. The two channels of the supply are used to independently control the anode and Frisch grid voltages, thus allowing for precise setting of the electric fields in the detector.

4.4. Data Acquisition System

The DAQ used for the SCI-CASTER project was originally designed for the TIGRESS detector array at TRIUMF [40]. In its current configuration, the DAQ can accept 120 signal inputs which are digitized with 14-bit resolution at a sampling rate of 100 MHz. The maximum digitization window width of the DAQ is currently 40 µs. The DAQ operates as a hierarchical system as shown in Figure 4.4.1.
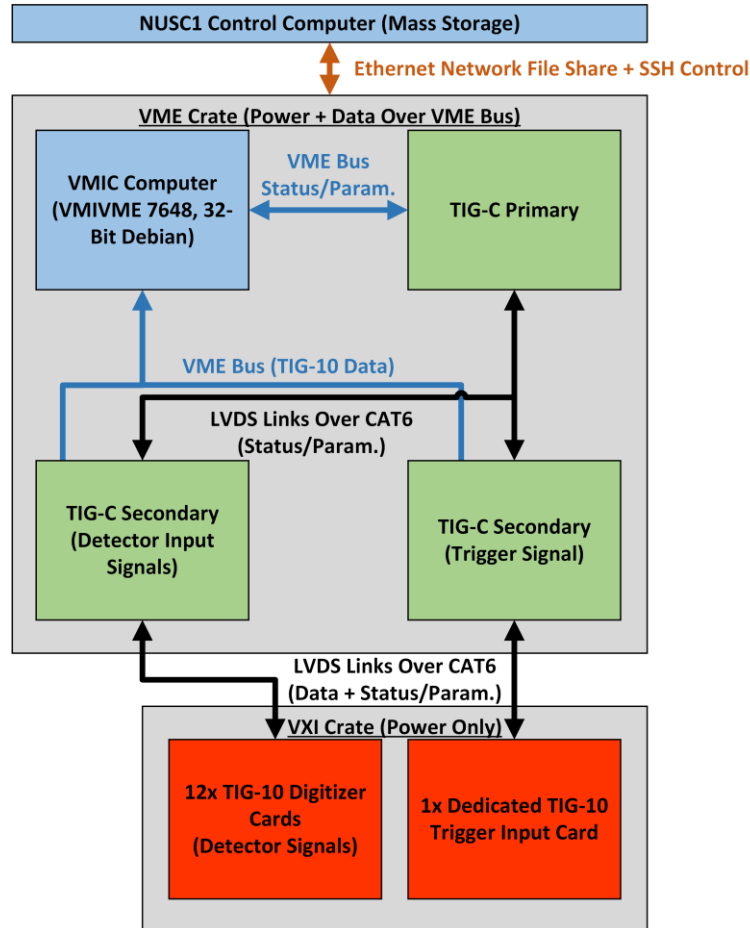
Figure 4.4.1: TIGRESS DAQ structure.

The TIGRESS DAQ takes the amplified output signals from the detector as inputs to the TIG-10 digitizer cards. These house frontend amplifiers, analog-to-digital converters (ADCs), and programmable FPGAs that facilitate communication with the rest of the DAQ. TIG-C cards communicate with the TIG-10 digitizers via LVDS links, which carry both status and data information throughout the DAQ. The TIG-C secondaries then send digitized data to a VME-based computer over the VME bus. The TIG-C primary is solely used for parameter transfer and monitoring of the DAQ.

The VME-based VMIC computer is a single-core computer with limited local storage in the form of a compact flash (CF) card. The local storage holds only the operating system and necessary program files to run the DAQ, and all data is instead directed to a network file share (NFS) hosted on the NUSC1 control computer. NUSC1 is a rackmount server-style Linux computer with bulk enterprise-grade hard disk storage and is responsible for the control and logging of all SCI-CASTER systems via the Maximum Integrated Data Acquisition System (MIDAS) software package [41].

While the current configuration of the DAQ offers up to 120 channels, an upper limit on the number of samples per second is imposed by the processing power of the VMIC computer. This limit has been experimentally determined to be 1.1 mega-samples per second (MSPs), that is, the total number of samples being taken by the DAQ irrespective of the number of channels or number of samples per channel must not exceed 1.1MSPs. Exceeding this value in experimentation has resulted in incomplete events (missing channels), outright DAQ crashes, and in the worst case, desynchronization of the DAQ event buffers (data associated with one event may be assigned to another when saving to disk).

4.5. DAQ Triggering Logic

The TIGRESS DAQ, as configured for SCI-CASTER, requires a single NIM logic level input trigger to fire all enabled DAQ channels. This is done because the signals from the SCI-CASTER detector segments vary significantly depending on the angle of emission of the alpha particle. Therefore, all detector channels, irrespective of their individual

detected signal amplitudes, should be digitized based on the Frisch grid signal alone since this is the only signal that will have a relatively consistent amplitude for each event.

The trigger signal for the TIGRESS DAQ is derived from a duplicate Frisch grid signal generated on the amplifier board of the SCI-CASTER detector (see Section 5.2) using NIM logic modules. A block diagram of the signal derivation is given in Figure 4.5.1.
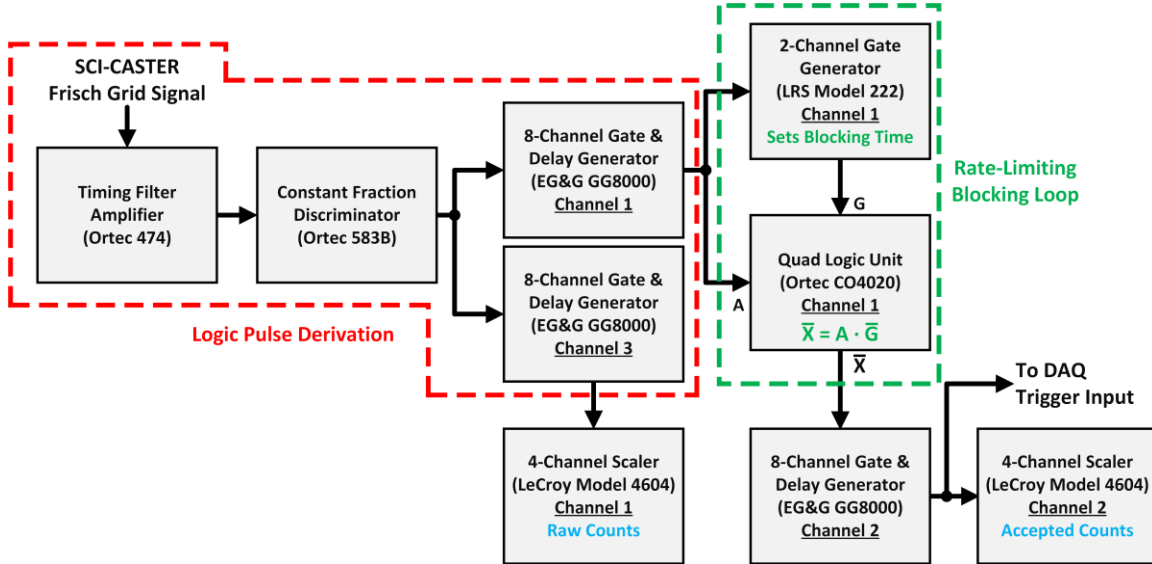
Figure 4.5.1: Triggering logic for the TIGRESS DAQ implemented in NIM hardware.

An Ortec 474 Timing Filter Amplifier (TFA) and Ortec 583B Constant Fraction Discriminator (CFD) are used with a gate and delay generator to create three copies of the raw logical trigger pulse from the detector. The 1st copy is sent to a LeCroy Model 4604 scaler for monitoring of the raw event rate, while the other two are used in a blocking loop configuration to limit the event rate sent to the TIGRESS DAQ. The blocking loop allows a single trigger to pass, after which all subsequent triggers are blocked for a user-specified time which is set by an LRS Model 222 Gate Generator based on the maximum event rate. The passed trigger is sent both to the TIGRESS DAQ as an input as well as to channel 2 of the LeCroy 4604 scaler to monitor the passed trigger rate. The raw trigger rate, passed rate, and rate as monitored by the TIGRESS DAQ can later be used in data analysis or as diagnosis of a fault in the DAQ structure.

Chapter 5. SCI-CASTER Prototype 1.9 Electronic Design

The charge signals from an FGIC, as computed in Section 2.6, are very weak and therefore highly susceptible to electrical and acoustical noise before being amplified. A low-noise highly robust amplification system and HV supply system are therefore required to successfully prepare these signals for digitization. This chapter outlines the design and layout of the circuitry which operates SCI-CASTER prototype 1.9.

5.1. High Voltage Circuitry

The purpose of the HV circuitry in an FGIC detector is to provide bias voltage for the detector electrodes as well as decouple the charge signal from the detector for the amplification system. The schematic of the HV circuitry used for SCI-CASTER prototype 1.9 is shown in Figure 5.1.1 and is based on the application notes provided for the Cremat CR-110 charge-to-voltage converters [42] used in the amplifier circuitry.
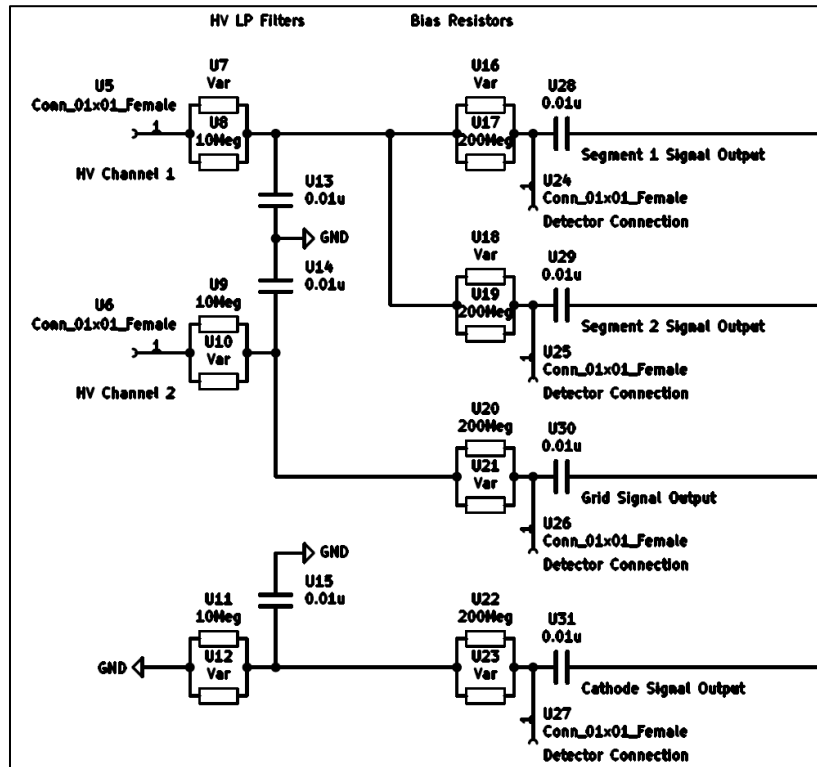
Figure 5.1.1: High voltage circuit schematic for SCI-CASTER prototype 1.9.

The input to the circuit is the HV provided by the ISEG NHQ-204M bias supply and a ground connection for the detector cathode, which is held at 0 V potential. The voltages are then filtered by a 1st order RC lowpass filter with a cutoff frequency of 0.63 Hz and passed through a resistor known as a *bias resistor*. This resistor determines the voltage drop seen by the detector under current draw (drift of charge through the detector) and is selected such that the voltage drop is ~0.5 V as per the application notes. As FGIC detector charge signals are very weak, the largest recommended bias resistor value of 200 MΩ has been used [42].

At this point the bias voltage line is connected to the detector electrodes, which in turn generate AC signals as charges drift through the detector volume. To allow the AC component of the signals to pass while blocking the HV DC component of the bias voltage, 4 kV rated decoupling capacitors are used.

5.2. Amplifier Circuitry

The amplification system used for SCI-CASTER prototype 1.9 is a updated 2-stage design based on the original amplification system designed for prototype 1.0 [28]. The circuit schematic is given in Figure 5.2.1, note that only a portion of the stage 1 and 2 amplifiers are shown to maintain figure clarity.

The 1st stage amplification system takes the decoupled AC charge signals from the detector as an input. There are a total of four input channels to the amplifier circuit, one for each detector electrode: anode segment 1, anode segment 2, the Frisch grid, and the cathode. The 1st stage amplifiers are Cremat CR-110 charge-to-voltage converters, which have a gain of 1.4 V per picocoulomb and a decay time constant of 140 μs as dictated by the 100 MΩ resistor and 1.4 pF capacitor used in the CR-110 internal transimpedance amplifier stage feedback loop [42].
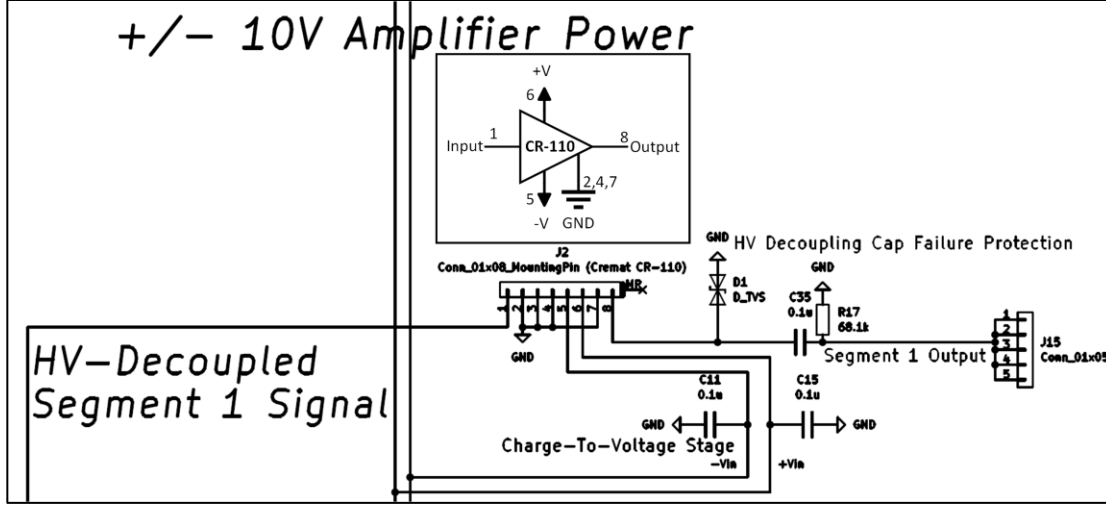
(a) Stage 1 (partial) charge-to-voltage conversion.
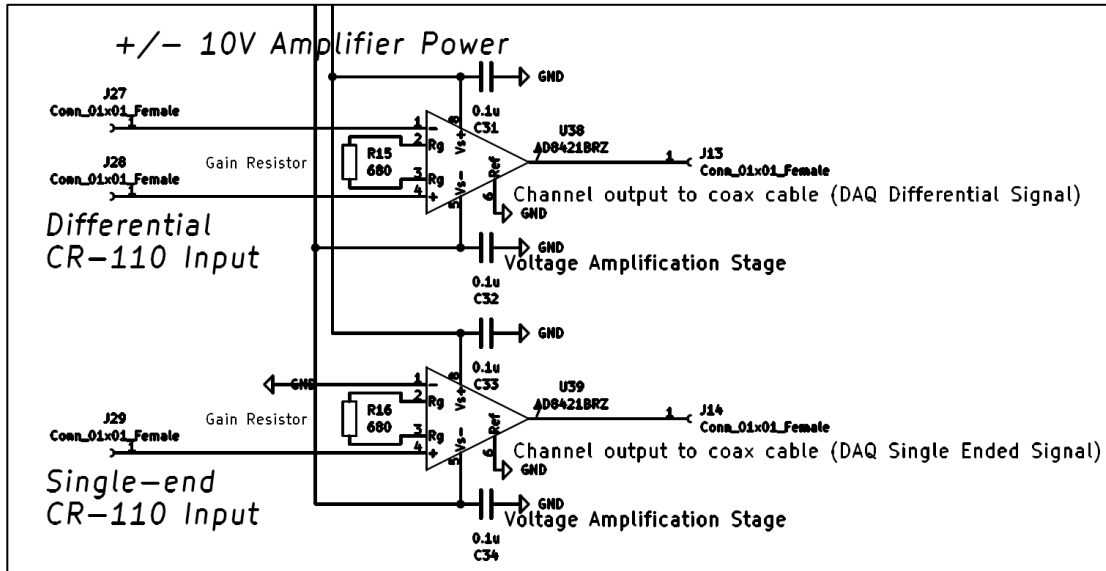
(b) Stage 2 (partial) voltage amplification stage.

Figure 5.2.1: SCI-CASTER prototype 1.9 amplification system schematic.

The outputs of the CR-110 amplifiers are connected to transient voltage suppression (TVS) diodes to prevent large input voltages from reaching the remainder of the amplifier circuitry and DAQ in the event of an HV decoupling failure. Should this occur, the TVS diodes will conduct a path to ground and trip the overcurrent protection of the HV bias supply, thereby shutting down the high voltage. The output signal from the CR-110 amplifiers is DC-decoupled by a 1st order highpass filter with a cutoff frequency of 23.4

42

Hz and is terminated at a 5-pin solder connection point. This has been done due to the limitations of the two-layer board used, which requires the use of coaxial jumper wires to connect stage 1 to stage 2.

The 2nd stage of the amplification system consists simply of Analog Devices AD8421 instrumentation amplifiers [43]. These were chosen based on their high bandwidth of 10 MHz at unity gain, low noise, and high common-mode rejection ratio (CMRR) and are used to drive the 50 Ω inputs of the TIGRESS DAQ directly over coaxial cables. The channels of the stage 2 amplification system are as follows:

Channel 1: Anode segment 1 single-ended

Channel 2: Anode segment 2 single-ended

Channel 3: Frisch grid single-ended

Channel 4: Cathode single-ended

Channel 5: Anode segment 1 / Frisch grid differential-mode

Channel 6: Anode segment 2 / Frisch grid differential-mode

Channel 7: Frisch grid / cathode differential-mode

Channel 8: Duplicate single-ended Frisch grid signal for NIM triggering system

The gain of the amplifiers is set by a 680 Ω resistor, yielding a 2nd stage voltage gain of 13.6. This value was selected based on the maximum realistic input signal expected to be seen by the detector, which can be found from Equation 2.6.1 for an alpha particle energy of 5.8 MeV yielding 0.0353 pC, or 49.4 mV after stage 1 amplification. The TIGRESS DAQ can accept a symmetrical bipolar signal that is a maximum of 672 mV peak-to-peak as limited by the positive DC offset that can be applied to each DAQ channel. A gain of 13.6 results in a maximum input signal amplitude of 672 mV, which aligns with the TIGRESS DAQ input limits.

5.3. Voltage Regulation Circuit

A linear regulation circuit designed to provide +/-10 V to future highly segmented SCI-CASTER detectors was used for prototype 1.9 as a test. The circuit schematic is given in Figure 5.3.1.
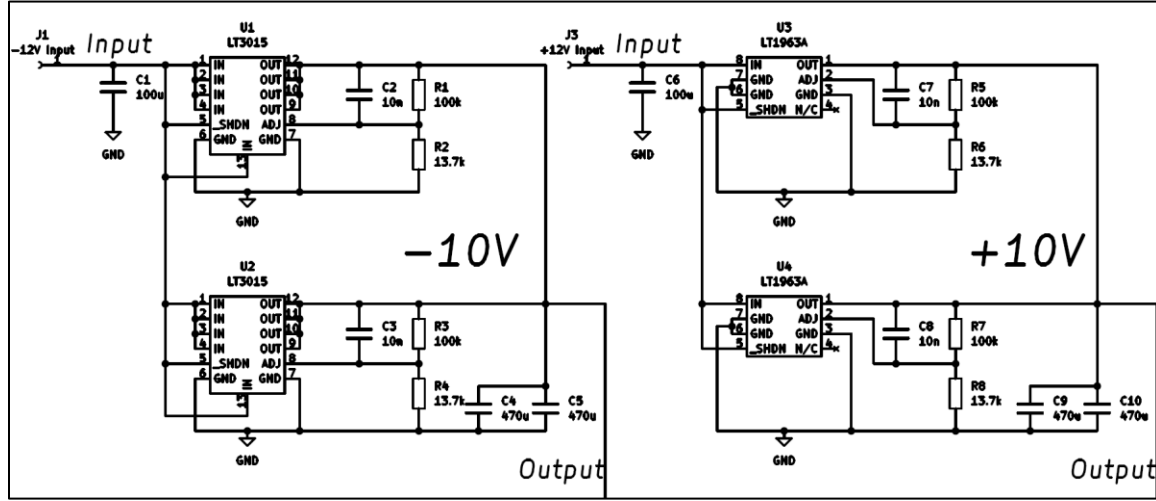
Figure 5.3.1: Linear voltage regulation circuit for SCI-CASTER prototype 1.9 amplifier power.

The required +/-12V input power is supplied by an HP 6236A power supply and is delivered to the circuit over coaxial BNC cables. The circuit has been designed according to the application notes provided by Analog Devices [44], [45] for a doubling of the maximum current by parallel connection of two regulators. Oversize tantalum output capacitors were added to the design to maintain voltage stability for simultaneous full-scale outputs on multiple channels.

5.4. SPICE Simulations

The circuitry presented thus far was simulated using LTSpice prior to assembly to ensure expected performance. The SPICE models used were either preexisting in LTSpice or taken from manufacturer websites in the case of the Cremat CR-110 and TVS diode. The detector was modeled as a current source with an estimated capacitance to ground of ~3.0 pF based on modelling the detector as a simple parallel plate capacitor. The current source waveform was determined by considering the expected charge drift throughout the

detector. For 5.8 MeV alpha particle, it is known the charge generated in argon gas is approximately 0.0353 pC, and that the drift time throughout the detector will be on the order of microseconds, suppose this is a 2 µs signal duration. Knowing that charge is the integral of current and that the charge signal in the case of the anode is a positive-slope ramp function, the corresponding current signal will be a current pulse 2 µs in duration with an amplitude equal to the slope of the charge ramp (17.65 nA).

Such a signal simulated in LTSpice is shown below (Figure 5.4.1) alongside the output voltages of the stage 1 and stage 2 amplifiers, which demonstrate correct functionality.
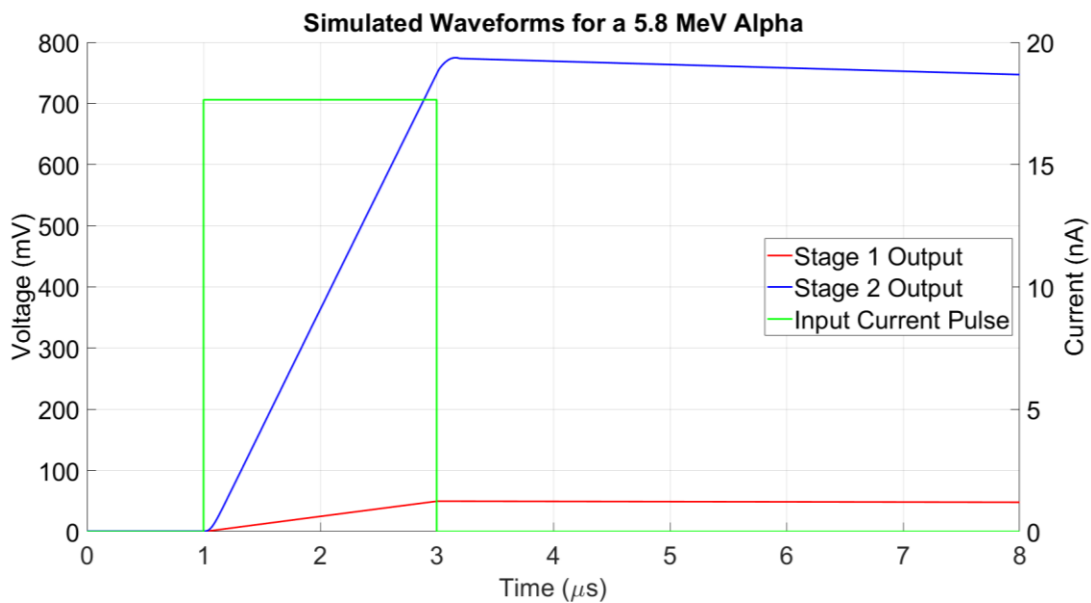
Figure 5.4.1: LTSpice simulated 5.8 MeV alpha particle in argon gas, drifting for 2.0 µs.

Additionally, a Bode magnitude and phase plot was created using LTSpice for an input voltage source to characterize the amplification channel response (Figure 5.4.2).
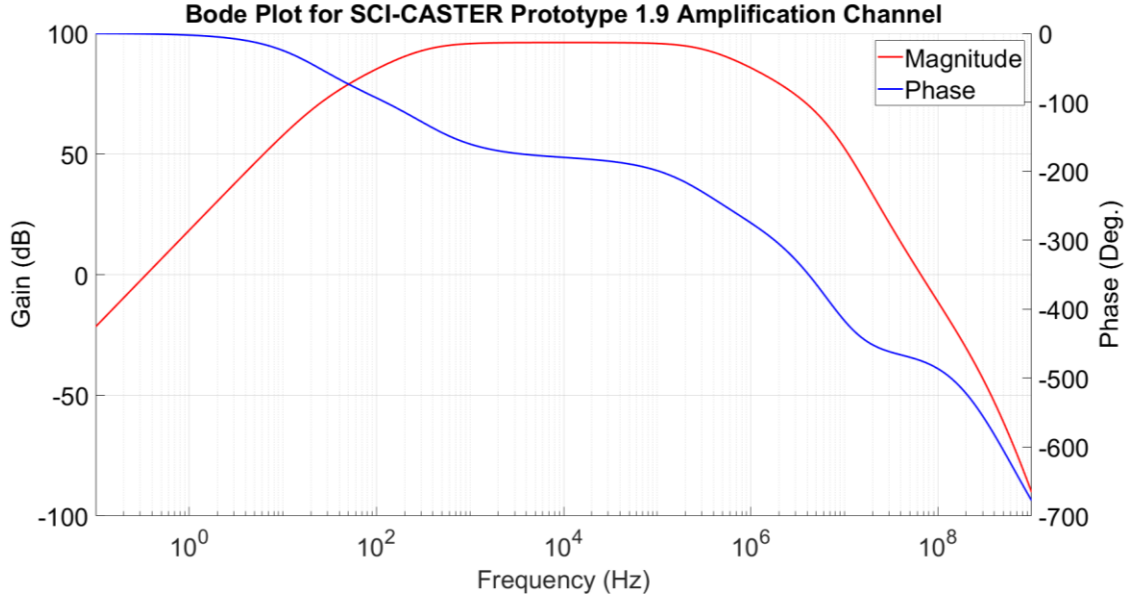
Figure 5.4.2: LTSpice bode magnitude and phase plot for a SCI-CASTER prototype 1.9 amplification channel.

5.5. Board Layout and Physical Characteristics

The layout of the circuit board housing all circuits discussed thus far is shown in Figure 5.5.1. The top side of the board (through-hole component side) consists of an unbroken ground plane, and the bottom side uses ground planes between all traces where possible. The HV section of the board has ground planes removed to minimize the chance of arcing, and all coaxial cable used for the detector connections and stage 1 to stage 2 jumper wires is RG-174. The circuit board is mounted in an acrylic caddy adjacent to the detector in the main chamber and utilizes a grounded stainless-steel shield to isolate it from the detector (Figure 5.5.2).
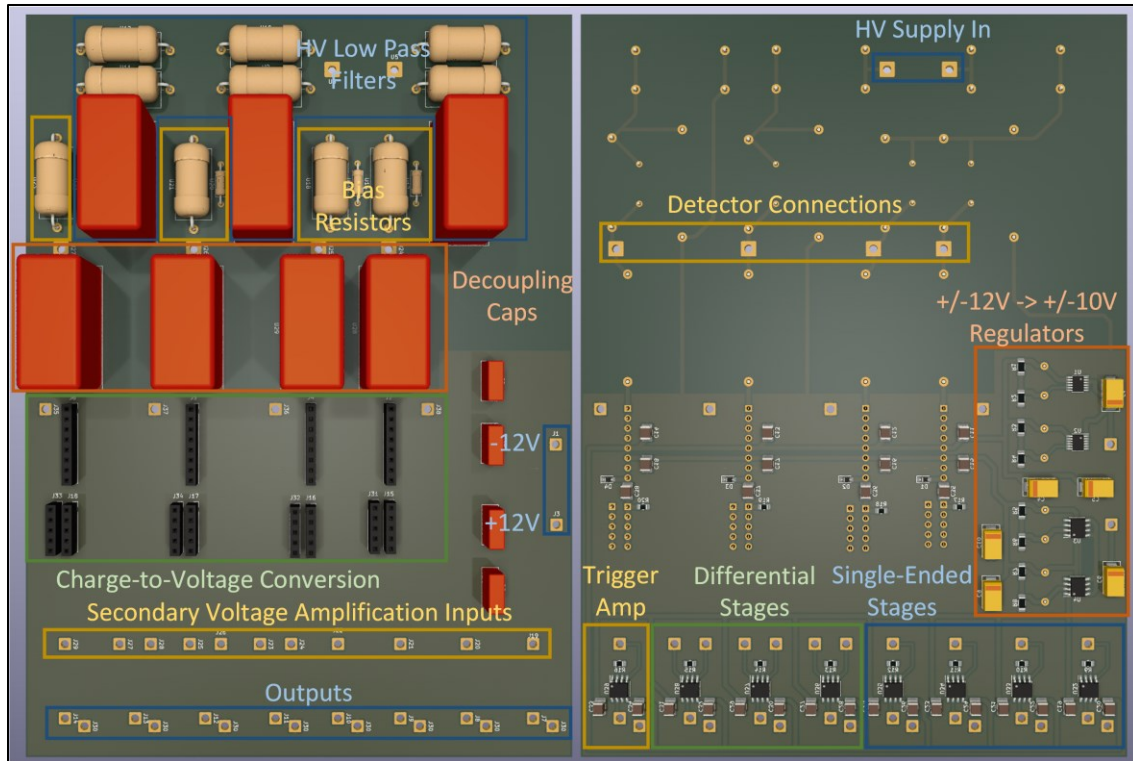
Figure 5.5.1: SCI-CASTER Prototype 1.9 circuit board top (left) and bottom (right).
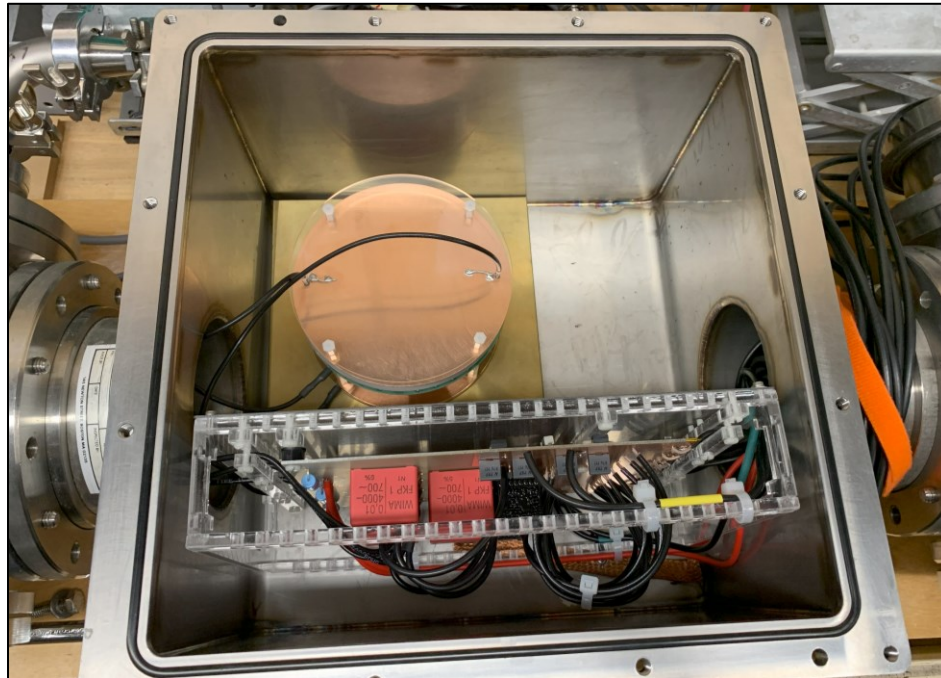
Figure 5.5.2: SCI-CASTER prototype 1.9 detector and circuitry mounted in main chamber.

Detector cable connections were made using soldered ring terminals for the Frisch grid and cathode. For the anode, a low-temperature solder backfill was used to connect the coaxial cables to the anode segments (this is further discussed in Appendix C). All HV connections were made using the ball soldering technique to limit HV discharges at solder joints.

5.6.   Power On Tests

Initial testing of the circuitry revealed that when connected to the detector the circuitry would become unstable to the point of saturating all amplifiers on the board. This would further cause a large power draw and generate a considerable amount of heat in the voltage regulation stage. Despite different shielding and grounding techniques, it was determined that the only method of reducing the noise to an acceptable level was to remove the CR-110 amplifier connected to the detector cathode. It is suspected that due to the presumably large amount of noise on the ground plane of the board and the high gain of the CR-110 amplifiers, the effectively grounded input of the cathode CR-110 would result in an output signal large enough to interfere with all other amplifiers on the board and cause instability throughout.

With the cathode amplifier removed, the noise fell below 30 mV peak-to-peak on the instrumentation amplifier output when using a 50 Ω termination. Oscilloscope waveforms of both the anode segment 1 signal and Frisch grid signal with the detector in an idling state (no radioactive source) are shown in Figure 5.6.1.
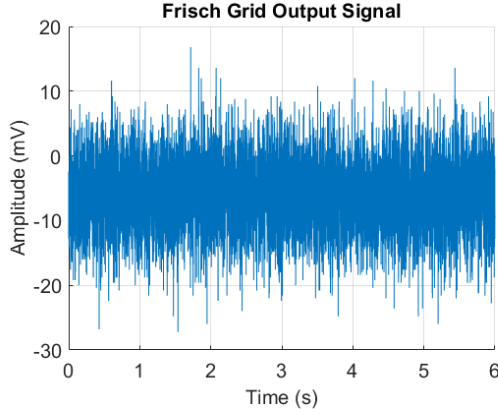
(a) Frisch grid signal, 1.0 s / division.
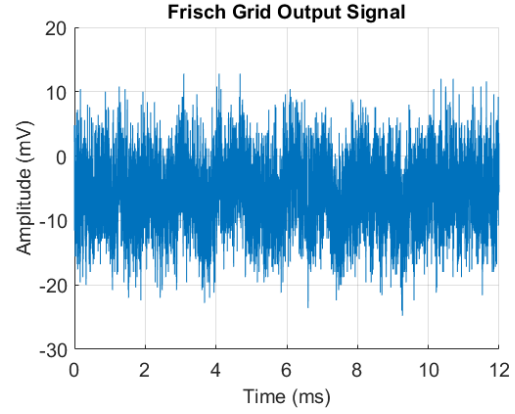
(b) Frisch grid signal, 2.0 ms / division.
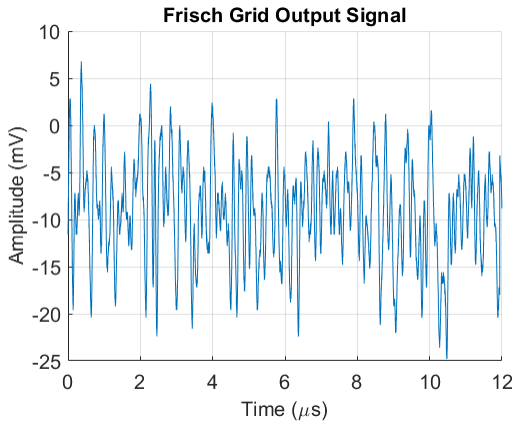
(c) Frisch grid signal, 2.0 µs / division.

(d) Frisch grid signal, 1.0 µs / division.

Figure 5.6.1: Oscilloscope waveforms of the Frisch grid signal while detector is idling.

An attempt to characterize the noise was made by using a 9 kHz – 3 GHz capable spectrum analyzer. The frequency spectra for two frequency spans are given in Figure 5.6.2. The noise appears to be a low-frequency continuum with a prominent peak at 5 MHz, the spectra were unchanged regardless of whether the HV supply, NUSC1 computer, or TIGRESS DAQ were on or off.
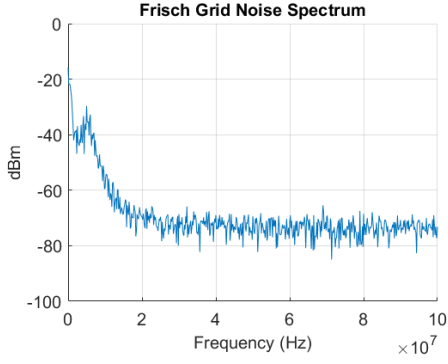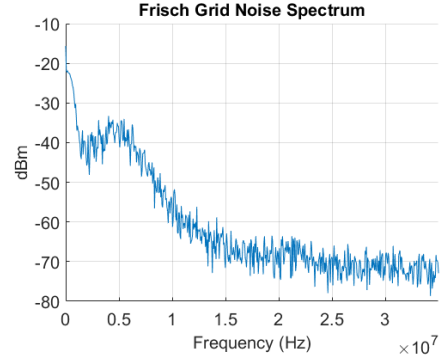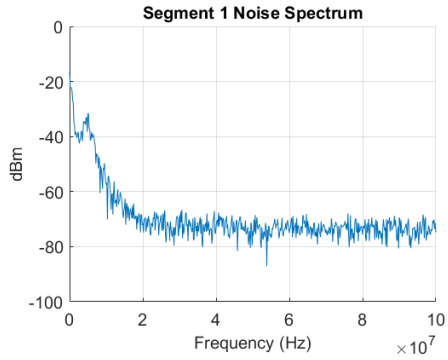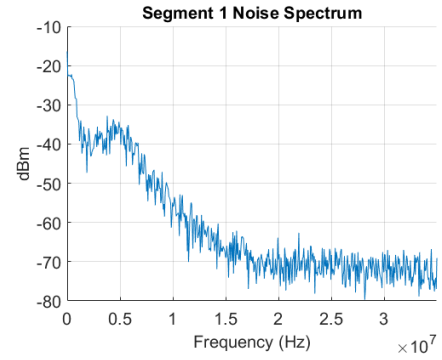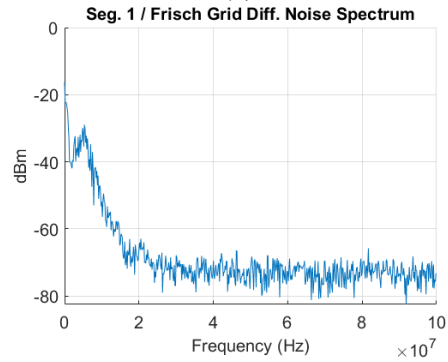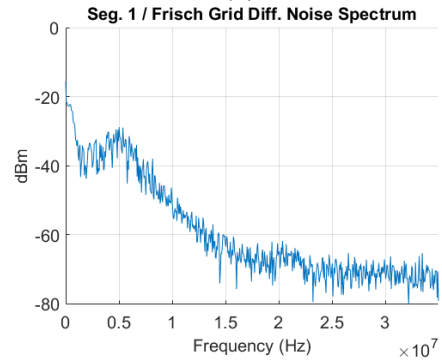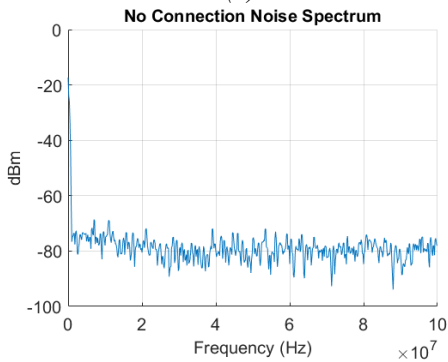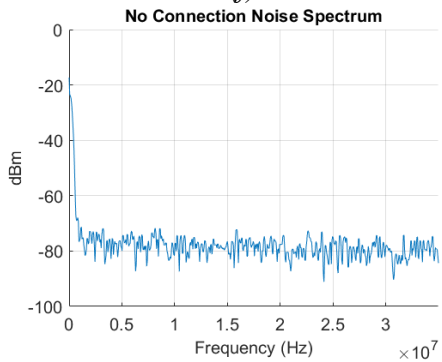
Figure 5.6.2: Spectra of noise on (a, b) the Frisch grid, (c, d) anode segment 1, (e, f) anode segment 1 / Frisch grid differential signal, and (g, h) with no connection to the detector.

Chapter 6.　　Data Analysis Methods

Data produced by the TIGRESS DAQ is stored in *.mid* files, which are generated by the MIDAS data acquisition software and contain encoded information from the DAQ in the form of fragments. In the case of the TIGRESS DAQ and its TIG-10 digitizer cards, each fragment is associated with a TIG-10 input channel and contains

- The ID of the DAQ input the fragment came from: TIG-10 port, TIG-10 number, TIG-C number, and global DAQ channel number,

- Readouts from the online filtering algorithm including the determined charge and CFD readout, which are not used for SCI-CASTER,

- The timestamp that indicates when the fragment was digitized and the associated global trigger number,

- The waveform length and corresponding digitized 14-bit samples.

Since SCI-CASTER relies solely on the interpretation of the digitized waveforms, the waveform data encoded in the *.mid* files needs to be extracted and converted into signal amplitude and timing parameters such that useful interpretations of the data can be made. This is done using a 2-step process in C++ code consisting of first extracting complete and valid events from the *.mid* files, and subsequently sending these events to a waveform analysis program for parameter extraction.

6.1.　Valid Event Extraction

The encoded .mid output files generated by MIDAS need to be decoded such that complete events can be assembled from multiple individual fragments. This is done by grouping events with matching trigger numbers together such that the waveforms for all SCI-CASTER amplifier channels are accessible and associated with a single alpha particle track.

To begin, the active DAQ channels are specified along with the electrode type of the channel (ex. anode, Frisch grid, cathode, etc.) in an input text file read at the start of the program. This can be thought of as mapping the known detector signal output to the

physical input channel of the TIGRESS DAQ. To be considered a complete event, a given trigger number must have associated fragments from each active channel. This condition is checked by iterating through the *.mid* data file fragment by fragment, where depending on the fragment trigger number, either a new entry is made or the fragment is added to an existing entry in a buffer of fragment vectors indexed by DAQ global trigger number. This buffer is required since it is not guaranteed by the TIGRESS DAQ that fragments with matching triggers will be contiguous in the *.mid* file data stream.

Each time the buffer is checked for a matching trigger number for the current fragment, a counter is incremented for each currently buffered trigger such that should an event be incomplete for a certain number of buffer checks (for example, 1000 checks), the event is considered incomplete and deleted from the buffer as it is likely a fragment was dropped due to an error in the digitization process.

Should an event be found complete, that is, all expected fragments based on the known active channels are present in the buffer, the event is checked to ensure that all fragments are of the correct waveform length as determined by the set length in the MIDAS interface. Should any fragments have a waveform of 0 length or should the length deviate from the expected value, the entire event is dropped. However, if the waveforms are of the correct length, the event is passed to the waveform analyzer.

6.2. Waveform Analysis

The waveform analyzer program is responsible for fitting the waveforms generated by the SCI-CASTER detector. The algorithm is reliant upon the fact that all waveforms expected from the detector are present, hence the required preprocessing done in Section 6.1. The waveform analyzer program has been written by Professor Krzysztof Starosta and implements a piecewise function consisting of 4 1st order polynomials and 3 3rd order polynomials determined by polynomial regression. The type of fit and its utilization in the waveform analysis algorithm is determined by the fit type specified in the input text file discussed in Section 6.1. A flowchart for the waveform analysis algorithm is shown in Figure 6.2.1.
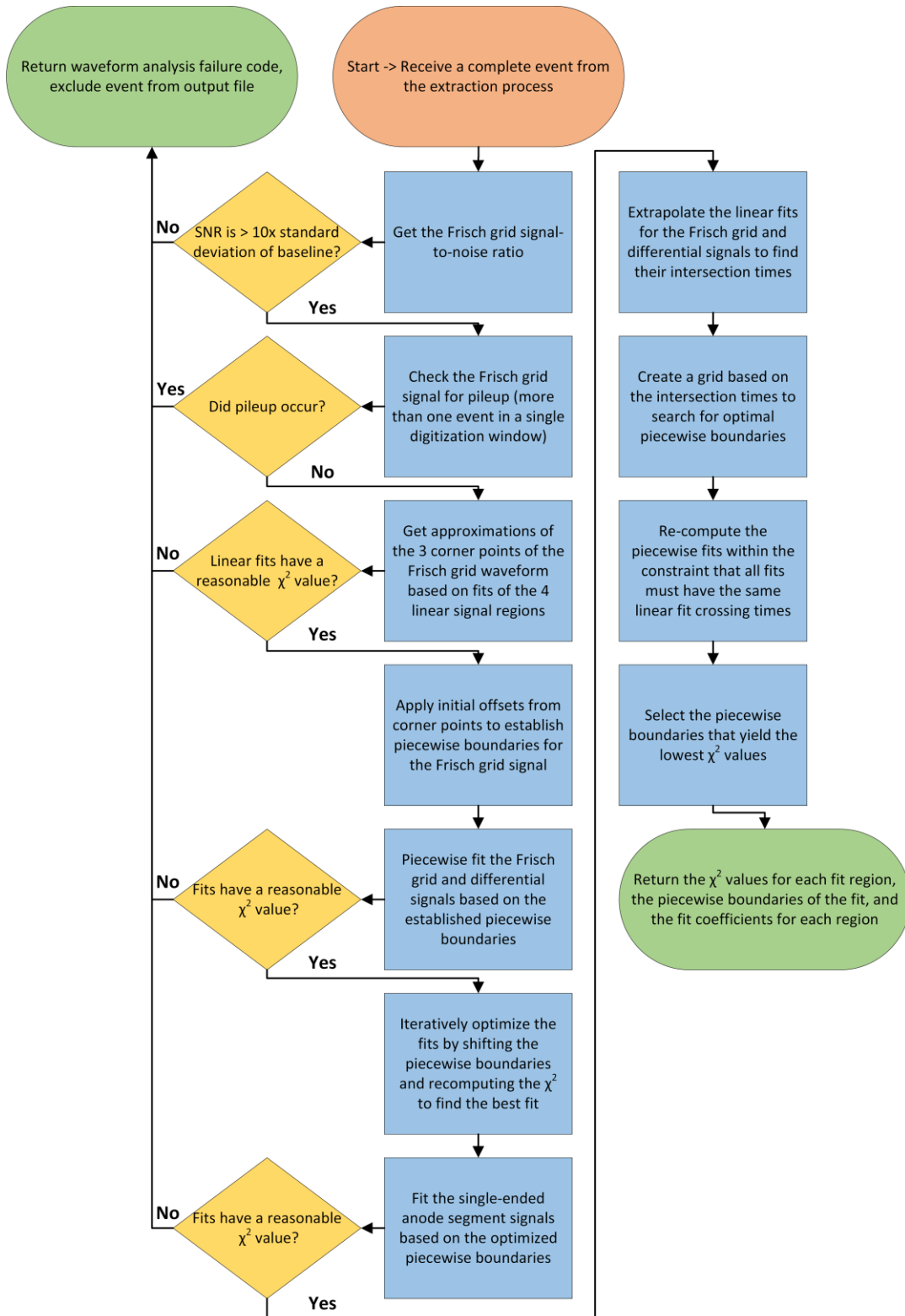
Figure 6.2.1: Flowchart detailing the function of the waveform analysis algorithm used for SCI-CASTER prototype 1.9.

53

6.3. Data Analysis Output Files

Complete events that have successfully been processed by the waveform analyzer are written to disk in the form of a .csv file containing the event trigger number, DAQ channel number for each fit, χ^2 goodness-of-fit measure for each piecewise region, and times and fit coefficients for each piecewise region which are used to reconstruct the waveform. Shown below (Figure 6.3.1) is an example of the fits determined by the waveform analyzer overlaid on the raw data they were derived from.
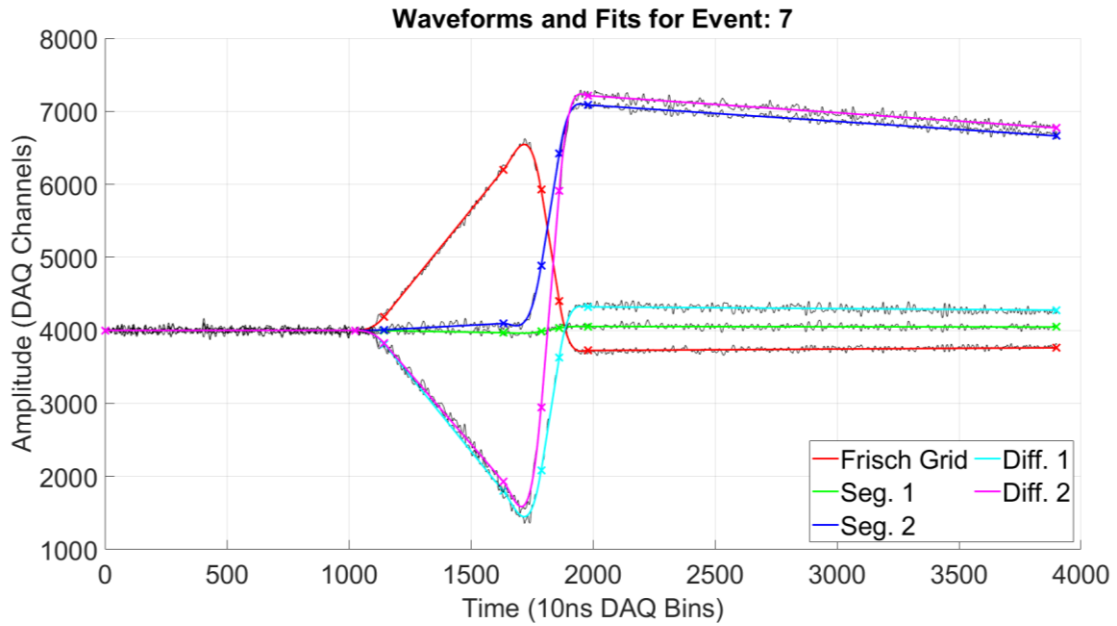
Figure 6.3.1: Example waveforms and their associated fits overlaid on top for a single event. The baseline values of each channel has been recentered at 4000 DAQ channels for consistency.

In addition to the output file, a report of the number of events dropped during decoding and analysis and the reason for their deletion is included. This is done to ensure that no appreciable number of events is being lost to a specific failure, for example, a large fraction of events missing active channels may point to a failure of the DAQ itself. The report printed by the analysis program is as follows:

- Total number of fragments seen,

- Fragments dropped due to the fragment being from an inactive channel,

- Total number of events seen,

- Events eliminated due to a missing channel (fragment lost),

- Events eliminated due to a fragment waveform length of 0,

- Events eliminated due to a fragment waveform length discrepancy,

- Events eliminated due to a failure of the waveform analyzer,

- Total number of events successfully fit and written to disk,

where the total number of events seen should be equal to the sum of dropped events and successfully processed events. Report print-outs for the three experiments discussed in Chapter 7 are given in Table 6.3.1.

Table 6.3.1: Results from waveform analysis for the three experiments conducted with SCI-CASTER prototype 1.9.

Value	Experiment 1	Experiment 2	Experiment 3
Fragments seen	203432	202680	203968
Fragments dropped / inactive channel	0	0	0
Events seen	25429	25335	25496
Events eliminated / missing channel	0	0	0
Events eliminated / waveform length 0	0	0	0
Events eliminated / waveform length discrepancy	0	0	0
Events eliminated / analyzer failure	1460	1631	1038
Events fit and written to disk	23969	23704	24458

Chapter 7.   Experimental Procedures and Results

Three successful experiments have been conducted using SCI-CASTER prototype 1.9 in the SCI-CASTER test chamber setup. The goals of these tests were to validate the detector's sensitivity to the azimuthal angle of emission of alpha particles, ensure its sensitivity to alpha particle energy, and confirm that the drift time of the electrons in the detector was in line with expected values. This last point is of particular importance since future experiments may take place over days or weeks and stability of electron drift velocity is a direct indicator of gas pressure and purity.

7.1.   Experiment Parameters

The radioactive source used for the experiments is an Eckert & Ziegler model QCRB2508 electroplated triple-alpha source [46]. The source has a 5 mm diameter active area which is deposited on a 25 mm diameter metal disk. The source is comprised of ^{239}Pu, ^{241}Am, and ^{244}Cm at 1 kBq activity per isotope, with quoted linewidth below 20 keV. The activity of this source is far higher than this SCI-CASTER detector was intended to be used with, and as such frequent occurrences of pileup are expected due to the relatively low drift velocity of electrons in pure argon.

The gas used in the experiments is Praxair Ultra High Purity 5.0 99.999% argon supplied in a T-type gas cylinder. The gas pressure has been selected based on the range of alpha particles in argon gas and consequently the depth of penetration of the alphas into the ionization region of the detector. The primary concern is that the alpha particles, when emitted at grazing angles, will reach the outer edge of the detector and into areas which have significant electric field nonuniformities, in turn warping the detector signals.

The lowest voltage for the experiments was chosen to be 700 V and 1000 V for the Frisch grid and anode, respectively, which yields an electric field ratio of 3.0 and therefore far exceeds the minimum value of 1.6. For these bias voltages, the Garfield++ simulation of the detector in Figure 3.3.4 indicates that ranges beyond 3.0 cm would experience significant nonuniformities in the electric field. To ensure that the alpha range stays below

this, NIST ASTAR [47] was used to find the projected range of alpha particles in argon gas. From the projected range r, the alpha particle range a can be computed from

$$a = \frac{r}{\rho},$$
(7.1.1)

$$\rho = \frac{mP}{RT},$$
(7.1.2)

where ρ is the gas density, m is molar mass, P is pressure, R is the ideal gas constant, and T is temperature. A plot of the ranges for a 5.8 MeV alpha particle in a variety of gases is given in Figure 7.1.1, and from this an argon pressure of 1400 Torr as a minimum was selected and used for experiment 1.
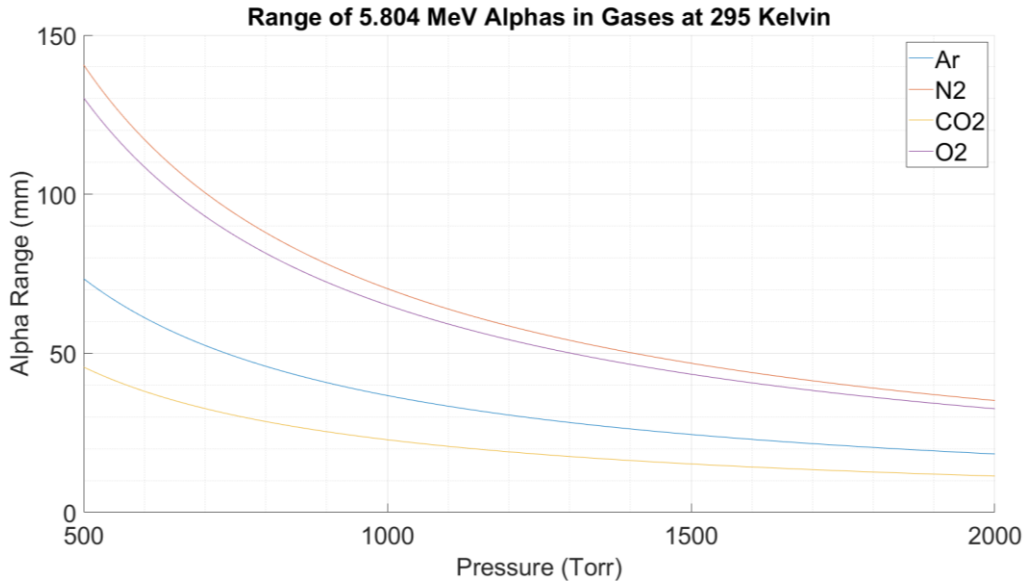
Figure 7.1.1: Alpha particle stopping ranges in a variety of gases.

Experiment 2 used the same argon pressure of 1400 Torr, however the bias voltages were increased to 1000 V for the Frisch grid and 1300 V for the anode, resulting a lower electric field ratio of 2.16. This was done to examine any effect a stronger ionization region electric field may have on detector performance as well as examine the effects of running the detector closer to the minimum field ratio.

Experiment 3 returned the bias voltages to those of experiment 1, however the gas pressure was increased to 1700 Torr. The expected effect of doing this is the shortening of alpha particle track lengths by ~4.6 mm, which should in turn result in a smaller discrepancy in induced signals from tracks with different angles of emission. As an extreme example, one can imagine increasing the pressure to a point where the track length is reduced to 1.0 mm, meaning that there would be a near imperceptible difference in induced signals between tracks that are emitted at grazing angles and those emitted at steep angles down the chamber axis of symmetry, since the drift times and location relative to the anode segments would be nearly identical. A summary of the experiment parameters is given below in Table 7.1.1.

Table 7.1.1: Summary of experiment parameters used for testing SCI-CASTER 1.9.

Parameter	Experiment 1	Experiment 2	Experiment 3
Source	^{239}Pu, ^{241}Am, ^{244}Cm (1 kBq activity)	^{239}Pu, ^{241}Am, ^{244}Cm (1 kBq activity)	^{239}Pu, ^{241}Am, ^{244}Cm (1 kBq activity)
Gas / pressure	Argon / 1400 Torr	Argon / 1400 Torr	Argon / 1700 Torr
Frisch grid voltage	700 V	1000 V	700 V
Anode voltage	1000 V	1300 V	1000 V

Prior to the experiments, the SCI-CASTER test chamber was allowed to saturate in 1700 Torr argon for 3 days. The goal of doing this is to have argon fill any small gaps in the chamber, most notably the coaxial cable braids, thus reducing the atmospheric content of the chamber. The chamber was subsequently pumped down to vacuum and re-pressurized prior to the experiments taking place.

7.2. Interpretation of Experiment Data

All 3 experiments successfully produced waveform data at approximately 25,000 events per experiment. These waveforms were then fit using the waveform analyzer program described in Chapter 6. The parameters generated by the analyzer have been used to measure various features of the data, for example, the time of drift in the ionization and collection regions, or the amplitudes of the anode segment signals. Two examples of waveform data from two events with relevant features are shown in Figure 7.2.1. Both the amplitudes and timings are measured by extrapolating the linear fits from each drift region and locating their intersection point. This is done because depending on the polar angle of emission, waveform boundaries will have varying degrees of curvature that will impact the amplitudes and timings of the cubic fits. By contrast, extrapolations of the linear fits should not be affected by this.
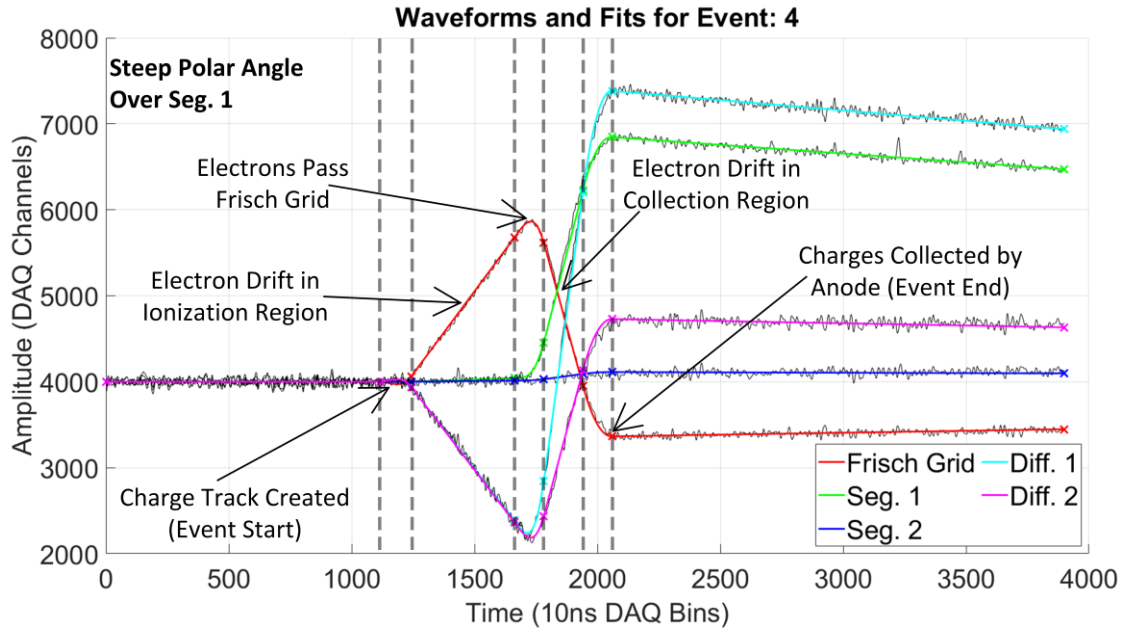
(a) Alpha track with steep polar angle directed over anode segment 1. Vertical dashed lines indicate the piecewise boundaries of the waveform fit.
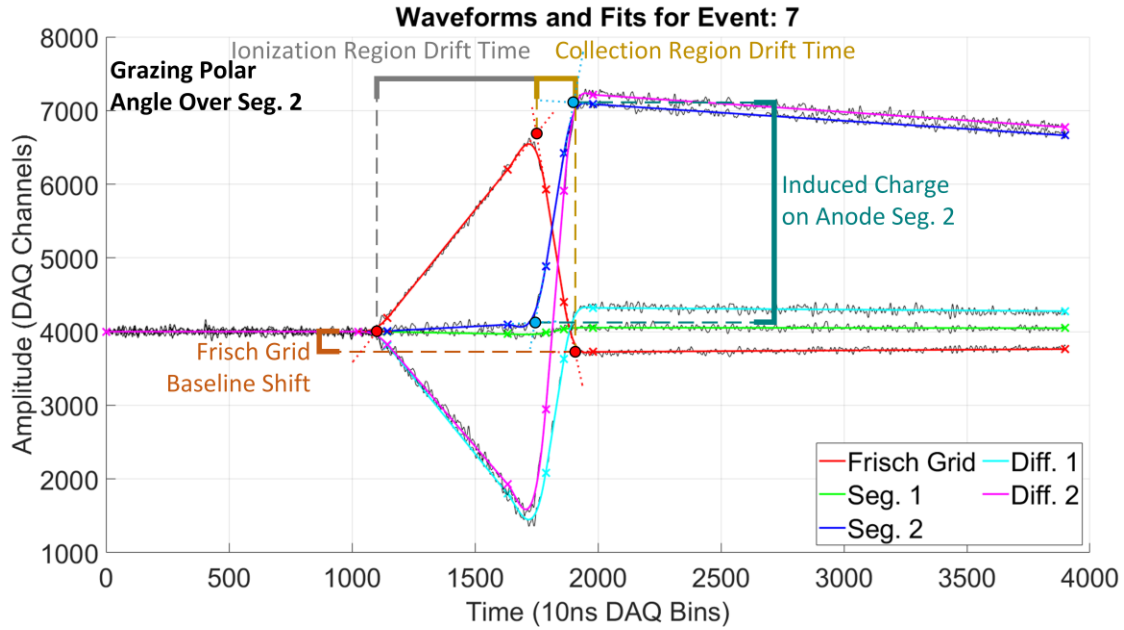
(b) Alpha track with grazing polar angle directed over anode segment 2. Relevant features extracted from fit parameters are shown.

Figure 7.2.1: Example waveforms from SCI-CASTER prototype 1.9 with overlaid fits and features of interest.

7.3. Results

Based upon the features shown in Figure 7.2.1(b), scatter plots of the relationships between induced charge and various other features have been created. These data are overlaid for all 3 experiments and reveal information about the fundamental behavior of the detector. The total induced charge on the anode is computed as the sum of the charge measured on anode segments 1 and 2 (the *summed segment amplitude*), where the anode segment 2 charge has been offset by +50 DAQ channels prior to the summation to account for a mismatch in the amplifier gains.

7.3.1. Charge as a Function of Frisch Grid Baseline Shift

Plotting the charge as a function of the shift in the Frisch grid baseline pre- and post-drift (Figure 7.3.1) reveals that at a minimum, 3 prominent alpha particle energies associated with the triple-alpha source are present, where these are mostly the 5156.59(14) keV peak from ^{239}Pu, the 5485.56(12) keV peak from ^{241}Am, and the 5804.77(5) keV peak from ^{244}Cm. Finer features such as the 5144.3(8) keV and 5105.5(8) keV peaks from ^{239}Pu, 5442.80(13) keV peak from ^{241}Am, and 5762.64(3) keV peak from ^{244}Cm appear to be lost in the main peaks, where this is explored further in Section 7.3.4. There also appears to be a non-linear relationship between the measured charge and the polar angle of emission as represented by the Frisch grid baseline shift. This is discussed further in Section 7.3.2.
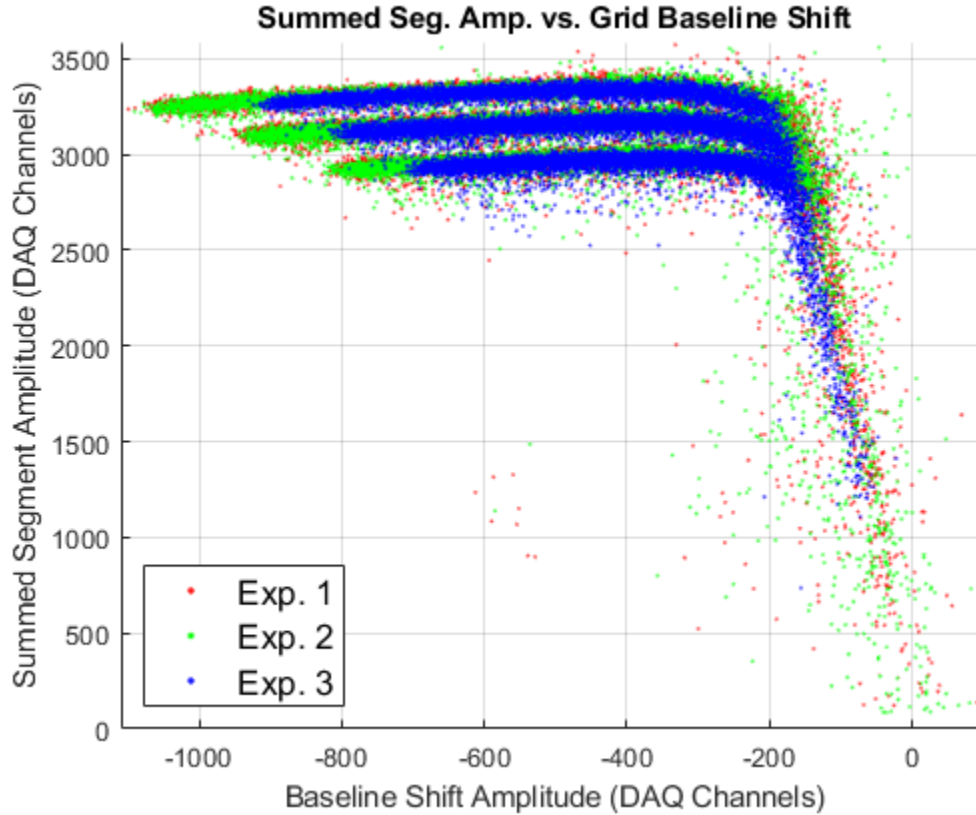
Figure 7.3.1: Summed anode segment charge as a function of the Frisch grid baseline shift.

A large polar angle of emission energy smear is also seen in Figure 7.3.1, where these events are associated with alpha particles that were emitted at grazing angles to the cathode. The energy smear is a result of the alpha particles losing their energy not only to a greater length of source material, but also due to interactions with the metal source disk and cathode plate. These interactions cause the alpha particles to lose only a fraction of their energy to the argon gas, thus resulting in a continuum of low-energy readings. The lack of positive Frisch grid baseline shifts demonstrates that for all 3 experiments, the field ratio was large enough that no appreciable amount of charge was lost to the Frisch grid. Additionally, the data from experiment 3 demonstrates the reduction in sensitivity to the polar angle of emission as a result of the increased pressure shortening the track lengths. This is indicated by the contracted distribution of data points along the horizontal axis.

7.3.2. Charge as a Function of Drift Times

The charge as a function of the collection region, ionization region, and total drift times is shown in Figure 7.32, Figure 7.3.3, and Figure 7.3.4, respectively.
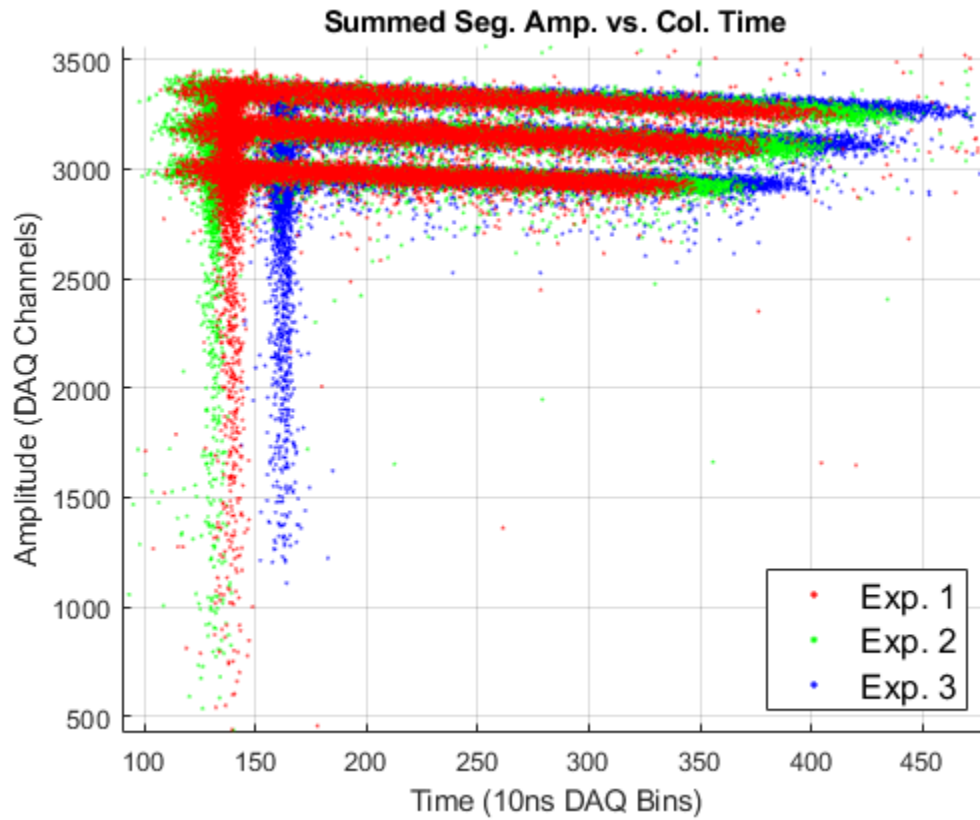
Figure 7.3.2: Summed anode segment charge as a function of collection region drift time.
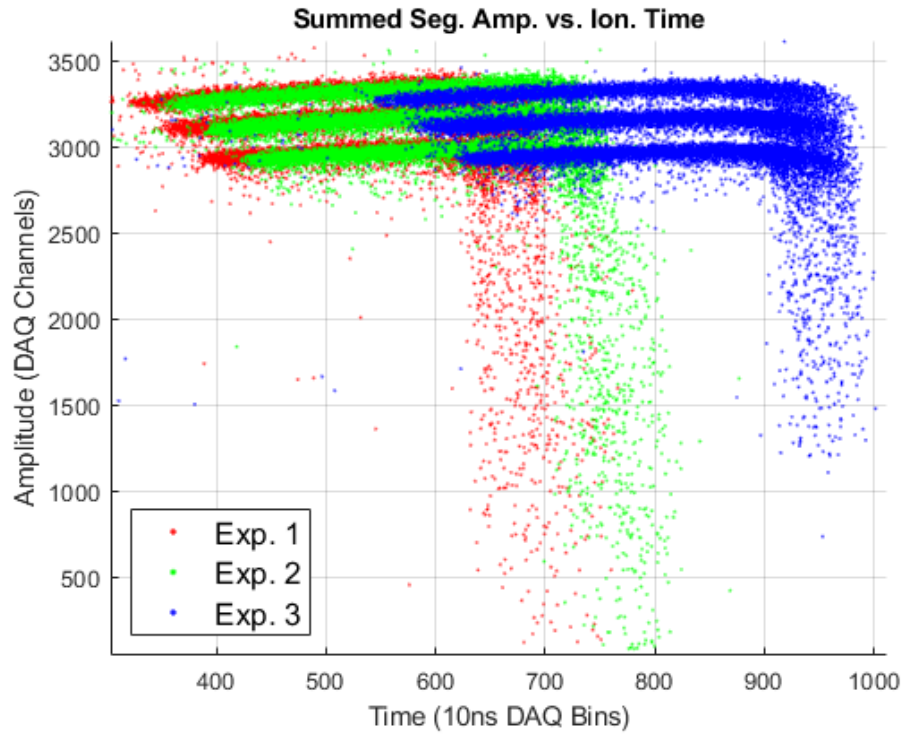
Figure 7.3.3: Summed anode segment charge as a function of ionization region drift time.
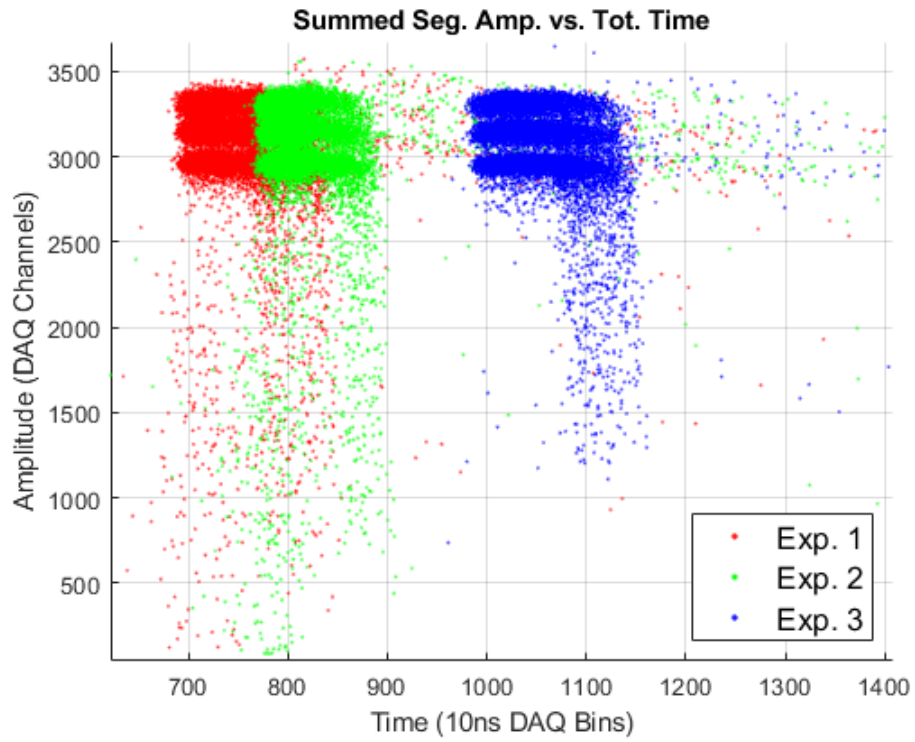
Figure 7.3.4: Summed anode segment charge as a function of total drift time.

Figure 7.3.2 indicates that there is a linear relationship between the collection region drift time and the measured charge, where this relationship does not appreciably change with bias voltage or gas pressure changes between experiments. It further appears that this relationship does not extend to the total time of drift, which indicates that as Figure 7.3.1 suggests, the relationship is dependent on the polar angle of emission and not the duration of time the charges spend in the detector volume.

Overall, the drift times measured in the 3 experiments are notably shorter than those expected based on published values for drift velocity as a function of the reduced field (V/cm/Torr), which suggest drift times that should be approximately twice as long as those seen here [33], [48]. Additionally, despite the increase in electric field in experiment 2 (which under pure argon should result in a shorter drift time), the time instead increased.

Both of these phenomena point to a contamination of the argon gas atmosphere in which the detector operates. It has been observed that that certain gas mixtures based on argon can have a peak in their drift velocities very near to the reduced field of this detector [33], [49], [50]. This would result in the drift velocity decreasing as the reduced field increases, thus explaining the observed behavior. This theory is further bolstered by plotting the charge as a function of the total drift time and Frisch grid baseline shift and color-coding chronological groups of 5000 events, thus creating a discretized time profile (Figure 7.3.5).

Figure 7.3.5 demonstrates that all 3 experiments experience a decrease in drift time, or increase in drift velocity, over time. This indicates that the gas contamination worsened as time progressed. The most likely cause of this is outgassing from the electronics and wiring present in the chamber, where these components have been noted to outgas small quantities of hydrogen, carbon dioxide, and methane [51], all of which can increase the drift velocity of electrons in argon gas. It is suspected that the initial pumping down of the chamber to vacuum purged the chamber of the contaminants being outgassed from the electronics. As the chamber was subsequently pressurized, the rate of outgassing of the components within the chamber was larger than the rate of gas exchange, thus leading to a time-dependent change in gas composition.
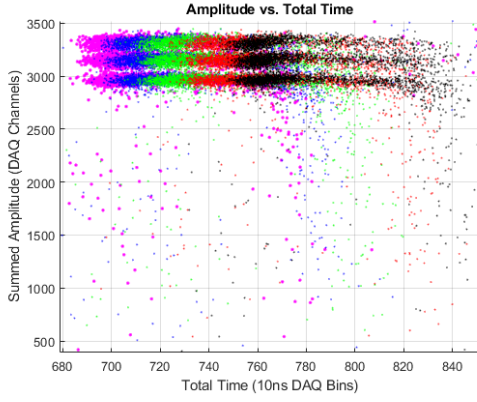
(a) Experiment 1 charge vs. total time   *(b) Experiment 1 charge vs. grid shift*
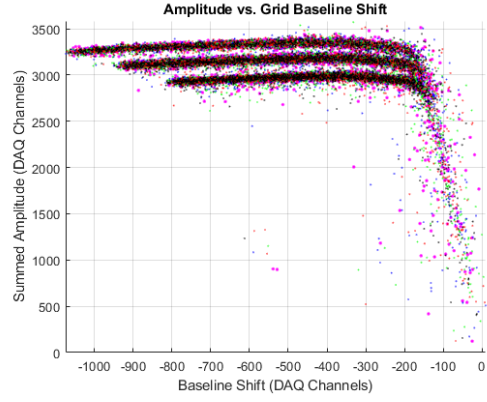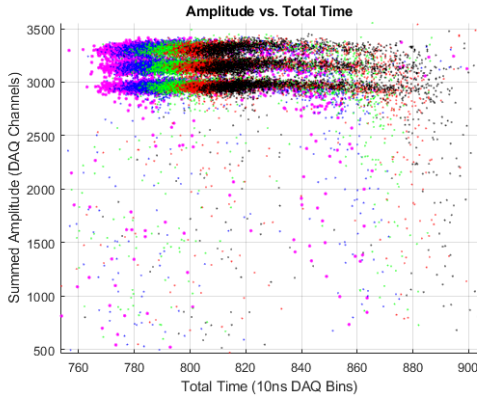
(c) Experiment 2 charge vs. total time   *(d) Experiment 2 charge vs. grid shift*
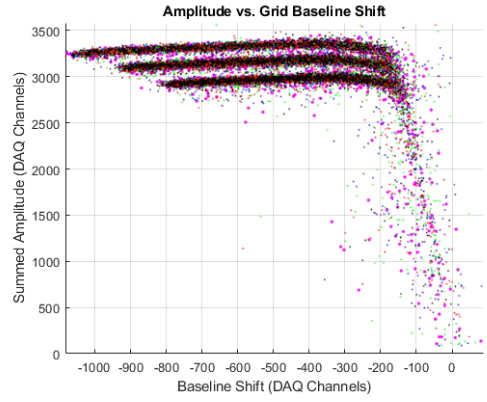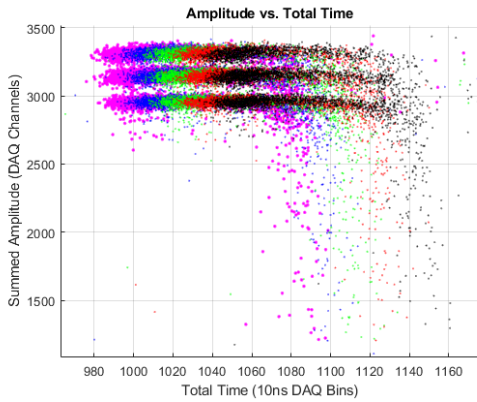
(e) Experiment 3 charge vs. total time   *(f) Experiment 3 charge vs. grid shift*
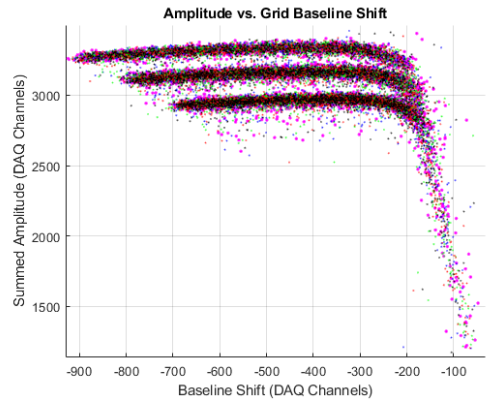
Figure 7.3.5: Charge as a function of total drift time and Frisch grid baseline shift. Plot colors correspond to groups of 5000 events, which are ordered chronologically as follows: black (experiment start), red, green, blue, magenta (experiment end).

Figure 7.3.5 also shows that the dependence of charge on the polar angle of emission does not change with time, indicating that either the contaminant gas has a relatively consistent impact on the charge as the polar angle varies, or an additional factor is causing this behavior.

The triple-alpha source being used with this detector, which has been noted to be stronger than the detector was designed to handle, may itself be the cause. Recalling that ions in a gas move ~1000 times slower than electrons, it is likely that at a nominal source activity of 3 kBq, or 1500 emissions per second considering the source geometry, there will be a buildup of ions in the ionization region of the detector. If an average angle of emission of 45° is considered, the time required for an ion track to reach the cathode based on electron drift times measured in the ionization region is ~5 ms. This means the detector will clear approximately 200 ion tracks per second, which is only a fraction of those being emitted per second. This buildup of ions has the potential to have two effects on detector operation:

1. It will cause a large cloud of ions to be persistently drifting towards the cathode at all times. While a single ion track may not have an appreciable effect on the readout of electron drift, several thousand ion tracks may have an effect.

2. There is a greater chance of charge recombination between electrons and the ions in the cloud. This would result in losing a varying percentage of electrons in each track, thus degrading energy resolution.

7.3.3. Anode Segment Charge Relationship

The most important result from the SCI-CASTER prototype 1.9 detector is the relationship between the charge read out from each anode segment, as this determines whether or not the detector is sensitive to the azimuthal angle of a track. The segment 2 vs. segment 1 charge relationship is shown in Figure 7.3.6, and clearly demonstrates the expected linear relationship between the charge induced on each segment. As in the summed amplitudes presented thus far, the three prominent alpha particle energies are visible in the plot. Splitting the data into 2 groups based on the dominant anode amplitude

revealed a near equal number of events in each group, therefore suggesting that the source material is centered in the detector.
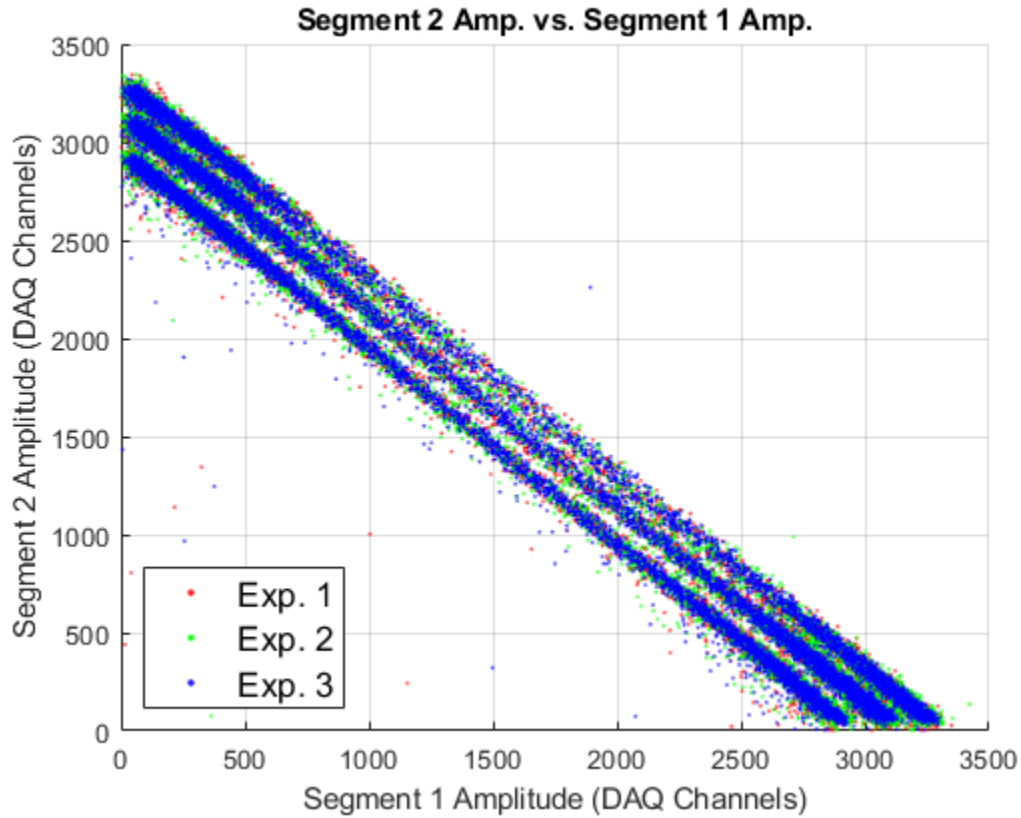
Figure 7.3.6: Anode segment 2 vs. segment 1 charge.

7.3.4. Energy Spectra

The final plot to be derived from the experiment data is the energy spectrum. To do this, the energy smear seen in Figures 7.3.1 – 7.3.4 is gated out of the data based on a collection time threshold. Further, the data is gated on the amplitudes and timings of the events to remove a fraction of erroneous values that result from unreported waveform fitting failures. Finally, a gate is set above the centroid of the χ^2 per degree of freedom for each experiment such that waveforms of poor fit quality are removed, leaving behind a clean summed segment charge scatter plot (Figure 7.3.7).
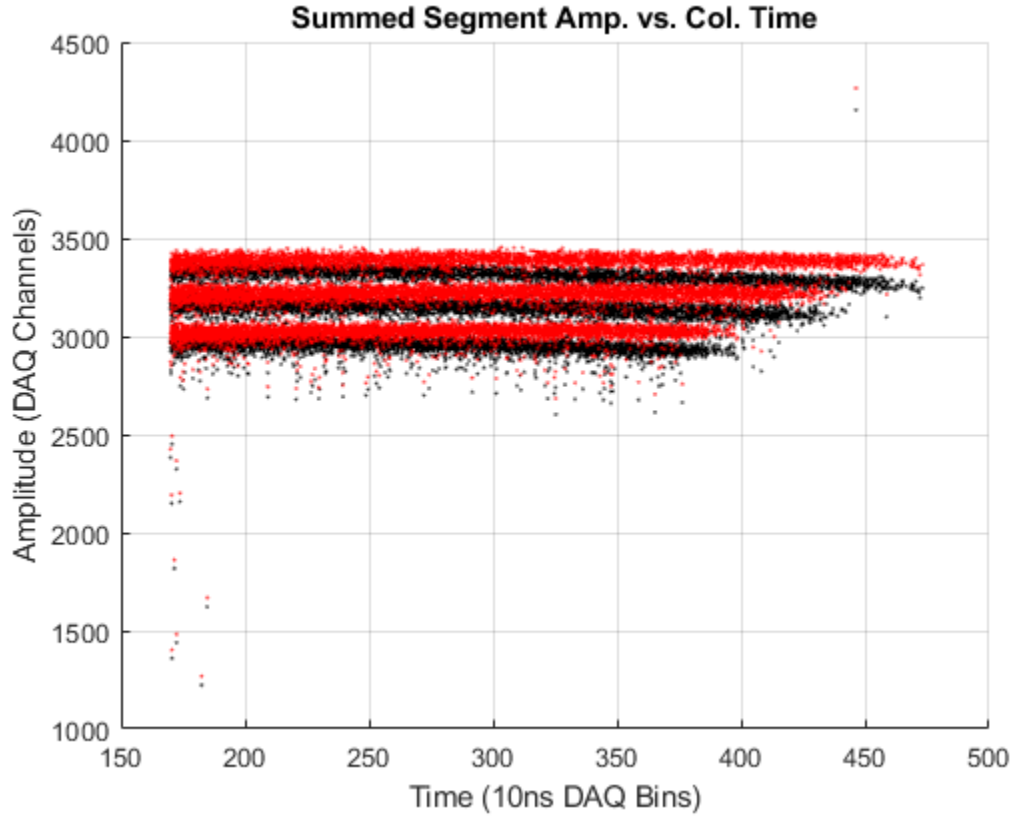
Figure 7.3.7: Summed segment charge as a function of collection time after event gating. The uncorrected data is shown in black, the corrected data is shown in red.

The final step is to de-correlate the charge from the polar angle by applying a 1st order correction to the charge based on the collection time. The coefficients for this correction are set manually for each experiment and produce a corrected scatter plot that is shown in red in Figure 7.3.7. Spectra of the corrected and gated charge readouts for each experiment are shown in Figure 7.3.8.
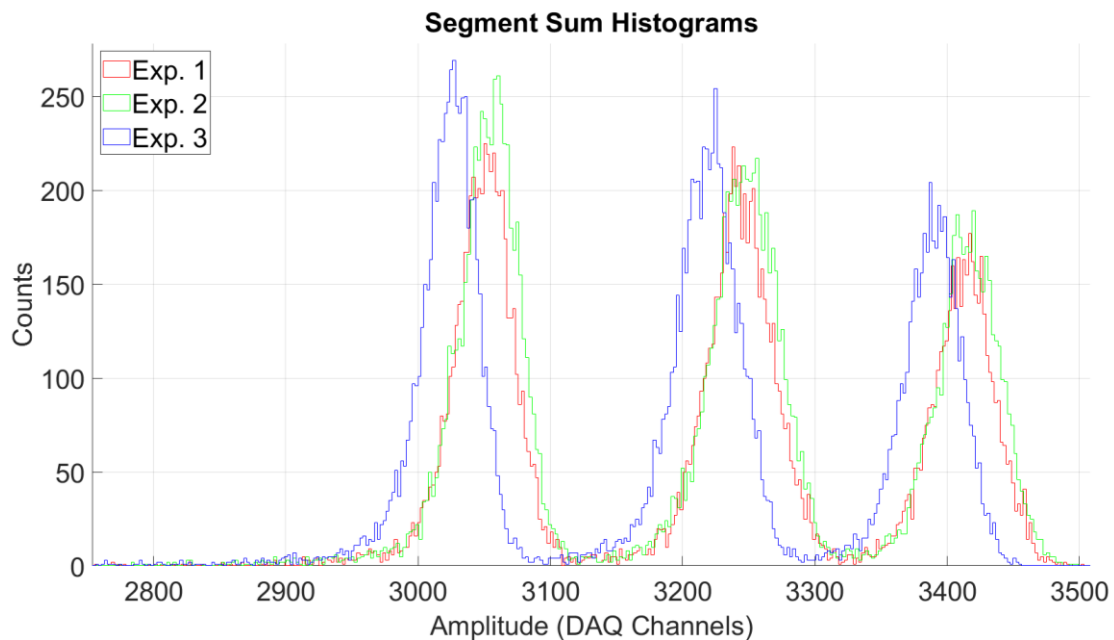
Figure 7.3.8: Gated and corrected charge spectra for each experiment. The shifts in amplitude are a result of the 1st order corrections applied to the data.

The above spectra are consistent with what has been observed in Section 7.3.1 in that the 3 peaks are dominated by the 3 prominent alpha particle energies. Finer features are lost and thus indicate a limitation of the detector resolution.

Chapter 8.   Conclusion and Future Developments

Significant progress has been made on the SCI-CASTER project in the SFU NSL, both in the form of a dedicated test setup for FGIC detectors and in the development of SCI-CASTER prototype 1.9.

The test setup located in the SFU NSL has proven to be able to handle up to 1750 Torr gas pressures after the main chamber was rebuilt and cleaned. The computer controlled gas and HV systems have demonstrated consistent behavior in the conducted experiments, and the addition of anti-vibration mounts to the chamber has improved its resilience to mechanical vibrations in the laboratory space. The TIGRESS DAQ used for the SCI-CASTER project has shown remarkable stability and has been able to reliably digitize waveforms at up to 1.1 mega-samples per second across 120 channels based on a single trigger signal input. The NIM logic trigger derivation and blocking loop has successfully limited the event rate of the DAQ such that previously observed instability has become a nonissue.

The physical design of SCI-CASTER prototype 1.9 has proven that conductor gaps between 0.25 mm and 0.5 mm are achievable for anode segmentation and that it is possible to utilize blind vias in the anode PCB to limit surface nonuniformities. Both of these factors contribute to maintaining a homogeneous electric field and charge collection surface. The electronic design, while functional enough to validate this prototype detector, is not sufficient for designs going forward. The instability of the amplifier circuitry necessitated the removal of the cathode amplifier channel, and various unexpected grounding techniques needed to be employed to reduce the noise to a usable level. Future work in this area will consist of a full redesign of the amplifier circuitry and the implementation of an in-house charge-to-voltage conversion stage. Additionally, the voltage regulation circuit will require an improved method of passive heat dissipation, as only the 8 channels used on this detector caused the regulators to warm up significantly.

The waveform analyzer program performed as expected and was able to yield high-quality piecewise fits of the waveform data produced by the detector. Future optimizations will include speed improvements to the algorithm where possible as well as parallelization to further increase waveform analysis throughput.

The observed relationship between measured charge and polar angle, the time-variation in total drift time, and the limitation of energy resolution are all areas that need to be characterized before additional SCI-CASTER detectors are built. This process will consist of moving all electronics to the exterior of the main chamber, thus significantly reducing the number of outgassing components in the detector atmosphere. Additionally, the triple-alpha source used in this work will be exchanged with a low-activity alpha source to better suit the detector's operating point.

The most important conclusion that can be drawn from this work is that SCI-CASTER prototype 1.9 effectively demonstrates that sensitivity to the azimuthal angle of emission of an ionizing particle can be achieved in an FGIC by segmenting the detector anode and using waveform analysis. Immediate future work will consist of using the data obtained thus far to determine the particle angles of emission and reconstruct the track of each particle in 3D space.

References

[1]   A. Hartmann, J. Hutsch, F. Kruger, M. Sobiella, H. Wilsenach and K. Zuber, "Design and performance of an ionisation chamber for the measurement of low alpha-activities," *Nuclear Instruments and Methods in Physics Research A,* vol. 814, pp. 12-18, 2016.

[2]   H. Wilsenach, K. Zuber, D. Degering, R. Heller and V. Neu, "High precision half-life measurement of 147Sm α decay from thin-film sources," *Physical Review C,* vol. 95, p. 034618, 2017.

[3]   C. Liu, D. Huo, X. Yang, Z. Ma, J. Zhou, C. Han, B. Xiaohou, K. Wu, Y. Zhang, J. Wang, Z. Yao and Z. Wei, "Development and testing of a Frisch-Grid Ionization Chamber for the measurement of low activity of alpha-particle emitters," *Journal of Radioanalytical and Nuclear Chemistry,* vol. 330, pp. 1091-1099, 2021.

[4]   G. Knoll, Radiation Detection and Measurement, 3rd ed., Wiley, 2000, p. 155.

[5]   C. Budtz-Jørgensen , H. Knitter, C. Straede, F. Hambsch and R. Vogt, "A Twin Ionization Chamber for Fission Fragment Detection," *Nucelar Instruments and Methods in Physics Research,* vol. 258, no. 2, pp. 209-220, 1987.

[6]   D. Mader, "An ionization chamber for fission fragment analysis," University of New Mexico, Albuquerque, 2013.

[7]   S. A. Bennett, P. T. MacGregor, A. G. Smith, R. L. Kennedy-Reid and T. Wright, "Development of a novel segmented anode Frisch-grid ionisation chamber for fission measurements," *Nuclear Instrumentation and Methods in Physics Research A,* vol. 951, 2020.

[8] L. I. Galanina, N. S. Zelenskaya, I. A. Konyukhova, V. M. Lebedev, N. V. Orlova and A. V. Spassky, "Investigation of the mechanism of inelastic alpha-particle scattering on 28Si nuclei by the method of angular αγ correlations at Eα = 30.3 MeV," *Physics of Atomic Nuclei,* vol. 73, no. 8, pp. 1339-1350, 2010.

[9] W. H. A. Hesselink and M. van Kampen, "Perturbations of alpha-gamma angular correlations in the decay of 230U and 226Th," *Z. Physik,* vol. 247, pp. 161-165, 1971.

[10] Z. Majka, D. G. Sarantites, L. G. Sobotka, K. Honkanen, E. L. Dines, L. A. Adler, L. Ze, M. L. Halbert, J. R. Beene, D. C. Hensley, R. P. Schmitt and G. Nebbia, "Nuclear Shapes from Alpha-Gamma-Ray Angular Correlations," *Physical Review Letters,* vol. 58, no. 4, pp. 322-325, 1987.

[11] C. Bosia, F. Chabaux, E. Pelt, A. Cogez, P. Stille, E. Deloule and C. France-Lanord, "U-series disequilibria in minerals from Gandak River sediments (Himalaya)," *Chemical Geology,* vol. 477, pp. 22-34, 2018.

[12] P. Guibert, C. Lahaye and F. Bechtel, "The importance of U-series disequilibrium of sediments in luminescence dating: A case study at the Roc de Marsal Cave (Dordogne, France)," *Radiation Measurements,* vol. 44, no. 3, pp. 223-231, 2009.

[13] M. Braun, Y. M. Georgiev, T. Schonherr and H. Wilsenach, "A new precision measurement of the α-decay half-lift of 190Pt," *Physics Letters B,* vol. 768, pp. 317-320, 2017.

[14] K. Kondo, I. Murata, K. Ochiai, N. Kubota, H. Miyamaru, C. Konno and T. Nishitani, "Measurement and Analysis of Neutron-Induced Alpha Particle Emission Double-Differential Cross Section of Carbon at 14.2 MeV," *Journal of Nuclear Science and Technology,* vol. 45, no. 2, pp. 103-115, 2008.

[15] J. Alme, Y. Andres, H. Appelshäuser, S. Bablok, N. Bialas, R. Bolgen, U. Bonnes, R. Bramm, P. Braun-Munzinger, R. Campagnolo, P. Christiansen, A. Dobrin, C. Engster, D. Fehlker, Y. Foka, U. Frankenfeld and J. Gaardhøje, "The ALICE TPC, a large 3-dimensional tracking device with fast readout for ultra-high multiplicity events," *Nuclear instruments & methods in physics research A,* vol. 622, no. 1, pp. 316-367, 2010.

[16] N. M. Viaux, "The ATLAS 'New Small Wheel' Muon detector stations recently commissioned for LHC Run3," *Nuclear instruments & methods in physics research A,* vol. 1045, no. 167574, 2023.

[17] M. Li, Y. Yang, P. Ma, J. Zhang, Z. Qin, X. Wei, C. Xiao, T. Qiu, Z. He, C. Lu, R. Hu, H. Yang, Y. Fang, Z. Xiao, H. Wang, H. Yikai, L. Duan and H. J. Ong, "Exploration of grid scheme for Frisch-grid ionization chamber," *The European Physical Journal C,* vol. 81, no. 12, p. 1089, 2021.

[18] Ortec Ametek, "B Series Totally Depleted Silicon Surface Barrier Radiation Detector," 2021. [Online]. Available: https://www.ortec-online.com/-/media/ametekortec/brochures/b/b-series.pdf?la=en&revision=50e7aca1-fd0b-4830-8a2c-c2fc7d9a2913. [Accessed 06 November 2023].

[19] J. Williams, C. Andreoiu, G. C. Ball, N. Bernier, M. Bowry, S. S. Bhattacharjee, C. Burbadge, R. Caballero-Folch, A. Chester, F. H. Garcia, A. B. Garnsworthy, S. A. Gillespie, G. Hackman, R. Henderson, B. Jigmeddorj, C. Jones, P. Kowalski, R. Lafleur, A. D. MacLean, M. Morrison, B. Olaizola, Y. Saito, L. Sexton, P. Šiuryte, J. Smallcombe, K. Starosta, C. E. Svensson, M. Spencer, E. Timakova, K. Van Wieren, P. Voss, M. Winokan and F. Wu, "The CsI ball ancillary detector array for TIP and TIGRESS at TRIUMF," *Nuclear Instrumentation and Methods in Physics Research A,* vol. 939, pp. 1-9, 2019.

[20] M. d. C. C. Pereira, T. M. Filho, V. M. Lopes, J. R. Berretta and J. P. N. Cárdenas, "Scintillation response of CsI: Tl crystal under neutron, gamma, alpha particles and beta excitations," in *INAC 2015: International Nuclear Atlantic Conference*, Sao Paulo, 2015.

[21] J. Williams, "Study of 28Mg and 22Ne using fusion-evaporation and Doppler shift techniques," Simon Fraser University, Burnaby, 2019.

[22] A. B. Garnsworthy and P. E. Garrett, "The 8π Spectrometer," *Hyperfine Interactions,* vol. 225, pp. 121-125, 2014.

[23] J. Williams, A. Chester, T. Domingo, U. Rizwan, K. Starosta and P. Voss, "NEUTRON GENERATOR FACILITY AT SFU: GEANT4 DOSE RATE PREDICTION AND VERIFICATION," *Radiation Protection Dosimetry,* vol. 171, no. 3, pp. 313-325, 2016.

[24] J. Williams, "Development of a Neutron Generator Facility at Simon Fraser University," Simon Fraser University, Burnaby, 2015.

[25] J. F. Ziegler, "INTERACTIONS OF IONS WITH MATTER," [Online]. Available: http://www.srim.org/. [Accessed February 2022].

[26] W. Shockley, "Currents to Conductors Induced by a Moving Point Charge," *Journal of Applied Physics,* vol. 9, no. 10, pp. 635-636, 1938.

[27] Z. He, "Review of the Shockley–Ramo theorem and its application in semiconductor gamma-ray detectors," *Nuclear Instruments and Methods in Physics Research A,* vol. 463, pp. 250-267, 2001.

[28] A. Redey, "Preliminary Design and Verification of a Low Rate Ionization Chamber for the 8Pi Gamma Ray Spectrometer: SCI-CASTER," Burnaby, 2021.

[29] R. Ashley, "Characterization of the First Stage Prototype of the TIFFIN Detector," 2014.

[30] O. Bunemann, T. Cranshaw and J. Harvey, "Design of Grid Ionization Chambers," *Canadian Journal of Research,* vol. 27a, no. 5, pp. 191-206, 1949.

[31] M. Kase, T. Akioka, H. Mamyoda, J. Kikuchi and T. Doke, "Fano Factor in Pure Argon," *Nuclear Instruments and Methods in Physics Research,* vol. 227, no. 2, pp. 311-317, 1984.

[32] A. Deisting, C. Garabatos, A. Szabo and D. Vranic, "Measurements of Ion Mobility in Argon- and Neon-Based Gas Mixtures," in *CERN RD51 Collaboration Meeting*, CERN Geneva, 2016.

[33] I.-B. G. Ferreira, J. G. Herrera and L. Villaseñor, "The Drift Chambers Handbook, introductory laboratory course (based on, and adapted from, A H Walenta's course notes)," *Journal of Physics: Conference Series,* vol. 18, pp. 346-361, 2005.

[34] CERN, "Garfield++," CERN, [Online]. Available: https://garfieldpp.web.cern.ch/garfieldpp/. [Accessed February 2022].

[35] MKS Instruments, "πPC PC99 Integrated Downstream Pressure Controller with Mass Flow Meter," 2021. [Online]. Available: https://www.mksinst.com/f/pc99-integrated-pressure-controller. [Accessed 20 February 2021].

[36] MKS Instruments, "M100B/M10MB Economical, Range Adjustable Mass-Flo Controller/Meter," MKS Instruments, Andover, MA, 2006.

[37] MKS Instruments, "722B 1-25,000 Torr, General Purpose Absolute Baratron® Capacitance Manometer," [Online]. Available: https://www.mks.com/f/722b-compact-absolute-capacitance-manometers. [Accessed 20 February 2021].

[38] CCR Process Products, "CCR Model 400 4-Channel MFC Power Supply/Controller Manual," CCR Process Products, Kanata, Ontario, 2008.

[39] iseg, "NHQ High Precision Single/Dual Channel HV Module in NIM Standard," [Online]. Available: https://iseg-hv.com/en/products/detail/NHQ. [Accessed 19 January 2021].

[40] J. P. Martin, C. Mercier, N. Starinski, C. J. Pearson and P. A. Amaudruz, "The TIGRESS DAQ/Trigger System," *IEEE Transactions on Nuclear Science,* vol. 55, no. 1, pp. 84-90, 2008.

[41] TRIUMF and PSI, "MIDAS - Main Page," 13 September 2023. [Online]. Available: https://daq00.triumf.ca/MidasWiki/index.php/Main_Page. [Accessed 13 October 2023].

[42] Cremat Inc, "CR-110-R2 charge sensitive preamplifier: application guide," October 2018. [Online]. Available: https://www.cremat.com/CR-110-R2.pdf. [Accessed 25 September 2020].

[43] Analog Devices, "AD8421 Data Sheet," 2020. [Online]. Available: https://www.analog.com/media/en/technical-documentation/data-sheets/ad8421.pdf. [Accessed 28 November 2022].

[44] Analog Devices / Linear Technology, "LT3015 Series," 2011. [Online]. Available: https://www.analog.com/media/en/technical-documentation/data-sheets/3015fb.pdf. [Accessed 30 November 2022].

[45] Analog Devices / Linear Technology, "LT1963A Series," 2005. [Online]. Available: https://www.analog.com/media/en/technical-documentation/data-sheets/1963aff.pdf. [Accessed 30 November 2022].

[46] Eckert & Ziegler, "Alpha Spectroscopy Sources," Eckert & Ziegler, [Online]. Available: https://www.ezag.com/home/products/isotope_products/isotrak_calibration_sources/reference_sources/alpha_spectroscopy_sources/. [Accessed 1 August 2023].

[47] National Institute of Standards and Technology: Physical Meas. Laboratory, "ASTAR Stopping-Power and Range Tables for Helium Ions," July 2017. [Online]. Available: https://physics.nist.gov/PhysRefData/Star/Text/ASTAR.html. [Accessed 4 February 2021].

[48] J. M. Kirshner and D. S. Toffolo, "Drift Velocity of Electrons in Argon and Argon Mixtures," *Journal of Applied Physics,* vol. 23, pp. 594-598, 1952.

[49] D. A. Wijngaarden, "Electron drift velo cities in fast Argon and CF4 based drift gases," CERN, 1998.

[50] K. D. Ianakiev, M. T. Swinhoe, K. Chung and E. A. McKigney, "Large Area Neutron Detector Based on 6Li Ionization Chamber with Integrated Body-Moderator of High Density Polyethylene," *IEEE Symposium Conference Record Nuclear Science,* vol. 1, pp. 456-460, 2004.

[51] Rouki, C; Westerberg, L; CHICSi development group, "Ultra-High Vacuum Compatibility Measurements of Materials for the CHICSi Detector System," *Physica Scripta,* vol. T104, pp. 107-108, 2003.

[52] J. Coderre, "MIT Open Courseware: Principles of Radiation Interactions," 2004. [Online]. Available: https://ocw.mit.edu/courses/22-55j-principles-of-radiation-interactions-fall-2004/resources/energy_depos_hcp/. [Accessed 10 October 2020].

[53] jmsaavedra, "Custom PCB Prototyping Using a Laser Cutter," 2010. [Online]. Available: https://www.instructables.com/Custom-PCB-Prototyping-using-a-Laser-Cutter/. [Accessed 20 October 2020].

Appendix A.   Maximum Energy Transfer

Beginning with the conservation of energy and momentum, two equations for the elastic collision between an alpha particle and an electron can be written:

$$\frac{1}{2}m_\alpha v_{\alpha 1}^2 + \frac{1}{2}m_e v_{e1}^2 = \frac{1}{2}m_\alpha v_{\alpha 2}^2 + \frac{1}{2}m_e v_{e2}^2, \tag{A.1}$$

$$m_\alpha v_{\alpha 1} + m_e v_{e1} = m_\alpha v_{\alpha 2} + m_e v_{e2}, \tag{A.2}$$

where m_α and m_e are the masses of an alpha particle (4 amu) and an electron (0.000548 amu), and v_{x1} and v_{x2} are the particle velocities pre- and post-collision.

Under the assumption that the alpha particle is moving much faster than the electron, the collision is head-on, and that the energy transferred in the collision is much larger than the binding energy of the electron [52], Equation A.1 and A.2 are simplified to

$$\frac{1}{2}m_\alpha v_{\alpha 1}^2 = \frac{1}{2}m_\alpha v_{\alpha 2}^2 + \frac{1}{2}m_e v_{e2}^2, \tag{A.3}$$

$$m_\alpha v_{\alpha 1} = m_\alpha v_{\alpha 2} + m_e v_{e2}. \tag{A.4}$$

Solving for $v_{\alpha 2}$ in Equation A.4 yields

$$v_{\alpha 2} = \frac{m_\alpha v_{\alpha 1} - m_e v_{e2}}{m_\alpha}, \tag{A.5}$$

which can then be substituted into Equation A.3, where solving for v_{e2} yields

$$v_{e2} = 2\frac{m_\alpha}{m_\alpha + m_e}v_{\alpha 1}. \tag{A.6}$$

As a final step, the kinetic energy transferred to the electron from the collision is found by squaring Equation A.6 and multiplying both sides by $\frac{1}{2}m_e$:

$$\frac{1}{2}m_e v_{e2}^2 = \left[\frac{4m_\alpha m_e}{(m_\alpha + m_e)^2}\right]\left[\frac{1}{2}m_\alpha v_{\alpha 1}^2\right], \tag{A.7}$$

where the maximum fraction of kinetic energy transferred from the alpha particle $(E_{\alpha 1})$ to the electron (E_{e2}) is

$$\frac{E_{e2}}{E_{\alpha 1}} = \frac{4m_\alpha m_e}{(m_\alpha + m_e)^2} = 5.48223 \times 10^{-4}. \tag{A.8}$$

Appendix B.   Derivation of the Shockley-Ramo Theorem

The following derivation is based on the work done in [26] and [27]. To begin, consider the work w done by an electric field $\vec{E}$ in moving the point charge q from an arbitrary point a to an arbitrary point b along a path $\vec{s}$, where the work done per unit charge is the EMF ε and is formally defined as the line integral

$$\varepsilon = \int_a^b \vec{E} \cdot d\vec{s}, \qquad (B.1)$$

and therefore the work w is

$$w = q \int_a^b \vec{E} \cdot d\vec{s}. \qquad (B.2)$$

Now, consider the energy density j of the electric field of a volume, which is defined as

$$\begin{aligned} j &= \frac{1}{2} \varepsilon \vec{E}^2 \\ &= \frac{1}{2} \vec{E} \cdot \vec{D}, \end{aligned} \qquad (B.3)$$

where $\vec{D}$ is the electric displacement field. From Equation B.3, it can be said that over a volume R (where R is used instead of V, since V will represent the electric potential of conductors in the volume R) the total energy of the electric field is

$$U_{tot} = \frac{1}{2} \varepsilon \int_R \left| \vec{E} \right|^2 dR. \qquad (B.4)$$

To find the change in total energy of the electric field due to the movement of point charge q from a to b, a general statement can be written:

$$dU = \frac{1}{2} \varepsilon \int_R \left(\left| \vec{E}_b \right|^2 - \left| \vec{E}_a \right|^2 \right) dR, \qquad (B.5)$$

83

and since work is defined as a change in energy, Equations B.2 and B.5 yield

$$q \int_a^b \vec{E} \cdot d\vec{s} = \frac{-1}{2} \varepsilon \int_R \left(\left| \vec{E}_b \right|^2 - \left| \vec{E}_a \right|^2 \right) dR. \qquad (B.6)$$

Now, suppose that in the volume R there is an arbitrary set of conductors under two separate conditions:

Condition 1: All conductors are grounded, but a static space charge $\rho(\vec{r})$ and a moving particle with a charge q are present.

Condition 2: All conductors are held at their respective potentials, but there are no charges whatsoever in the volume.

Given the above conditions, two assumptions must now be made:

Assumption 1: The electric field $\vec{E}$ is in actuality the linear superposition of the electric fields in conditions 1 and 2:

$$\vec{E} = \vec{E}_1 + \vec{E}_2. \qquad (B.7)$$

Assumption 2: The electric fields for each conductor i are enforced by HV power supplies (PSUs) which themselves supply energy to the field:

$$w_{PSU} = \sum_{i=1}^{k} V_i \Delta Q_i, \qquad (B.8)$$

where V_i is the potential of conductor i and ΔQ_i is the induced charge on conductor i. Under these assumptions, Equation B.6 becomes

$$\sum_{i=1}^{k} V_i \Delta Q_i - q \int_a^b (\vec{E}_1 + \vec{E}_2) \cdot d\vec{s} = \frac{1}{2} \varepsilon \int_R \left(\left| \vec{E}_{1,b} + \vec{E}_2 \right|^2 - \left| \vec{E}_{1,a} + \vec{E}_2 \right|^2 \right) dR, \qquad (B.9)$$

which states that the work done on the moving point charge q by the HV power supplies minus the energy absorbed by q itself is equal to the total energy deposited into the electric field.

It is now necessary to apply Green's 1st identity, which states that for arbitrary scalar functions f and g and for the volume R and surface T:

$$\int_R (f\Delta g + \nabla f \cdot \nabla g)dR = \oint_T f\nabla g \cdot d\vec{T}, \tag{B.10}$$

where ∇ is the gradient operator and Δ is the Laplace operator. Green's 1st identity can be rewritten in terms of the scalar electric potentials φ_1 and φ_2 in conditions 1 and 2 as follows:

$$\int_R (\varphi_1\Delta\varphi_2 + \nabla\varphi_1 \cdot \nabla\varphi_2)dR = \oint_T \varphi_1\nabla\varphi_2 \cdot d\vec{T}. \tag{B.11}$$

If φ is an electrostatic potential associated with a charge distribution $\rho(\vec{r})$ then

$$\rho(\vec{r}) = -\varepsilon_0\Delta\varphi, \tag{B.12}$$

and since condition 1 has all conductors at ground potential,

$$\varphi_1 = 0, \tag{B.13}$$

and condition 2 by definition has no charge distribution,

$$\varepsilon_0\Delta\varphi_2 = 0. \tag{B.14}$$

Furthermore, under the assumption that the electric fields are static,

$$\vec{E} = -\nabla\varphi, \tag{B.15}$$

which means

$$\int_R (\vec{E}_1 \cdot \vec{E}_2)dR = \int_R (\nabla\varphi_1 \cdot \nabla\varphi_2)dR. \tag{B.16}$$

Under the conditions of Equations B.13, B.14, and B.16, Equation B.11 is reduced to:

$$\int_R \left(\vec{E}_1 \cdot \vec{E}_2 \right) dR = 0, \tag{B.17}$$

and from this the right-hand side of Equation B.9 can be expanded to:

$$\frac{1}{2}\varepsilon \int_R \left(\left| \vec{E}_{1,b} \right|^2 + 2\left(\vec{E}_{1,b} \cdot \vec{E}_2 \right) + \left| \vec{E}_2 \right|^2 - \left| \vec{E}_{1,a} \right|^2 - 2\left(\vec{E}_{1,a} \cdot \vec{E}_2 \right) - \left| \vec{E}_2 \right|^2 \right) dR, \tag{B.18}$$

where by Equation B.17 the 2nd and 5th terms are zero, making Equation B.9:

$$\sum_{i=1}^{k} V_i \Delta Q_i - q \int_a^b \left(\vec{E}_1 + \vec{E}_2 \right) \cdot d\vec{s} = \frac{1}{2}\varepsilon \int_R \left(\left| \vec{E}_{1,b} \right|^2 - \left| \vec{E}_{1,a} \right|^2 \right) dR. \tag{B.19}$$

Equation B.19 states that the change in field energy is reflective of only the drift of charge in the volume R, that is, condition 1. Therefore, the fixed electric potentials of the conductors do not change the field energy. Expanding the left-hand side of Equation B.19 and substituting the right-hand side from Equation B.6 yields

$$\sum_{i=1}^{k} V_i \Delta Q_i - q \int_a^b \vec{E}_1 \cdot d\vec{s} - q \int_a^b \vec{E}_2 \cdot d\vec{s} = -q \int_a^b \vec{E}_1 \cdot d\vec{s}, \tag{B.20}$$

which simplifies to

$$\sum_{i=1}^{k} V_i \Delta Q_i = q \int_a^b \vec{E}_2 \cdot d\vec{s}. \tag{B.21}$$

The electric potential at an arbitrary point in a static electric field $\vec{E}$ is given by the line integral

$$\varphi = - \int_C \vec{E} \cdot d\vec{s}, \tag{B.22}$$

where C is a path between two points in the field. This can be used to rewrite the right-hand side of Equation B.21 as follows:

$$\sum_{i=1}^{k} V_i \Delta Q_i = -q(\varphi_{2,b} - \varphi_{2,a}). \qquad (B.23)$$

At this point, a set of three conditions must be imposed to find the time-dependent induced current and charge on a single conductor:

1) Set the potential on a single conductor of interest to 1.0 V, call this conductor 1.

2) All other conductors are set to 0 V potential.

3) Consider only the case were all charge distributions in the volume R are ignored, where this is already implicitly done in Equation B.23.

Under the above conditions, Equation B.23 becomes

$$(1.0 \text{ V})\Delta Q_1 = q \int_a^b \vec{E}_2 \cdot d\vec{s} \qquad (B.24)$$
$$= -q(\varphi_{2,b} - \varphi_{2,a}),$$

where dividing both sides by 1.0 V results in the Ramo weighting potentials $\varphi_{2,bR}$ and $\varphi_{2,aR}$ and the Ramo weighting field $\vec{E}_{2R}$:

$$\Delta Q_1 = q \int_a^b \vec{E}_{2R} \cdot d\vec{s} \qquad (B.25)$$
$$= -q(\varphi_{2,bR} - \varphi_{2,aR}),$$

From B.25 and the knowledge that current is defined as the derivative of charge with respect to time, the time-dependent induced charge $Q(t)$ and current $i(t)$ for a single conductor due to the movement of a particle with charge q are:

$$Q(t) = -q\varphi_{2R}(\vec{s}(t)), \qquad (B.26)$$

$$i(t) = q\vec{E}_{2R}(\vec{s}(t)) \cdot \vec{v}(t), \qquad (B.27)$$

where $\vec{v}$ is the constant velocity of the particle, thus completing the derivation of the Shockley-Ramo theorem.

Appendix C.   Anode Production

Segmented detector design requires that multiple conductive electrodes are as close as possible to each other on the anode plane while not being in electrical contact, where the former is done to ensure minimal perturbation of the detector electric field. In addition to these requirements, each electrode must be connected to HV and amplifier circuitry. This can become complicated when electrodes are isolated from the edge of the anode, requiring cable connections to be made from the back of each segment. While the prototype 1.9 detector does not have this complication, subsequent SCI-CASTER detectors will and it was therefore decided to develop a manufacturing process that can be used in future designs.

A PCB-based design was chosen as the most likely candidate, as it can be precisely machined on both a waterjet cutter and a laser cutter and can be chemically etched to create small features. An important consideration is that CO_2 lasers tend to reflect off copper surfaces rather than cut them whereas the FR4 material used in PCBs is readily burned by the laser, albeit with a poor finish. This makes a CO_2 laser a reasonable choice both for precise laser drilling and laser etching of a mask on the PCB copper surface. To test the minimum feature size of the segment gaps and the feasibility of laser drilling blind vias into the PCB, two test boards were made.

The first board used wide spacings of 3.0 mm and 0.5 mm to test the etching capability of the laser cutter being used (Kern 400 Watt HSE CO_2 laser), and a variety of hole sizes for the blind vias to determine the minimum diameter (Figure C.1). The laser etching process generally consists of covering the copper face of the PCB with 4-5 layers of black spray paint and subsequently making 4-5 raster-scan engraving passes using the laser cutter, effectively creating a mask for the copper chemical etching process. Multiple passes are required to fully remove the spray paint layer as some of the paint will re-adhere to the copper surface after removal [53].
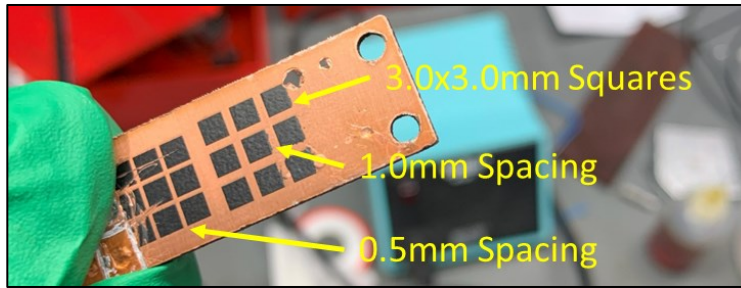
*(a) Laser used to etch away all paint except over an array of square segments.*
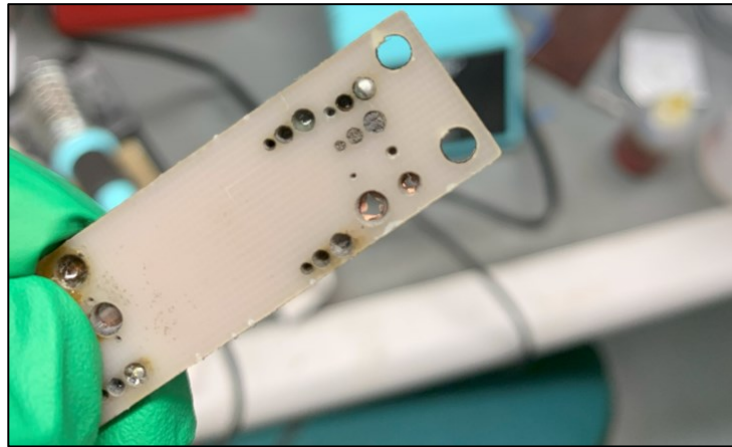
(b) Laser drilled blind vias at varying power levels and diameters.

Figure C.1: First board made for testing laser processing of PCBs.

The removal of paint using laser etching is shown in Figure C.1(a) and demonstrated that good results could be achieved for the chosen wide spacings. Laser drilling tests done in Figure C.1(b) yielded a minimum programmed hole diameter of approximately 2.0 mm, where this was limited by the tapered structure of the hole due to divergence of the laser beam between its focal point at the top surface of the PCB and the defocused beam at the back of the copper cladding.

The second board used finer spacings of 0.25 mm and 0.1 mm to further test the laser etching resolution, and an attempt was made to laser drill a matching array of 2.0 mm diameter blind vias behind the array of square segments. The exposed copper was subsequently chemically etched using ferric chloride to create an array of copper segments, where different stages of the process are shown in Figure C.2.
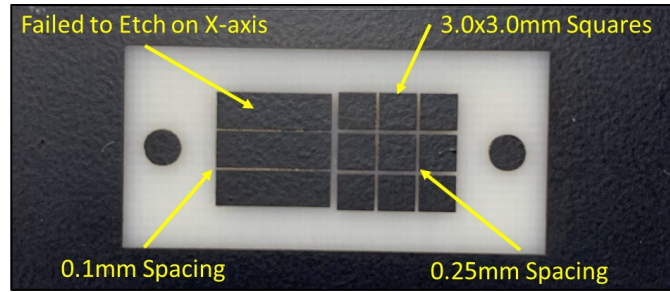
(a) Masked and chemically etched test patterns.

(b) Laser drilled blind vias behind test patterns.
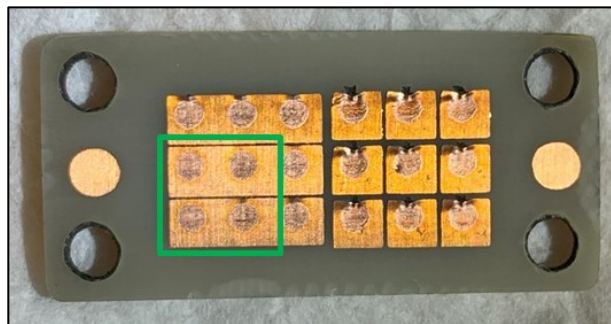
(c) Front of second test board after removal of the paint mask. The squares in the green box had good alignment with the blind vias and demonstrated minimal surface disruption, albeit with discoloration present.

Figure C.2: Second test board at various stages of processing.

Figure C.2(a) shows that there are different limits to the laser cutter's etching resolution, where the visible limitation likely comes from the beam needing to pulse as the laser head scans the board. As a result, 0.25 mm has been considered to be the reasonably attainable minimum separation between segments. Figure C.2(b) clearly shows the back of the copper cladding of the PCB, as well as the poor finish attained when laser cutting FR4.

While the laser drilled blind vias were not in perfect alignment with the test pattern of squares (Figure C.2(c)), the ones that did align showed minimal disruption to the copper surface other than some discoloration.

As a final step, different methods of connecting cables to the segments through the blind vias were tested using the second board (Figure C.3). These methods included various types of soldering and a conductive epoxy; the results of the tests are given below:

Leaded solder and soldering iron: Would not bond to copper, soldering iron marred the segment faces.

Low-temperature solder and hot plate: Successfully bonded to copper, good conductivity and strength.

Low-temperature solder with flux and hot plate: Would not bond to copper, flux caused solder to float in the via and fall out after cooling.

Conductive epoxy: Successfully bonded to copper, however resistance measured in the kΩ range.
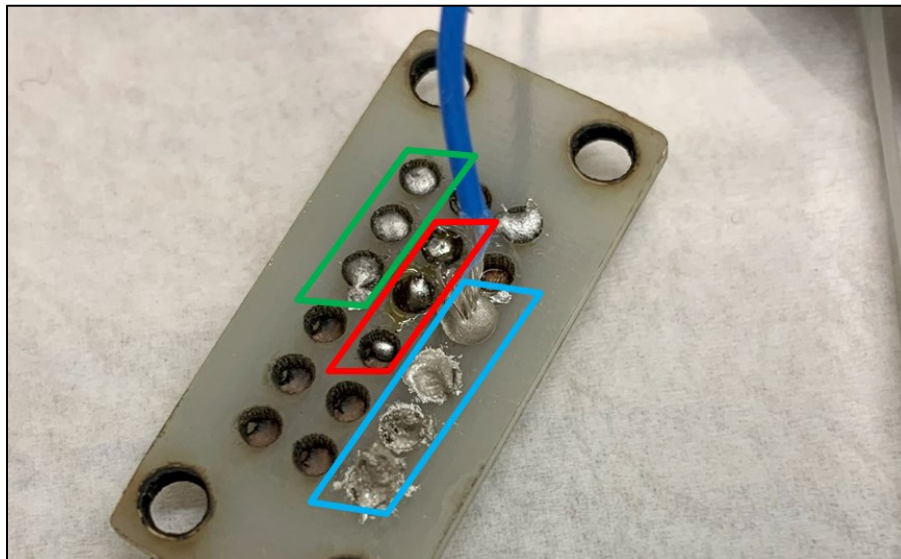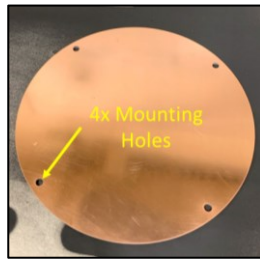

Figure C.3: Testing attaching cable to copper segments. Methods included: leaded solder and soldering iron (not shown), low-temperature solder and hot plate (green), low-temperature solder with flux and hot plate (red), and conductive epoxy (blue).

It was found that the use of a hot plate with low-temperature solder gave the most consistent results with no significant resistance measured between the copper face and the cable end, and this method was therefore used in the production of the prototype 1.9 segmented anode.
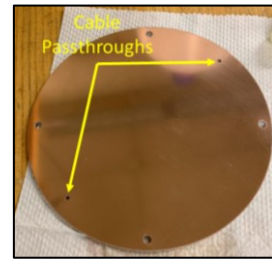
The process of creating the anode plates began by machining all cut-through features on the PCBs on a waterjet cutter, since CO_2 lasers, as discussed previously, leave a poor surface finish on FR4 and tend to reflect off copper. Images of the waterjet bed and the finished PCB components are shown in Figure C.4.
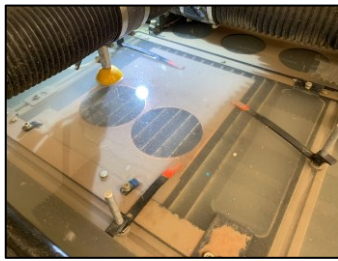
*(a) Waterjet cutter bed with remaining material.* *(b) Cut anode PCB.* *(c) Cut grounding plate PCB.*

Figure C.4: Waterjet processing of the anode PCBs.

Following this, the anode PCB was coated in 5 layers of black spray paint and loaded into the CO_2 laser cutter, where a 0.25 mm wide line was etched in the paint mask. A paper mounting frame was used to align the anode PCB in the laser cutter and keep its position consistent between manufacturing steps. Images of this process are shown in Figure C.5.

(a) Cut paper frame to mount anode PCB.
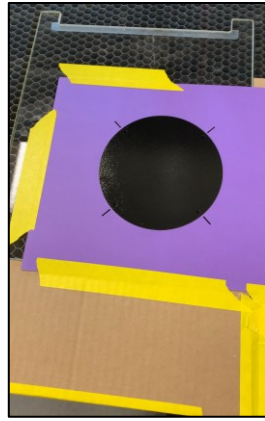
(b) Painted anode PCB in paper frame backed with borosilicate.

(c) 0.25 mm wide line etched into anode PCB paint mask.

*Figure C.5: Laser etching the anode PCB paint mask.*

The now exposed copper line was etched away using ferric chloride, however the etching process took unusually long, in excess of 6 hours. It was later found that running a scalpel along the exposed copper line sped up the process significantly, and likely indicates that more etching passes were required to fully remove the paint mask. Due to the long etching time, the line dividing the anode PCB has a varying width from 0.25 mm to approximately 0.5 mm, and the edges of the PCB have visible degradation (Figure C.6).
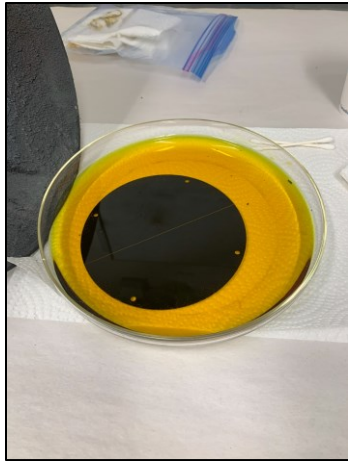
(a) Masked anode PCB in ferric chloride.

(b) Etched and cleaned anode PCB.
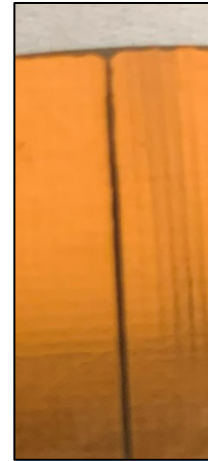
(c) Close-up of segment line and PCB edge.

Figure C.6: Anode PCB chemical etching.

After the chemical etching process, the PCB was loaded back into the CO2 laser and aligned face-down in the paper frame. Two 2.0 mm blind vias were then laser drilled into the back of the PCB, where minor deformation of the copper face occurred due to one additional etching pass. As a final step in the anode production, two 0.5 mm thick copper washers were machined and adhered in alignment with the blind vias using high-temperature epoxy (Figure C.7). These were added to give additional strength to the solder connections for the cables.
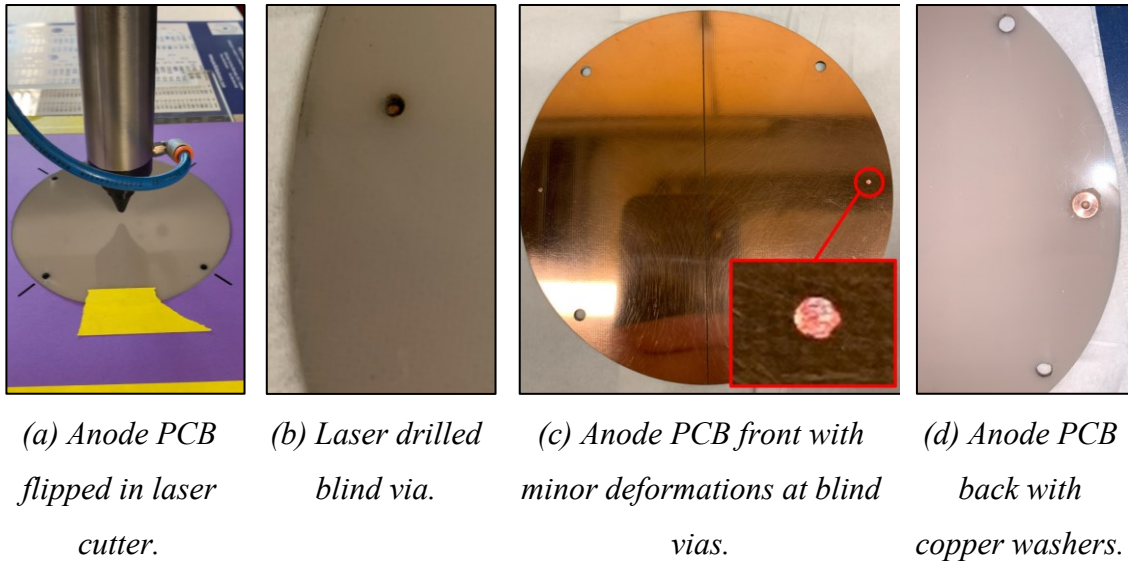
(a) Anode PCB flipped in laser cutter.   *(b) Laser drilled blind via.*   *(c) Anode PCB front with minor deformations at blind vias.*   *(d) Anode PCB back with copper washers.*

Figure C.7: Laser drilling of anode PCB.

RG-174 coaxial cable was used to make the electrical connections to the anode segments. A cross-sectional diagram of the connection is shown in Figure C.8, and images of the soldering process and attached cables are shown in Figure C.9.
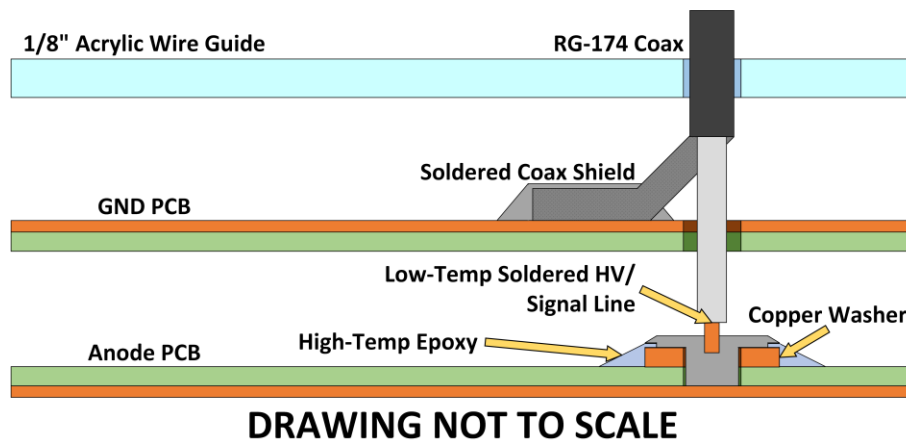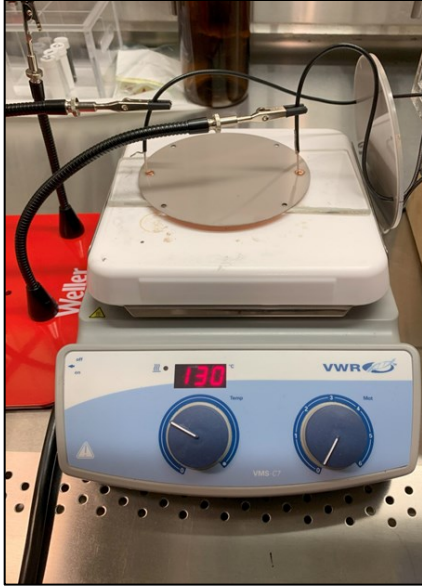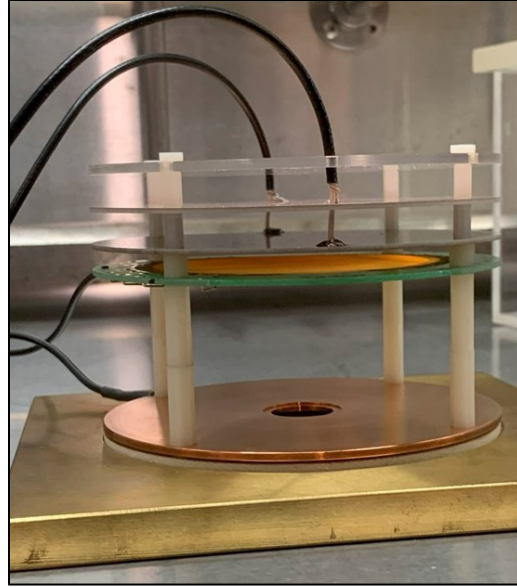

Figure C.8: Diagram of coaxial cable connection to the anode.

(a) Low-temperature soldering of the anode PCB on a hot plate.

(b) Assembled SCI-CASTER prototype 1.9 detector with soldered cables in place.

Figure C.9: Final assembly of anode PCB and detector.